LAWRENCE
LIVERMORE
NATIONAL
LABORATORY

Characterization of the Electronic Structure of Silicon Nanoparticles Using X-ray Absorption and Emission

A. S. M. Vaverka

July 18, 2008

Disclaimer

This document was prepared as an account of work sponsored by an agency of the United States government. Neither the United States government nor Lawrence Livermore National Security, LLC, nor any of their employees makes any warranty, expressed or implied, or assumes any legal liability or responsibility for the accuracy, completeness, or usefulness of any information, apparatus, product, or process disclosed, or represents that its use would not infringe privately owned rights. Reference herein to any specific commercial product, process, or service by trade name, trademark, manufacturer, or otherwise does not necessarily constitute or imply its endorsement, recommendation, or favoring by the United States government or Lawrence Livermore National Security, LLC. The views and opinions of authors expressed herein do not necessarily state or reflect those of the United States government or Lawrence Livermore National Security, LLC, and shall not be used for advertising or product endorsement purposes.

Characterization of the Electronic Structure of Silicon Nanoparticles Using X-Ray Absorption and Emission

By

APRIL SUSAN MONTOYA VAVERKA
B.S. (University of Nebraska, Kearney) 2002

DISSERTATION

Submitted in partial satisfaction of the requirements for the degree of

DOCTOR OF PHILOSOPHY

in

Materials Science & Engineering

in the

OFFICE OF GRADUATE STUDIES

of the

UNIVERSITY OF CALIFORNIA

DAVIS

Approved:

_____

_____

_____

Committee in Charge

2008

Acknowledgements

This thesis work is the result of years of hard work on my part but even more work on the part of many people who I definitely need to thank and will probably be indebted to forever. I am sure I will probably forget a few people but just know that I do appreciate all the help I got along the way from everyone.

First, there are my advisors, Tony and Subhash, so different yet each of you helped me to get through it in your own way. Tony, there is so much I need to thank you for I am not sure it will fit here but hopefully you know how grateful I am to you. Thank you for allowing me into your group and treating me like an equal even when most of the time I was not. Thank you for all the patience you had with me and my bad ideas and all the late, late, late phone conversations while I was at the beamline. Subhash, thank you for getting me through even though I knew nothing about materials science when I entered grad school and for all the wonderful opportunities that you made happen. Thank you for all times I went to your office in complete despair and left feeling like a nobel laureate.

Thanks so much to the Livermore group, Trevor, Jon and Rob. Thanks for all the help along the way not treating me like the lowly grad student… all the time. I have to give an extra thanks to Rob, who was like another advisor for me.

Next, to all my BFD accomplices, you guys made Fridays even better. To the Livermore dance party office mates, thank you for making my last years bearable.

Thank you to all the people who were there for me along the way helping me with classes, research and general mental health, Ed, Ashley, Anu, Zambranos and many others, you were all there for me in different yet important ways.

I definitely need to thank my family because even though they have no idea what I do, they still pretend like it is interesting to them. Mom and Dad, I know you probably did not want to answer the phone sometimes but thank you for doing it anyway and Casey, thanks for tolerating such a nerdy sister.

Gracias a mis suegros, su hijo es maravilloso a causa de ustedes y muchisimas gracias para darlo a mí sin dudan. Te quiero mucho.

Andres, there really are no words to express my gratitude to you. You kept me in grad school even though I was on a daily quitting spree my first and last years. You made me laugh when nothing else could and when I cried you hugged me until I stopped. You have been with me through everything and I hope we can spend the rest of our lives together forgetting all of it. I love you with all my heart.

Abstract

Resolving open questions regarding transport in nanostructures can have a huge impact on a broad range of future technologies such as light harvesting for energy. Silicon has potential to be used in many of these applications. Understanding how the band edges of nanostructures move as a function of size, surface termination and assembly is of fundamental importance in understanding the transport properties of these materials. In this thesis work I have investigated the change in the electronic structure of silicon nanoparticle assemblies as the surface termination is changed. Nanoparticles are synthesized using a thermal evaporation technique and sizes are determined using atomic force microscopy (AFM). By passivating the particles with molecules containing alcohol groups we are able to modify the size dependent band edge shifts. Both the valence and conduction bands are measured using synchrotron based x-ray absorption spectroscopy (XAS) and soft x-ray fluorescence (SXF) techniques. Particles synthesized via recrystallization of amorphous silicon/SiO_2 multilayers of thicknesses below 10 nm are also investigated using the synchrotron techniques. These samples also show quantum confinement effects but the electronic structure is different from those synthesized via evaporation methods. The total bandgap is determined for all samples measured. The origins of these differences in the electronic structures are discussed.

Table of Contents

List of Figures

Chapter 6

Chapter 7

Appendix A

Chapter 1:

Introduction

Silicon is an important material for many areas of technology including microchips and solar energy conversion and storage[1,2]. Integrated circuits (ICs) are made from circuits of transistors which are composed of predominantly silicon and solar cells are also fabricated from poly-crystalline silicon. Although silicon has already made its mark in technological history, Moore's law predicts that transistors will eventually no longer be able to shrink in size to accommodate the need for increasing memory capacity and speed[3]. In response to this, the researchers have pursued and alternative avenue for information transferal; optoelectric technology. In this technology, light, which can travel faster than electrons, will be used to transfer information in computing systems. There is, however, a problem with integrating silicon into these new technologies: silicon has an indirect bandgap which makes it a poor light emitter[4,5].

There has been considerable effort to obtain light emission from silicon structures. The fabrication of silicon/germanium structures resulted in a small increase in the emission efficiency but not to the point necessary for applications using light emission[6,7]. It has also been observed that the optical properties of semiconductors change at very small sizes and, as a consequence, we are interested in studying the novel optical properties of silicon that appear at the nanoscale. Some direct bandgap semiconductors have well understood size dependent optical properties that are attributed to quantum confinement[8,9]. An explanation of quantum confinement will be given in the next chapter. These properties are potentially suitable for use in a wide range of applications such as biological sensors[10,11] and light emitting diodes (LEDs)[12].

In silicon, the mechanisms for light emission have not been unambiguously determined and many possible origins have been identified. Along with the effects of quantum confinement, defect states, surface states and strain have all been identified as possible sources of emission from silicon nanostructures[13-17].

Due to the difficulties associated with generating silicon nanostructures, a variety of methods have been developed for their synthesis and reported in the literature. Significantly, further characterization of these materials has demonstrated that they exhibit distinct, and often conflicting, optical properties with respect to one another (eg. differences in the bandgap of the silicon nanostructures), which can be directly attributed to variations in the methods of synthesis[18]. Therefore, the variation in the modes of synthesis (and, by extension, sample uniformity) used within the scientific community makes it difficult to resolve the mechanisms of luminescence from silicon nanomaterials. This problem is compounded by the fact that the Si NCs are not always quantitatively evaluated beyond their size and interesting physical properties (e.g. novel light emission). A synopsis of the PL peak energy produced from many of these syntheses was compiled by Wilcoxon et. al.[19] and is illustrated by the graph in figure 1.1. The discrepancies in the data are attributed to the lack of consistent synthesis conditions and surface termination. Although theoretical calculations are usually helpful in resolving such discrepancies, the theoretical treatments have also provided inconsistent results.

The variation in emission properties of the Si nanostructures could be due, in part, to the different surface states produced by each synthetic method. Surface states are known to play a major role in many emission processes but little is known about the effects of surface passivation on the quantum confinement effects in silicon nanoparticles. A thorough investigation of surface termination and proximity will reveal the mechanisms of light emission and transport properties.
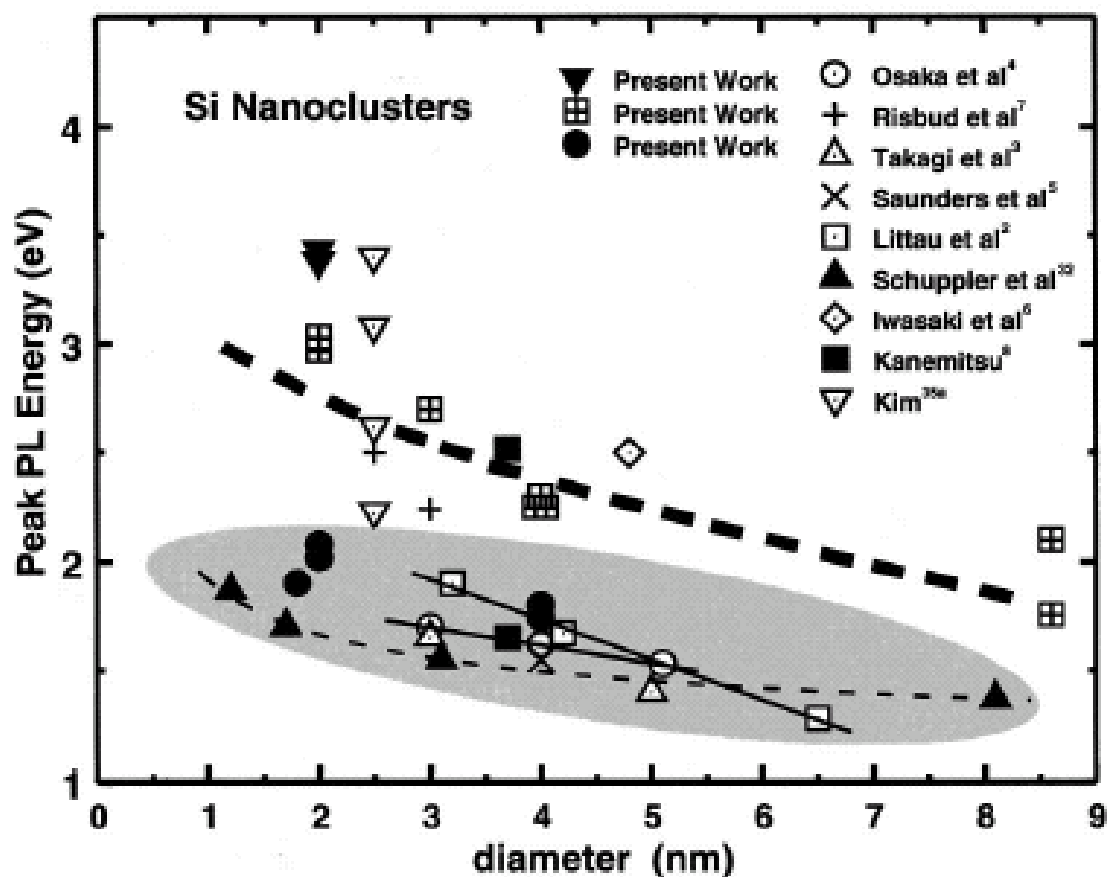
Fig. 1.1: Photoluminescence peak energies compiled for various silicon nanoparticle syntheses and theoretical calculations. The different syntheses produced many different results. Reproduced from Wilcoxon et. al.[19] Copyright (1999) by the American Physical Society.

Despite a large research effort in the area of silicon nanoparticles, there are still several questions that need to be answered before these structures can fully utilized in technological applications such as the role of surface states and proximity on the photoluminescence, and the correlation of sample synthesis to changes in the electronic.

In this thesis, the electronic properties of silicon nanoparticles are investigated using x-ray absorption spectroscopy (XAS) and soft x-ray fluorescence spectroscopy (SXF). The benefits of using these techniques allow us to obtain quantitative, element-specific information regarding the atomic and electronic structure for an extended range of Si-based nanocrystalline materials. Specifically, XAS and SXF have been used in mapping the evolution in electronic band structure in order to clarify the mechanisms of quantum confinement like behavior in Si NCs.

The electronic structure of silicon nanoparticles as a function of surface is examined in a well controlled environment. Two different syntheses have been investigated to compare the effects of synthesis on electronic properties. The focus of this thesis work is to characterize the electronic structure of thermally evaporated silicon nanoparticles and how the surface passivation affects these electronic properties. The use of gas phase synthesis creates clean nanoparticle surfaces and the nature of the experiments performed immediately alerts us to sample contamination or variation. Samples that are passivated by oxide are also measured. Both types of sample exhibit changes in the electronic structure due to quantum confinement but the magnitudes of these effects vary with surface passivation. The electronic structures of each of these sample types are discussed, as are possible reasons for differences between the two.

References

[1] M.C. Beard, Knutsen, K.P., Yu, P., Luther, J.M., Song, Q., Metzger, W.K., Ellingson, R.J., Nozik, A.J., "Multiple exciton generation in colloidal silicon nanocrystals," nanoletters **7** (8), 2506 (2007).

[2] M. Stupca, Alsalhi, M., Al Saud, T., Almuhanna, A., Nayfeh, M. H., "Enhancement of polycrystalline silicon solar cells using ultrathin films of silicon nanoparticle," Applied physics letters **91** (6), 063107 (2007).

[3] J. McCann, University of California, Davis, 2002.

[4] L.T. Canham, "Silicon quantum wire array fabrication by electrochemical and chemical dissolution of wafers," Applied physics letters **57** (10), 1046 (1990).

[5] Cohen Chelikowsky J., M., "Nonlocal pseudopotential calculations for the electronic structure of eleven diamond and zinc-blende semiconductors," Physical Review B **14** (2), 556 (1976).

[6] Q. Mi, X. Xiao, J.C. Sturm et al., "Room temperature 1.3 mm electroluminescence from strained $Si_{1-x}Ge_x/Si$ quantum wells," Applied physics letters **60** (25), 3177 (1992).

[7] M.H. Liao, T.-H. Cheng, C.W. Liu et al., "2.0 mm electroluminescence from $Si/Si_{0.2}Ge_{0.8}$ type II heterojunctions," Journal of applied physics **103**, 013105 (2008).

[8] A.P. Alivisatos, "Semiconductor clusters, nanocrystals and quantum dots," Science **271** (5251), 933-937 (1996).

[9] A.I. Ekimov and A.A. Onushcenko, "Quantum size effect in 3-dimensional microscopic semiconductor crystals," JETP Letters **34** (345) (1981).

[10] L. Wang, Zhao, W., O'Donoghue, M., Tan, W., "Fluorescent Nanoparticles for Multiplexed Bacteria Monitoring," Bioconjugate Chemistry **18** (2), 297-301 (2007).

[11] N. Elfstrom, Karlstrom, A., Linnros, J., "Silicon nanoribbons for electrical detection of biomolecules," nanoletters **8** (3), 945-949 (2008).

[12] C. Striemer, Krishnan, R., Fauchet, P., "The Development of Naocrystalline Silicon for Emerging Microelectronic and Nanoelectric Applications," JOM **56** (10), 20-25 (2004).

[13] W.-Q. Huang, F. Jin, H.-X. Wang et al., "Stimulated emission from trap electronic states in oxide of nanocrystal Si," Applied physics letters **92**, 221910 (2008).

[14] D.M. Lyons, K.M. Ryan, M.A. Morris et al., "Tailoring the optical properties of silicon nanowire arrays through strain," Nano letters **2** (8), 811-816 (2002).

[15] G. Guillois Ledoux, O., Porterat, D., Reynaud, C., Huisken, F., Kohn, B., Paillard, V., "Photoluminescence properties of silicon nanocrystals as a function of their size," Physical Review B **62** (23), 15942 (2000).

[16] G. Santana, Monroy, B.M., Ortiz, A., Huerta, L., Alonso, J.C., Fandino, J., Aguilar-Hernandez, J., Hoyos, E., Cruz-Gandarilla, F., Contreras-Puentes, G., "Influence of the surrounding host in obtaining tunable and strong visible photoluminescence from silicon nanoparticles," Applied physics letters **88**, 041916 (2006).

[17] S. Ossicini, Pavesi, L., Priolo, F., *Light Emitting Silicon for Microphotonics*. (Springer Berlin Heidelberg, 2003).

[18] E. Draeger, Grossman, J., Williamson, A., Galli, G., "Influence of synthesis conditions on the structural and optical properties of passivated silicon nansoclusters," Physical review letters **90**, 167402 (2003).

[19] J.P. Wilcoxon, G.A. Samara, and P.N Provencio, "Optical and electronic properties of Si nanoclusters synthesized in inverse micelles," Physical Review B **60** (4), 2704 (1999).

Chapter 2:

Background and Theory

This chapter provides some theoretical and empirical background for this thesis. A brief explanation of quantum confined structures is covered and is accompanied by a discussion of relevant literature within the field.

2.1 Quantum Confinement

The focus of this thesis is a characterization of specific size dependent properties of silicon nanocrystals that have considerable technological relevance. Not least among these properties are the size-dependent optical and electronic properties that could be tailored for use in a number of applications, such as memory devices and more efficient solar cells, once they are more fully understood. Since many of the size-dependent changes in nanomaterials properties are attributed to quantum confinement, a brief explanation is required to fully understand both the purpose of this research and the characterization that is performed within it.

In a semiconductor material, the electrons of highest energy of filled electronic states are referred to as the valence band and the lowest energy unfilled states are referred to as the conduction band. These are continuous bands that are separated by an energy gap. In an atomic energy diagram of the same material, the energy bands are condensed into discrete levels where the electrons are allowed. Figure 2.1 shows the atomic and bulk energy schemes. Quantum confinement occurs as the size of the
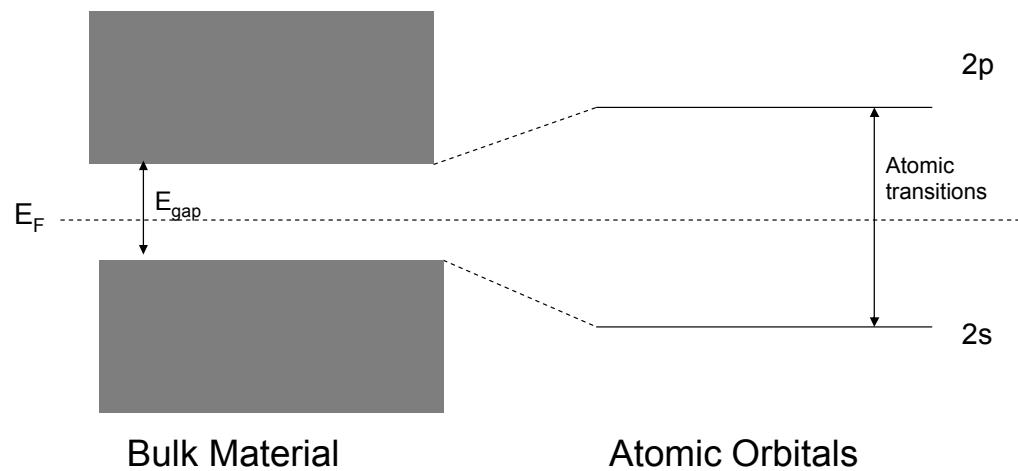
Fig. 2.1: The electronic structure of a bulk semiconductor is that of continuous bands called the valence and conduction bands. The distance between these bands is called the bandgap. The energy levels of an atom are discrete energy levels and the electrons are limited to only set energy levels called atomic orbitals.

particles approaches the Bohr radius for a core exciton in the material and the energy bands become more discrete. Some of the energy levels near the edges of the bands are no longer allowed, thereby causing the edges of the conduction and valence bands to shift.

A simple model to demonstrate the size dependence of the energy levels in a nanoparticle is the particle in an infinite square well potential. In this model, an electron is confined to a square well of length L with infinite barriers at the edges of this well. The time-independent Schrödinger equation for this one electron approximation in an infinite square well is:

$$-\frac{h^2}{2m}\Delta\psi(r) + V(r)\psi(r) = E'\psi(r) \qquad\qquad 2.1$$

where the potential V(r) is:

$$V(x) = \begin{cases} V_0 = const \\ \infty \quad otherwise \end{cases} \qquad \textit{for } 0 \le x \le L \qquad\qquad 2.2$$

Because of the infinite barrier at the boundaries of the well, the electron is confined to the well, just as it would be in a nanoparticle[1]. The solution to the Schrödinger equation gives the possible energy states of the electron:

$$E = \frac{\eta\pi}{2mL} \qquad\qquad 2.3$$

where m is the effective mass of the particle. Two important pieces of information can be obtained from equation 2.3 regarding the energy states in a confined system. First, the energy levels are discrete, as was discussed earlier in the chapter. Second, the energy is inversely dependent on the length, L, of the well. While this example is not completely applicable to nanoparticles since multiple electrons will be involved, the general concepts can be applied to quantum confinement in nanoparticles and one can generally

understand the inverse relationship between the size of a nanostructure and the energy gap.

The size and shape of the nanostructure both have an effect upon the degree of confinement that occurs. When a structure is only confined in one direction there is the case of the quantum well. If the structure is confined in two directions, a quantum wire is produced and a quantum dot or nanoparticle is confined in all three directions. The effects of increasing the dimension of confinement on the allowed energy states are shown in figure 2.2. As the number of confined directions increases, the energy levels become more discrete.

Quantum confinement brings about dramatic changes in the electronic and optical properties of a material. An example of these changes can be seen in the size dependent optical luminescence of direct bandgap semiconductors. A semiconductor whose valence band maximum and conduction band minimum are aligned are directly over on another in the band diagram are said to have a direct bandgap. Because of this, a direct radiative transition from the conduction band to the valence band is possible. Examples of direct bandgap semiconductors are cadmium selenide (CdSe), cadmium telluride (CdTe) and cadmium sulfide (CdS). The optical properties of materials are often studied using photoluminescence spectroscopy (PL). In this technique, an electron is excited from the occupied states into an unoccupied state via the absorption of a photon. At this point the system is in an excited state and the release of energy is required to return to a more stable energetic state. As the electron returns to a more stable state, some of the energy is lost through vibrational or rotational movement but if the energy gap is large enough it can be lost through emitted radiation, luminescence[2]. Figure 2.3 provides a schematic of how luminescence is produced. As the size of the particles decreases, the luminescence energy increases, which one would anticipate with the widening of the bandgap.
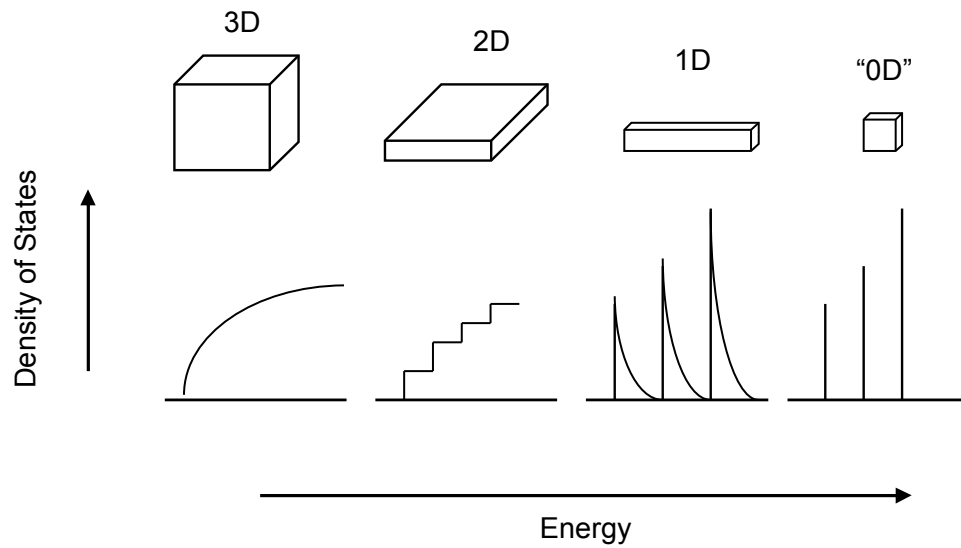
Fig. 2.2: The density of states changes as the structure is confined by increasing directions. A bulk material has continuous electronic band structure while a quantum well, confined by only direction, has regions of discontinuity. Similarly, the nanowire, confined in two directions and the quantum dot, confined in all three directions, yield more discrete energy levels.
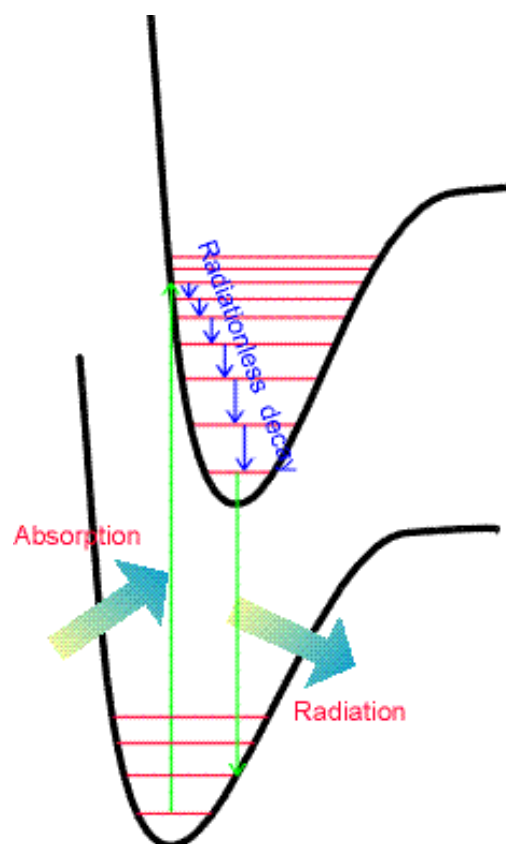
Fig. 2.3: Photoluminescence spectroscopy measures the radiative transitions occurring when an excited electron releases the energy it obtained through absorption. Absorption occurs as the electron is excited from the occupied states into unoccupied states. Reproduced from reference[2].

2.2 Previous Experimental Work

2.2.1 Size Dependent Photoluminescence in II-VI Semiconductors

Although quantum confinement has been observed in many forms, the most notable, and relevant to this work, is the size dependent emission seen from semiconductor nanoparticles[3]. Almost 30 years ago, light emission from II-VI semiconductor nanoparticles was observed to shift toward higher energy as a function of decreasing particle size[4]. As the size of the nanoparticle decreased, the energy of emission and absorption increased, which indicated that quantum confinement is the reason for this controlled shifting of the luminescence peaks. Quantum confinement was theoretically predicted for semiconductors with direct bandgaps[4]. One class of such materials is the binary II-VI semiconductors, which are composed of two elements with two valence electrons in the first element and six in the other. Examples of the binary II-VI semiconductors include CdSe, CdS and CdTe. Quantum confinement was experimentally confirmed via synthesis of direct bandgap semiconductors with size dependent properties, which lead to extensive study of the optical and electronic properties of these II-VI materials[5,6]. Recently, II-IV nanoparticles have been used for applications such as biological sensing[7] and as drug carriers for cancer therapy[7,8]. There has also been research related to changing the nanoparticle shape and size to increase the application possibilities. To date, researchers have fabricated many nanostructures including hollow nanoparticles[9,10], tetrapods[11] and multipods[12] with these different structures it is predicted that better control of the optical and electrical properties may be realized[11].

II-IV quantum dots have shown bright size-dependent luminescence. These II-VI QDs have become commercially available due to the large amount of research put into these materials. In fact, several companies offer QDs and give dramatic examples of the

luminescence on their websites. A high demand for these materials in commercial applications has spurned research efforts in these fields.

Quantum confinement is generally accepted as responsible for the size-dependent bandgaps that yield luminescence in the visible region of direct bandgap nanoparticles[3]. However, interfaces, defects and surface effects are also sources of nanoparticle luminescence and in indirect gap materials these sources take on a larger role[13]. It has been theoretically shown that dangling bonds at the surface of Si can create intermediate states in the bandgap that allow non radiant modes of energy release or different emission energies[14]. Because of these other sources of luminescence it is important to understand where changes in the electronic structure originate through careful experiments. This thesis will explore how confinement, proximity and surface passivation affect the electronic structure of silicon nanoparticles. With this information, devices made of silicon nanoparticles can be efficiently and effectively integrated into current technologies.

2.2.2 Previous Experimental Work in Silicon

Here is a brief synopsis the methods of producing silicon nanoparticles and the relevant research on nanoparticles that have, in a short time, become an important part of materials research today. Additional detail on this and related topics can be found in the literature[3,15].

2.2.2.1 Sample Synthesis

Silicon nanoparticles have been synthesized using many different techniques including solution chemistry, ion implantation, annealing of amorphous multilayers, growth in glass and gas phase techniques. Although chemical syntheses have been successfully and extensively produce II-VI semiconductor nanoparticles [3,6,16], high quality

silicon nanocrystals have proven more difficult to synthesize using chemical methods[17]. Frequently, silicon nanostructures prepared by chemical methods are characterized by broad size distributions, which leads to broad PL, or are oxidized to some degree and this adds complexity to determining the origin of the PL.

Porous silicon is produced by electrochemically etching silicon wafers. The wafer is placed in a 50% HF solution in ethanol and a current controlled electrical source is applied. An anodization reaction occurs and the silicon is etched to the point that 2-5 nm sized nanosized material is produced in p-type doped silicon[18]. These structures produce bright and efficient luminescence and were the first evidence of size dependent optical properties in silicon[19]. Nonetheless, this synthesis produces wide size distributions that lead to broad PL emission.

Chemical synthesis techniques are widely used and studied especially in II-VI semiconductor materials. In these techniques, nanoparticles are grown in solution and their size is determined by stopping the chemical reaction at the appropriate point. For silicon nanostructures, the particles are generally synthesized in a core shell method that results in the formation of a crystalline Si core coated with a shell of passivants. The organic shell stabilize the surface atoms of the nanoparticle without interfering with the optical properties[20]. However, for silicon nanoparticles, the lack of surface dipoles has hindered the surfactant binding making the process difficult to control[21].

Both ion implantation and annealing of amorphous multilayers provide the advantage of producing nanoparticles that are passivated during the course of the syntheses. During ion implantation, silicon is implanted into a silica matrix and nanoparticles are grown via Oswald Ripening. Multilayer nanostructures are then produced via the recrystallization of amorphous silicon/ silica multilayers. Multilayer samples are made by alternately depositing amorphous Si and amorphous SiO_2 films on Si wafers through radio frequency (RF) magnetron sputtering. RF magnetron sputtering

is a physical vapor deposition technique that involves the bombardment of a target with ions to induce the ejection of atoms and molecules, which are then collected on an appropriate substrate. The a-Si layers are crystallized by a rapid thermal anneal (RTA) followed by a longer furnace anneal. The RTA serves to induce nucleation of the nanocrystals and the long furnace anneal allows growth to the desired size as well as decreasing any defects in the layers[22-24]. The size of the nanoparticles is restricted by the amorphous silicon layer thickness. These samples are also passivated with amorphous oxide layers between the particles and have brilliant luminescence. Inherent silica passivation of the Si nanoparticles provides them with great stability but renders surface modification essentially impossible. Despite this limitation, interesting structures result from this synthesis and one can readily obtain electronic and optical information about the embedded silicon nanoparticles[25]. Chapter 5 gives electronic structure results from structures synthesized using this method.

Silicon NP formation within glasses is another synthesis that intrinsically passivates the particles. This method was highly researched with II-VI materials in the early 1990's [26] and also to some extent in silicon by Liu et al. [27]. In this synthesis, semiconductor powder is dissolved into a glass melt and allowed to mix homogeneously. The glass pieces are then annealed and the nanoparticles form through nucleation and growth, by Oswald ripening. The silica passivation of the nanoparticles leads to intense luminescence. However, the poor size distribution and low concentrations of semiconductor have made nanoparticle glass synthesis undesirable for many applications. Once again, this technique creates particles which cannot be studied without the presence of the host material.

Gas techniques have been found to be most suitable for our goals of studying the interactions between nanoparticles and the effects of surface environment on the electronic structure. In addition, gas techniques are important because they generate

nanoparticles with narrow size distributions and they are performed in an in-situ vacuum chamber allowing for study of the nanoparticle surface without exposure to air. It is important to note that gas phase techniques also enable relatively large amounts of nanoparticles to be synthesized in a short time[28].

There are several different gas phase synthesis techniques that include magnetron sputtering and plasma gas flow. In the magnetron sputtering technique, an electron or ion beam, in flowing argon, is directed toward a target made of the desired nanoparticle material. The force from the electron beam creates a "plume" of nanoparticles which then condenses on a substrate[29]. The plasma synthesis creates nanoparticles by flowing helium and silane gas mixture through a quartz tube at a pressure from 1-15 Torr. A current is applied to two copper electrode rings by radio frequency and a plasma is created. The particles are then directed to an annealing chamber and collected using a Faraday cup[30].

The synthesis that has been used in the research presented here is an inert gas evaporation technique. This synthesis successfully produces clean and small particles with relatively narrow size distributions. The bulk material, Si, is resistively heated in a buffer gas atmosphere. Ballistic collisions between the evaporated silicon atoms and the buffer gas cool the Si vapor causing condensation of the silicon into nanoparticles. Because the synthesis is performed under 250 mTorr of helium and the sample is held under ultra high vacuum (UHV) conditions at all other times, contamination is controlled and minimized. Metal particles have been synthesized by this method since as early as 1940 by Beeck et. al.[31] Group IV semiconductors have been synthesized in this way since the 1970's by Saito [32] who studied empirically the details of the technique. Saito characterized the size of the particles with respect to the proximity of the substrate to the evaporation source and also noticed a change in the evaporation plume with variation in the gas pressure. More recently, this synthesis has been used by van Buuren and

Bostedt et. al. in the synthesis of silicon and germanium nanoparticles with good control of the size and electronic structure[33-36]. The details of this synthesis will be discussed further in the following chapter.

2.2.2.2 Luminescence in Silicon Nanostructures

The indirect bandgap of most group IV materials leads to difficulty extracting luminescence from these structures. Luminescence in indirect gap materials requires a phonon for an electronic transition since direct radiative transitions are prohibited. Thus, efficient luminescence in indirect gap materials is not usually observed. Luminescence was observed, however, in porous silicon in 1990 by Canham [19] and this started a large amount of research in the field of silicon nanostructures. The main goal of the research was to determine the source and mechanism of light emission from these structures in order to enhance luminescence efficiencies. Significantly, the underlying mechanisms remain undetermined.

After the first reported emission from porous silicon, much of the subsequent research was directed toward enhancing the PL. Although porous silicon has been researched extensively, the synthesis generally used, etching a silicon wafer using HF and applying an electrical current, does not produce uniform structure size. This leads to broadening of the PL because each particle size emits at a slightly different wavelength. Also, smaller particle sizes are more affected by surface defects that are known to change the wavelength of the emitted light. In order to better control the size distribution and surface effects, silicon nanoparticles have become a focus of silicon research in recent years.

Many scientists believe that the effects of quantum confinement are responsible for the luminescence in silicon nanostructures. Evidence for this argument can be seen in the size dependent shifting of the luminescence peaks reported by many research

groups[20,37,38]. This size-dependent shift is obvious in a representative spectrum taken from a publication by Ledoux et. al.[38], which is reproduced in figure 2.4. The figure shows size distributions in the top graph and the corresponding PL spectra in the bottom graph. The PL peaks shift to lower wavelength (higher energy) with decreasing size of the nanoparticles. Ledoux et. al. give evidence for the quantum confinement model of silicon PL, citing shrinking core sizes for the changes of the PL with aging. This explanation of shifting PL has been cited by other research groups [39] that have used TEM and XAS to demonstrate that the Si core shrinks as the nanoparticles are further oxidized in the air leading to an increase in the bandgap and therefore a blueshift of the PL.

As with II-VI materials, the intensity of the luminescence correlates to the number of dangling bonds on the surface of the nanoparticles, which is in turn related to the level of passivation[40,41]. Silicon nanoparticles are generally passivated with hydrogen or oxide. Porous silicon that is freshly prepared is passivated with hydrogen but most aged porous silicon and embedded silicon particles are passivated with oxide[18]. Both of these passivated structures exhibit photoluminescence, although the luminescence peak energy is not the same for structures of equivalent size but with different passivation. It has been observed that changes in the surface passivation can increase the intensity of the luminescence. Many groups have observed both an increase in the intensity and a shift to higher energy of the luminescence peak as the samples age, presumably as a result of increased oxidation[39]. Also calculations by Brus et. al. have indicated that a shell of SiO_2 on a silicon core quantum dot increases the fluorescence efficiency[42]. In contrast, other research suggests that Si-O interface states cause the increase in fluorescence efficiency rather than quantum confinement[43,44]. While the enhancement in luminescence is not believed to arise from the oxide layer in isolation, the mechanism for this emission remains poorly understood.
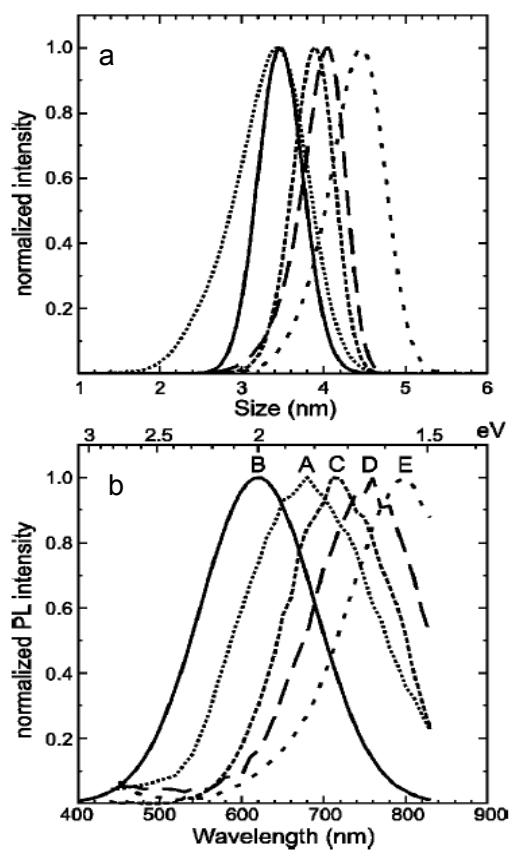
Fig. 2.4: a) Size distribution of nanoparticles. b) The photoluminescence of respective samples. It can be seen that with decreasing size of particles the luminescence peak decreases in wavelength (increases in energy). Reproduced from Ledoux et. al.[38].

It may be confusing to those familiar with research in group II-VI nanoparticles that the surface chemistry of silicon QDs is not understood, while highly luminescent, water soluble and superstructures of II-IV QDs are routinely synthesized. For group IV QDs, where advances in research are not at the same level, this is not the case. While the synthetic protocol for II-VI quantum dots is well developed, there is no such wet chemical protocol for group IV quantum dots. In fact, the luminescence wavelength for one size of silicon quantum dots can vary from red to blue by changing the surface termination from hydrogen to oxide[43,45,46]. Alternative terminations have also been reported to change the luminescence. Figure 2.5, taken from Santana et. al., shows matrix effects on the luminescence of silicon nanoparticles[47]. Silicon nanoparticles were embedded in three different silicon based dielectrics: Si_xN_y:H,Cl, $Si_xN_yO_z$:H,Cl, and Si_xO_z:H,Cl. Three different PL peak energies were obtained from each sample indicating that passivation groups do play a role in the PL of the nanoparticles. Effects of this kind are not observed in II-IV quantum dots where the mechanism for light emission is not controversial. The PL in II-VI dots can be enhanced or quenched via surface modification with little to no change in the PL energy. In the case of silicon, it is not known to which extent quantum confinement and defects (interface or surface states) control the observed PL.

2.2.2.3 Oxide Passivation Multilayer Samples for Enhancement of Luminescence

Silicon has been used for many years in technological applications such as solar cells[48], light emitting devices and as a major component of transistors for microchips[22]. For many applications it is beneficial for silicon nanoparticles to be embedded in a silica matrix for stability or integration of other device components[25].
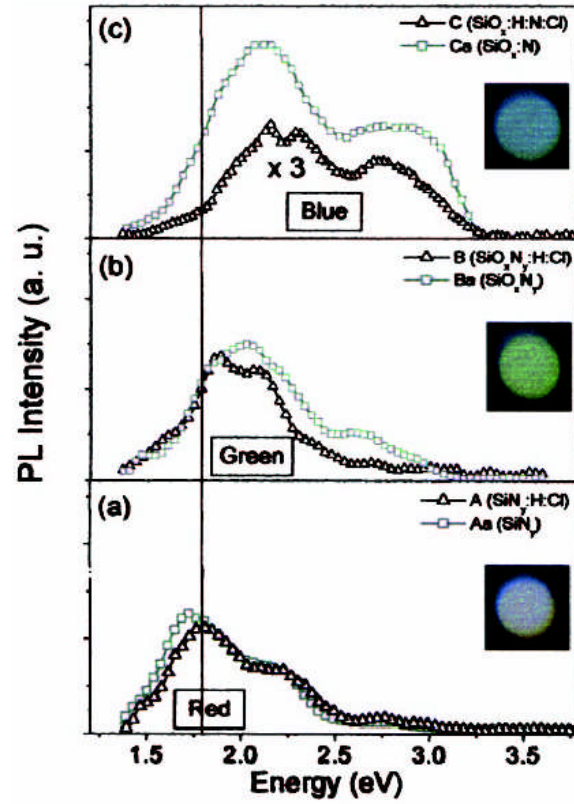
Fig. 2.5: Photoluminescence spectra of silicon nanoparticles in different matrices. The photoluminescence changes as the passivating matrix is changed. The inset pictures show the visible luminescence. Reproduced from Santana et. al. [47].

Passivation is achieved with the multilayer samples as they are intrinsically oxide passivated. These structures are also robust and easily integrated into current Si processing technology[49] making them ideal for use in the next wave of optoelectric devices. In fact, the possibility of integrating these materials into single-electron memory devices, electrostatic sensors and logic structures has also been proposed by Streimer et. al.[50]. Integrating silicon nanocrystals into memory devices could decrease power consumption while storing information for long periods. Light emitting nanocrystals could also be used for optical transmission in the next wave of information technology[50].

Previously, nanoparticle silicon multilayers crystallized from amorphous silicon (a-Si) layers in a-Si/SiO_2 layers could only be fabricated with dimensions in excess of 4 nm because of the large lattice mismatch between the silicon and SiO_2[23,24]. Recently, layers smaller than 2 nm have been crystallized into nanoparticles[51,52] through a two step annealing process at higher temperatures. Many interesting optical and electronic properties are observed in this size regime. For example, crystallized samples with 2 nm layers exhibited bright luminescence around 1.4 eV (885 nm), while the luminescence was blue shifted to around 1.7 eV (730 nm) for 1 nm thick samples. Many optical experiments have been performed on a-Si/SiO_2 multilayers and also on similar nanoparticle samples formed from SiO_x/SiO_2 multilayers. In the annealing step of the other synthesis, amorphous SiO_x layers phase separate to form Si nanoparticles and SiO_2. It is interesting, therefore, that the photoluminescence spectroscopy (PL) from these two types of samples is similar even though they have very different electronic structures.

2.2.2.4 Doping of Nanoparticles to Enhance Luminescence

Research has also been performed to determine if Si based structures can produce light emission at the telecommunications wavelength (1535 nm). Bulk silicon

cannot produce emission at this wavelength due to its indirect bandgap. Nonetheless, doped and confined Si structures are potential candidates for stimulating emission at this wavelength. By confining electrons in nanostructures, the electronic wavefunctions are spread out which increases the probability of radiative energy decay due to an increase in wavefunction overlap. This would allow for other optically active atoms to be excited[53]. For emission in the telecommunications region it is also necessary to dope the nanostructures with highly optically active rare earth elements such as erbium (Er). The nanoparticle is excited by a photon and produces an electron-hole pair. This electron-hole pair non-radiatively transfers its energy to the Er center via a dipole-dipole interaction (Förster energy transfer). A non-radiative decay to the $^4I_{13/2}$ state is followed by a radiative decay to the $^4I_{15/2}$ state which is the characteristic 1535 nm emission[53].

The bright emission at 1535 nm from Er^{3+} states is due to an intra band $4f$ transition ($^4I_{13/2} \rightarrow {}^4I_{15/2}$). This corresponds to the region of low loss for silica optical fibers. Silicon based optical sources would integrate easily into current optical fiber systems and sources compatible with fiber systems are in high demand. This has lead to research in the field of Er doping of Si nanostructures[53] such as porous silicon, nanocrystalline Si and Si quantum dots[53,54]. Porous Si is often too fragile to be used in many devices[53]. The nanocrystalline Si relys on the Er in an amorphous Si layer and higher temperatures would be needed for stimulated emission[55]. Coupling the absorption bands of Si nanoparticles and the Er excited states has been observed by research groups but the synthesis of monodispersed Er-doped nanoparticles is not readily achieved. Despite these challenges, the tunability of the optical properties in these systems make them of interest in current and future research[53].

2.3 Theoretically Calculated Predictions

Experimental research has often resulted in confusing or contradictory reports in the field of silicon nanoparticles. Theoretical calculations are used to help explain the experimental evidence as well as predict the results of difficult experiments. However, it has been observed that the calculated bandgaps do not correspond with the bandgaps determined by PL techniques[56]. The discrepancies between theoretical and experimental treatments can be attributed to limitations of the theoretical models or misinterpretation of the experimental results. This will be discussed in more depth later in this section.

2.3.1 Types of Modeling Used to Predict Band Structures of Nanoparticles

Several modeling schemes have been used to predict the widening of the band gap of silicon nanoparticles as the size decreases. Some of the most commonly used methods are the effective mass approximation (EMA), the tight binding method, ab-initio calculations, and pseudopotential theory. Each of these methods is based on certain assumptions that lead to intrinsic problems or benefits which can add to or detract from the accuracy of the resultant bandgaps. Each method will be discussed briefly here and the more accurate models will be compared to experimental results later in the thesis.

2.3.1.1 Effective mass approximation (EMA)

This method was one of the first used to predict the bandgaps of semiconductor nanoparticles. This modeling scheme replaces the periodic crystal field in a material with an effective electron mass in the Hamiltonian[57]. As a consequence, the EMA is only accurate when the extremum of the energy band of interest is in the center of the Brillouin zone which is not the case of silicon[57]. It also assumes the energy bands are parabolic, which is a good assumption for direct gap but not for indirect bandgap materials. Detailed information about the original assumptions made in this method can

be found in papers by Luttinger et. al.[57,58]. Many of the calculations of the electronic bands of silicon nanostructures using this method were performed by Takagahara et al.[57-59]. While this method was important to the early work it cannot be easily generalized to Si nanoparticles and does not calculate an accurate bandgap[13].

2.3.1.2 Tight binding method

This method assumes that the electrons are localized in the material and are concentrated in the bonds between atoms. Because of these assumptions, the tight binding approach provides reasonably accurate predictions of covalently bonded, valence states but not for the unfilled conduction band states. Si nanoparticles were modeled by Hill and Whaley by adding shells of Si atoms around a central Si atom and passivating the dangling bonds at the surface with H atoms with bandgaps that are much higher than experimentally observed[60].

2.3.1.3 Pseudopotential theory

Possibly the most accurate band calculations for silicon nanoparticles use pseudopotential theory[61,62]. Pseudopotential theory treats the core electrons and valence electrons differently. An effective potential is applied to the valence electrons that is a combination of the pseudopotential for the core region and a Coulomb potential for the outer orbitals[13]. Therefore, in the pseudopotential method the wavefunction of the valence electrons is divided into two parts a smooth part outside the core region and an oscillatory part inside the core region[34]. There are two types of pseudopotential theory calculations; experimental and ab-initio. The first is based on experimental data already obtained and the second is self-consistent which is based on fundamental principles. The method which will be discussed is the empirical pseudopotential method because it

is generally the most accurate model for calculating band structures of nanoparticles[15,62-65].

In this method, the electronic structure is determined as solutions to the single particle Schrödinger's equation:

$$\hat{H}\psi_i = \varepsilon_i \psi_i \qquad (2.4)$$

$$\hat{H} = -\frac{1}{2}\nabla^2 + V(r) \qquad (2.5)$$

$$V(r) = \sum_{atom} \upsilon_{atom}(r - R_{atom}) \qquad (2.6)$$

where V(r) is the mean-field potential that is the sum of the atomic potentials $v_{atom}(r)$ and R_{atom} are position vectors. The wavefunctions, ψ_i, are plane waves[64]. The potentials of the reciprocal lattice vector, $\upsilon_{atom}(q)$, are fitted to a series of experimental data and also to first principle calculations in order to get the best fit to experimental results.

Another important aspect of these calculations is the structure of the particles. In calculations by Zunger et. al. [63,64] the nanoparticles are considered, as in experimental results, to have interatomic distances similar to that of bulk in the center of the nanoparticle. The only major differences between the two calculations of particles are at the surface where dangling bonds occur. In the work presented by Zunger et. al. the bonds are either passivated with hydrogen or bonded to interior atoms[62,63].

Zunger and Wang have shown that without taking into account surface effects the bandgap of nanostructures (spheres, rectangular boxes and cubic boxes) with diameter, d, can be plotted vs. effective diameter and be fit using the equation:

$$E_g(d) \approx 1.167 + 88.34/d^{1.37}(eV) \qquad 2.7$$

Where E_g is the band gap of the nanoparticle. This plot is shown in figure 2.4 and is compared to the values previously calculated using the effective mass approximation and a truncated crystal calculation. It is noted, however, that the pseudopotential

calculation does not take into account the surface effects on the bandgap of the particles.

In a more recent publication by Zunger and Reboredo the bandgap of silicon nanoparticles was recalculated taking into account coulomb effects. In this calculation, the nanoparticles were assumed to be spherical with atoms in the same position as a bulk material centered around a single Si atom. The dangling bonds on the surface atoms were passivated with hydrogen. This calculation resulted in a smaller bandgap than previously calculated [62] which provides the best fit with experimental results reported to date. Our experimental results on electronic structure measurements of various silicon nanostructures will be compared to these theoretical results in subsequent chapters.
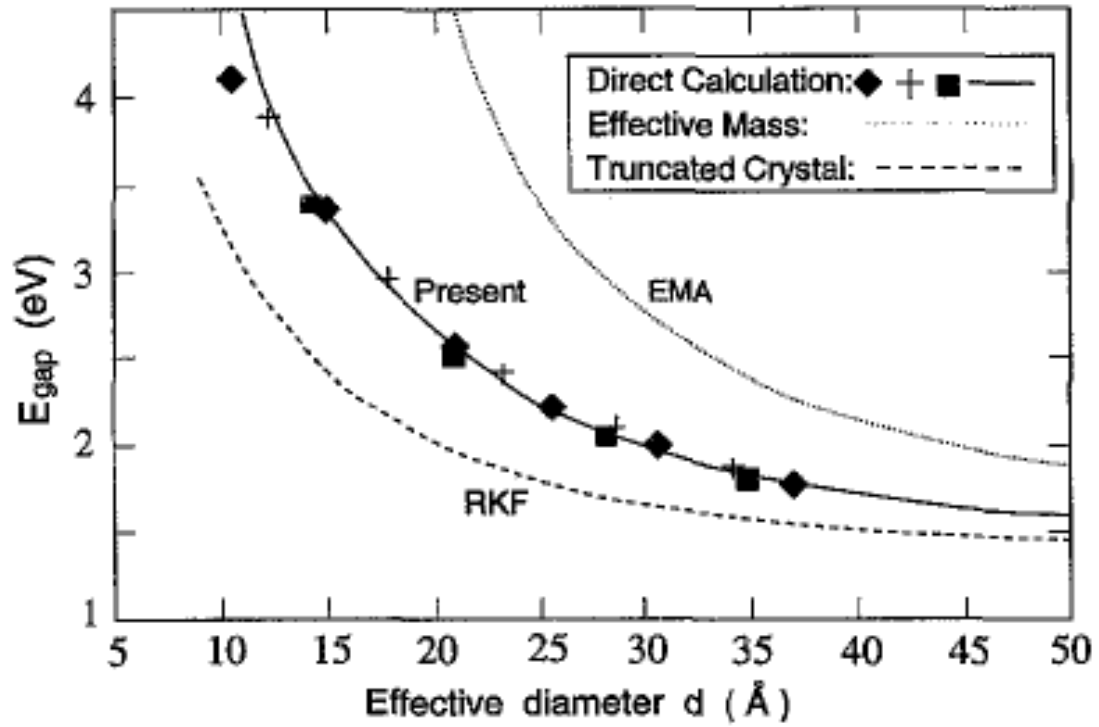
Fig. 2.6: Calculated bandgaps of silicon nanoparticles by various methods. The center line is calculated by psuedopotential method and is of interest to this research. The alternative two methods, the effective mass approximation (EMA) and truncated crystal method do not produce accurate bandgaps. Reproduced from Zunger and Wang[64].

References

[1] H. Ibach and H. Luth, *Solid-state physics: An introduction to principles of materials science*. (Springer Verlag, Berlin, 2003).

[2] P.W Atkins, *Physical chemistry*, 6 ed. (Oxford University Press, 1999).

[3] A.P. Alivisatos, "Semiconductor clusters, nanocrystals and quantum dots," Science **271** (5251), 933-937 (1996).

[4] A.I. Ekimov and A.A. Onushcenko, "Quantum size effect in 3-dimensional microscopic semiconductor crystals," JETP Letters **34** (345) (1981).

[5] C.R. Kagan, Murray, C.B., Nirmal, M., Bawendi, M.G., "Electronic energy transfer in CdSe quantum dot solids," Physical Review Letters **76** (9), 1517 (1996).

[6] C.B. Murray, D.J. Norris, and M.G. Bawendi, "Synthesis and characterization of nearly monodisperse CdE (E = S, SE, TE) semiconductor nanocrystallites," Journal of american chemical society **115** (19), 8706 (1993).

[7] L. Wang, Zhao, W., O'Donoghue, M., Tan, W., "Fluorescent Nanoparticles for Multiplexed Bacteria Monitoring," Bioconjugate Chemistry **18** (2), 297-301 (2007).

[8] J. Zhang, Lan, C., Post, M., Simard, B., Deslandes, Y., Hsieh, T., "Design of nanoparticles as drug carriers for cancer therapy," Cancer Genomics and Proteomics **3** (3-4), 147-157 (2006).

[9] Y. Yin, Erdonmez, C., Cabot, A., Hughes, S., Alivisatos, A.P., "Colloidal synthesis of hollow cobalt sulfide nanocrystals," Advanced Function Materials **16** (11), 1389 (2006).

[10] Y. Yin, Rioux, R.M., Erdonmez, C., Cabot, A., Hughes, S., Somorjai,G.A., Alivisatos, A.P., "Formation of Hollow Nanocrystals through the Nanoscale Kirkendall Effect," Science **304** (5671), 711 (2004).

[11] L. Manna, Milliron, D.J., Meisel, A., Scher, E.C., Alivisatos, A.P., "Controlled growth of tetrapod-branched inorganic nanocrystals," Nature Materials **2** (6), 382 (2003).

[12] Y.H. Leung, Djurisic, A.B., Choy, W.C.H., Xie, M.H., Gao, J., Cheah, K.W., Man, K.Y.K., Chan, W.K., "Synthesis and properties of ZnO multipod structures," Journal of Crystal Growth **274**, 430 (2005).

[13] S. Ossicini, Pavesi, L., Priolo, F., *Light Emitting Silicon for Microphotonics*. (Springer Berlin Heidelberg, 2003).

[14] M. Schluter, Cohen M.L., "Nature of conduction-band surface resonances for Si(111) surfaces with and without chemisorbed overlayers," Physical Review B **17** (2), 716 (1978).

[15] A.P. Alivisatos, "Perspectives on the Physical Chemistry of Semiconductor nanocrystals," Journal of physical chemistry **100**, 13226 (1996).

[16] A.R. Kortan, R. Hull, R.L. Opila et al., "Nucleation and growth of CdSe on ZnS quantum crystallite seeds, and vice versa, in inverse micelle media," Journal of american chemical society **112**, 1327 (1990).

[17] G. Belomoin, Therrien, J., Nayfeh, M., "Oxide and hydrogen capped ultrasmall blue luminescent Si nanoparticles," Applied physics letters **77** (6), 779 (2000).

[18] P. Bettotti, M. Cazzanelli, L. Dal Negro et al., "Silicon nanostructures for photonics," Journal of physics:Condensed matter **14**, 8253-8281 (2002).

[19] L.T. Canham, "Silicon quantum wire array fabrication by electrochemical and chemical dissolution of wafers," Applied physics letters **57** (10), 1046 (1990).

[20] J.D. Holmes, Ziegler,K.J., Doty, C., Pell, L.E., Johnston, K.P., Korgel, B.A., "Highly luminescent silicon nanocrystals with discrete optical transitions," JOURNAL OF THE AMERICAN CHEMICAL SOCIETY **123**, 3743-3748 (2001).

21   A.J. Williamson, Bostedt, C., van Buuren, T., Willey, T.M., Terminello, L., Galli, G., Pizzagalli, L., "Probing the Electronic Density of States of Germanium Nanoparticles: A Method for Determining Atomic Structure," Nanoletters **4** (6), 1041-1045 (2004).

22   R. Krishnan, University of Rochester, 2005.

23   L. Tsybeskov, Hirschman, K.D., Duttagupta, S.P., Zacharias, M., Fauchet, P.M., McCaffrey, J.P., Lockwood, D.J., "Nanocrystalline-silicon superlattice produced by controlled recrystallization," Applied physics letters **71**, 43-45 (1998).

24   Lockwood D.J. Grom G.F., McCaffrey J.P., Labbe H.J., Fauchet P.M., White B., Diener J., Kovalev D., Koch F., Tsybeskov L., "Ordering and self-organization in nanocrystalline silicon," Nature **407**, 358 (2000).

25   A. Zimina, Eisebitt, S., Eberhardt, W., "Electronic structure and chemical environment of silicon nanoclusters embedded in a silicon dioxide matrix," Applied physics letters **88**, 163103 (2006).

26   L. Liu, Risbud, S., "Quantum-dot size distribution analysis and precipitation stages in semiconductor doped glasses," Journal of applied physics **68** (1), 130028 (1990).

27   S. Risbud, Liu, L., Shackelford, J., "Synthesis and luminescence of slicon remnants formed by truncated glassmelt-particle reaction," Applied physics letters **63** (12), 1648 (1993).

28   C. Bostedt, van Buuren, T., Willey, T.M., Franco, N., Terminello, L., Heske, C., Moller, T., "Strong quantum-confinement effects in the conduction band of germanium nanocrystals," Applied physics letters **84** (20), 4056 (2004).

29   C.K. Chung, Wu, B.H., "Thermally induced formation of SiC nanoparticles from Si/C/Si multylayers deposited by ultra-high-vacuum ion beam sputtering," Nanotechology **17** (13), 3129 (2006).

30   Y. Dong, Bapat, A., Hilchie, S., Kortshagen, U., Campbell, S. A., "Generation of nano-sized free standing single crystal silicon particles," Vacuum science technology B **22** (4), 1923 (2004).

31   O. Beeck, Smith, A.E., Wheeler, A., "Catalytic activity, crystal structure and adsorptive properties of evaporated metal films," Proceedings of the royal society A **177**, 62 (1940).

32   Y. Saito, "Crystal structure and habit of silicon and germanium particles grown in argon gas," Journal of crystal growth **47**, 61-72 (1979).

33   C. Bostedt, van Buuren, T., Willey, T.M., Franco, N., Moller, T., Terminello, L., "Photoemission spectroscopy of germanium nanocrystal films," Journal of electron spectroscopy and related phenomena **126**, 117-124 (2002).

34   C. Bostedt, University of Hamburg, 2002.

35   C. Bostedt, van Buuren, T., Willey, T.M., Terminello, L., "Controlling the electronic structure of nanocrystal assemblies by variation of the particle-particle interaction," Applied physics letters **85** (22), 5334 (2004).

36   T. van Buuren, Dinh, L.N., Chase, L.L., Siekhaus, W.J., Terminello, L.J., "Changes in the electronic properties of si nanocrystals as a function of particle size," Physical Review Letters **80** (17), 3805 (1998).

37   J.S. Biteen, Lewis, N.S., Atwater, H.A., Polman, A., "Size-dependent oxygen-related electronic states in silicon nanocrystals," Applied physics letters **84** (26), 5389 (2004).

38   G. Guillois Ledoux, O., Porterat, D., Reynaud, C., Huisken, F., Kohn, B., Paillard, V., "Photoluminescence properties of silicon nanocrystals as a function of their size," Physical Review B **62** (23), 15942 (2000).

39   J.A. Carlisle, Germanenko, I.N., Pithawalla, Y.B., El-Shall, M.S., "Morphology, photoluminescence and electronic structure in oxidized silicon nanoclusters," Journal of electron spectroscopy and related phenomena **114-116**, 229-234 (2001).

40   M. Lopez, Garrido, B., Garcia, C., Pellegrino, P., Perez-Rodriguez, A., Morante, J.R., "Elucidation of the surface passivation role on the photoluminescence emission yield of silicon nanocrystals embedded in SiO_2," Applied physics letters **80** (9), 1637 (2002).

41   A.A. Seraphin, Ngiam, S.-T., Kolenbrander, K.D., "Surface control of luminescence in silicon nanoparticles," Journal of applied physics **80**, 6429 (1996).

42   Z. Zhou, Friesner, R., Brus, L., "Electronic structure of 1 to 2 nm diameter silicon core/shell nanocrystals: surface chemistry, optical spectra, charge transfer and doping," Journal of american chemical society **125**, 15599-15607 (2003).

43   M.V. Wolkin, Jorne, J., Fauchet, P.M., Allan, G., Delerue, C., "Electronic states and luminescence in porous silicon quantum dots: The role of oxygen," Physical review letters **82**, 197 (1999).

44   Y. Kanemitsu, T. Ogawa, K. Shiraishi et al., "Visible photoluminescence from oxidized Si nanometer-sized spheres: exciton confinement on a spherical shell," Physical Review B **48** (7), 4883-4886 (1993).

45   A. Puzder, Williamson, A.J., Grossman, J.C., Galli, G., "Surface chemistry of silicon nanoclusters," Physical Review Letters **88** (9), 097401 (2002).

46   A. Puzder, Williamson, A.J., Grossman, J.C., Galli, G., "Computational Studies of the optical emission of silicon nanocrystals," Journal of american chemical society **125**, 2786-2791 (2003).

47   G. Santana, Monroy, B.M., Ortiz, A., Huerta, L., Alonso, J.C., Fandino, J., Aguilar-Hernandez, J., Hoyos, E., Cruz-Gandarilla, F., Contreras-Puentes, G., "Influence of the surrounding host in obtaining tunable and strong visible photoluminescence from silicon nanoparticles," Applied physics letters **88**, 041916 (2006).

48   M. Stupca, Alsalhi, M., Al Saud, T., Almuhanna, A., Nayfeh, M. H., "Enhancement of polycrystalline silicon solar cells using ultrathin films of silicon nanoparticle," Applied physics letters **91** (6), 063107 (2007).

49   R.A. Soref, "Silicon-based Optoelectronics," Proceedings of IEEE **81**, 1687 (1993).

50   C. Striemer, Krishnan, R., Fauchet, P., "The Development of Naocrystalline Silicon for Emerging Microelectronic and Nanoelectric Applications," JOM **56** (10), 20-25 (2004).

51   M. Zacharias, Streitenberger, P., "Crystallization of amorphous superlattices in the limit of ultrathin films with oxide interfaces," Physical Review B **62** (12), 8391 (2000).

52   M. Zacharias, Blazing, J., Hirschman, K., Tsybeskov, L., Fauchet, P.M., "Extraordinary crystallization of amorphous Si/SiO_2 superlattices," Journal of non-crystalline solids **266-269**, 640-644 (2000).

53   A.J. Kenyon, "Quantum confinement in rare-earth doped semiconductor systems," Current Opinion in Solid State and Materials Science **7**, 143-149 (2003).

54   M. Fujii, Yoshida, M., Hayashi, S., Yamamoto, K., "Photoluminescence from SiO_2 films containing Si nanocrystals and Er: Effects of nanocrystalline size on the photoluminescence efficiency of Er^{3+}," Journal of applied physics **84** (8), 4525 (1998).

[55] X.W. Zhao, H. Isshiki, Y. Aoyagi et al., "Formation and device application of Er-doped nanocrytalline Si using laser ablation," Materials Science Engineering G **74**, 197 (2000).

[56] G. Allan, Delerue, C., Lannoo, M., "Nature of luminescent surface states of semiconductor nanocrystallites," Physical review letters **76** (16), 2961 (1996).

[57] J.M. Luttinger, Kohn, W., "Motion of electrons and holes in perturbed periodic fields," Physical Review **97** (4), 869 (1955).

[58] J.M. Luttinger, "Quantum theory of cyclotron resonance in semiconductors: General Theory," Physical Review **102** (4), 1030 (1956).

[59] T. Takagahara, Takeda, K., "Theory of the quantum confinement effect on excitons in quantum dots of indirect-gap materials," Physical Review B **26** (23), 15578 (1992).

[60] N.A. Hill, Whaley, K.B., "Size dependence of excitons in silicon nanocrystals," Physical review letters **75** (6), 1130 (1995).

[61] E. Draeger, Grossman, J., Williamson, A., Galli, G., "Influence of synthesis conditions on the structural and optical properties of passivated silicon nansoclusters," Physical review letters **90**, 167402 (2003).

[62] F. Reboredo, Zunger, A., "Surface-passivation-induced optical changes in Ge quantum dots," Physical Review B **63**, 235314 (2001).

[63] F. Reboredo, Franceschetti, A., Zunger, A., "Dark exitons due to direct coulomb interactions in silicon quantum dots," physical Review B **61** (19), 13073 (2000).

[64] A. Zunger, Wang, L.W., "Theory of silicon nanostructures," Applied surface science **102**, 350-359 (1996).

[65] A. Zunger, "Pseudopotential theory of semiconductor quantum dots," Phys. stat. sol **224** (3), 727-734 (2001).

Chapter 3:

Experimental Techniques

This chapter gives a brief overview of the experimental techniques used to investigate the size and electronic structure of silicon nanoparticles which include atomic force microscopy (AFM) and two synchrotron based techniques: x-ray absorption spectroscopy (XAS) and soft x-ray fluorescence (SXF). AFM is a scanned probe microscopy technique that is used to analyze the size and structure of the particles. XAS and SXF are used to probe the conduction and valence band density of states of the silicon nanoparticles. The general concepts of synchrotron radiation are also discussed within this chapter as an aid in the description of the XAS and SXF techniques.

3.1 AFM

Atomic force microscopy, which was first introduced by Binnig et. al.[1] in 1986, is a surface imaging technique that uses a cantilever with a small tip on one end (figure 1), on the order of 5 nm, to raster over the surface of a sample in order to give topographical information. A benefit to using AFM is the capability for imaging on almost any surface. Other imaging techniques such as scanning tunneling microscopy (STM) require conducting samples, while transmission electron microscopy (TEM) requires difficult sample preparation of very thin samples. AFM does not have either of these sample restrictions making this technique an effective method for size determination of nanoparticles, especially on flat substrates. In addition, AFM can be performed quickly compared to other imaging techniques because it does not have to be performed under vacuum[1].
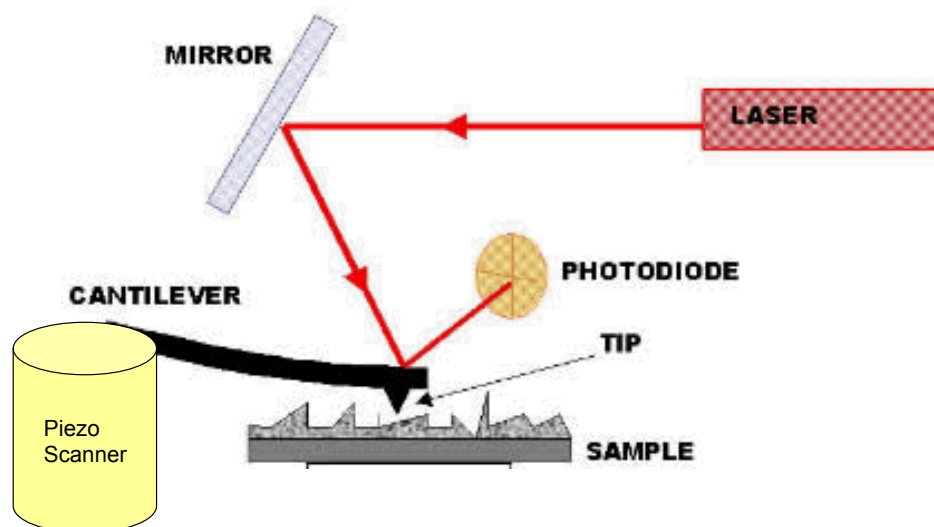
Fig. 3.1: Schematic of AFM. The laser is focused onto the end of cantilever tip and reflected onto photodiode detector. The detector sends this information to the computer that keeps the tip steady above the surface of the sample without crashing the tip into the samples surface and also produces a topography image of the sample surface.

For these measurements to be possible piezo electric crystals in the instrument called the piezo tube scanner, allow for small movements and provide the ability to bring the tip in close proximity to the sample surface. Piezo electric crystals expand or contract with electric stimulation and a small amount of applied voltage results in a small expansion of the crystal. In AFM, the tip is brought close enough to the surface for van der Waals interactions between the tip and surface to occur. The tip is brought close to the surface of the sample mechanically and is then approached using the piezo tube scanner. As the tip gets closer to the sample surface, interactions between the surface and tip pull the tip into the surface giving an indication that the tip has reached the surface of the sample[2].

Imaging is achieved by laterally rastering the tip over the surface of the sample and detecting perpendicular tip movement. The tip movement is monitored by a laser beam focused on the tip that is reflected into a quadrant photodiode detector. As the tip is deflected by the topography of the sample surface, the reflected beam moves to different regions on the detector. A feedback loop based upon the detector signal and the z-axis piezo is used to keep the tip at a constant height above the sample. A schematic of the AFM is shown in figure 3.1.

The resolution of AFM is described by two distinct components; these are the lateral and z-direction resolutions. The lateral resolution is determined by the tip radius as shown in figure 3.2. A sharper probe increases the maximum resolution that can be achieved. The z-direction or vertical resolution is much higher than the lateral direction and is limited only by external vibrations such as acoustic noise, thermal vibrations and room vibrations, which can be reduced by noise isolation. The accuracy of the height determination using AFM is on the order of ± 2 Å depending on how well the instrument is isolated from vibrations[2]. The photodiode is very sensitive to the motion of the tip

Scanning tip

Topography
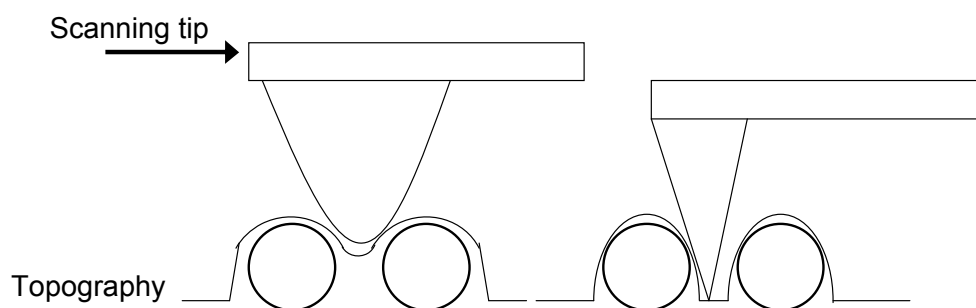
Fig. 3.2: The size of the AFM tip is the most important in the lateral resolution of the image. As the larger tip on the left is rastered over the two particles they cannot be resolved in the image because the tip cannot fit in between the two particles whereas the higher aspect ratio tip on the right can resolve the two particles because it is able to fit between the two particles.

and thus provides a feedback loop to the piezo scanner for a high resolution topography image.

AFM is performed in three different operational modes. These are the contact, non-contact and tapping modes. In contact mode the tip is always in contact with the surface and moved back and forth over the sample to obtain images. A potential drawback of the contact mode is that the tip can move the nanoparticles on the substrate. As such, contact mode was not used in this research.

Both non-contact and tapping modes oscillate the cantilever tip at a resonance frequency in order to monitor the surface topography with high sensitivity. Non-contact mode does not allow the tip to touch the surface of the sample. The tip is oscillated with a small amplitude and close enough to be affected by van der Waals interactions with the sample surface[3]. These attractive forces between the tip and the sample are measured to obtain the topographic image of the sample surface. Non-contact mode is usually used in vacuum chambers because the water and other contaminants on the surface are minimized and do not interfere with the measurement. In addition, it is ideally suited for fragile samples because there is no contact with the sample surface.

During tapping mode the tip is oscillated at larger amplitude than non-contact mode and makes slight contact with the surface of the sample. The repulsive forces on the cantilever tip are monitored and changes in the amplitude of the oscillations are recorded to obtain an amplitude image. The topography is obtained from the movement of the piezo scanner. Tapping mode was selected for use in this project because the samples are not fragile enough to require non-contact mode but do need to minimize the tip induced movement of particles on the substrate surface one might anticipate using contact mode[4].

3.1.1 AAC and MAC Mode

As mentioned previously, the cantilever tip is oscillated at its resonant frequency. Two different methods of causing the tip to oscillate have been used in this project; magnetic alternating current mode (MAC) and acoustic alternating current mode (AAC). Imaging was predominantly conducted using a PicoSPM AFM (Molecular Imaging)[2], which provides the capability of operating in both the MAC and AAC modes.

In the operation of MAC mode, the tip is coated with a magnetic material. The tip oscillates by an alternating current created by a coiled wire producing an alternating magnetic field. The amplitude of the oscillations is again monitored by the position sensitive photodiode detector. As the tip scans the sample surface, the amplitude is kept constant by changing the voltage supplied to the Z-axis piezo. The topography image is generated by this changing voltage[2].

In this project AAC mode AFM is also used since it gives a similar resolution to MAC mode and also does not disturb the particles on the substrate surface. In AAC mode the entire scanner head of the AFM oscillates under the driving force of the piezo electrics[2].

For this project, the main goal of AFM characterization is to determine particle sizes and size distributions. Figure 3.3a shows a typical blank highly oriented pyrolytic graphite (HOPG) substrate as well as nanoparticles deposited on HOPG, 3.3b. The respective *z*-height data for each image is also included. The blank HOPG image shows clear step edges that often appear in this substrate. HOPG is made up of sheets of graphite which are weakly bonded together by van der Waals force. The height of one sheet is known to be 3.5 Å[5]. Using this information, the AFM can be calibrated using the step edges because they always have a height which is a multiple of 3.5 Å. A representative AFM image of silicon nanoparticles deposited on HOPG can be seen in figure 3.4. The particles are assumed to be spherical in shape, as determined by
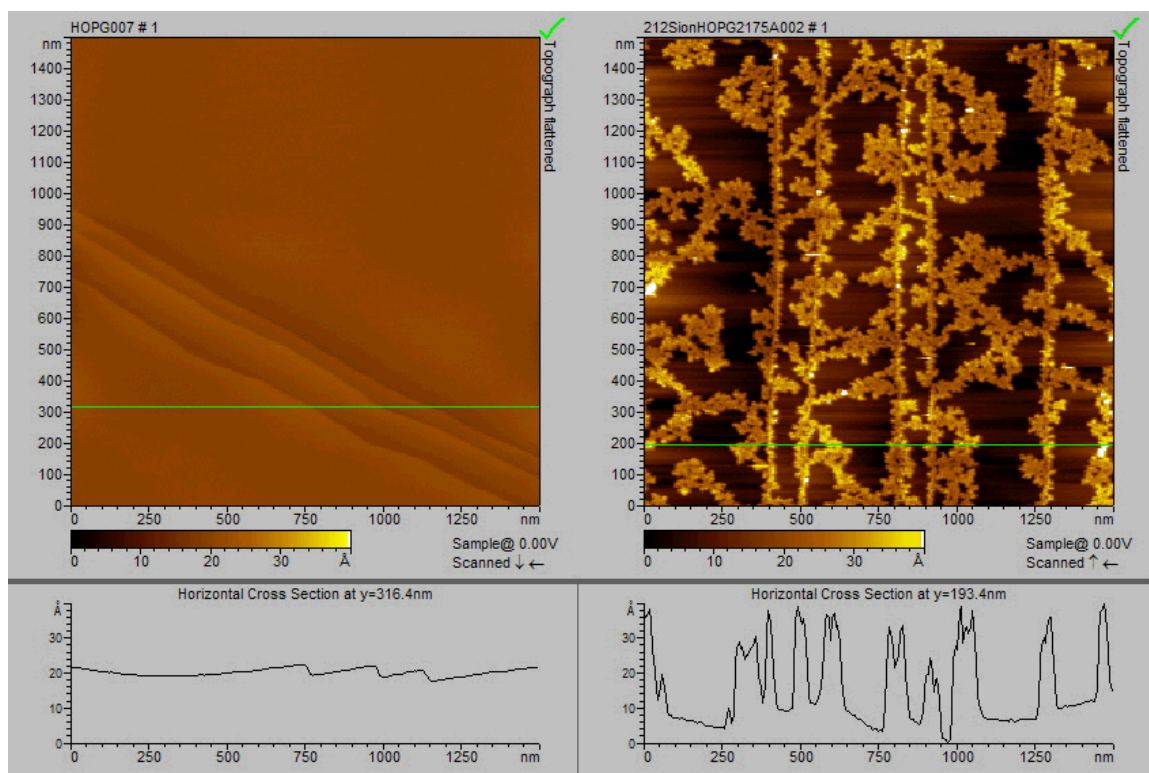
Fig. 3.3 a) Blank HOPG showing step edges that run diagonally across the image and **b)** HOPG with deposited nanoparticles that aggregate at step edges. The z-height topography shown below each of the images shows the step edges on the blank HOPG and the nanoparticles on the deposited sample.
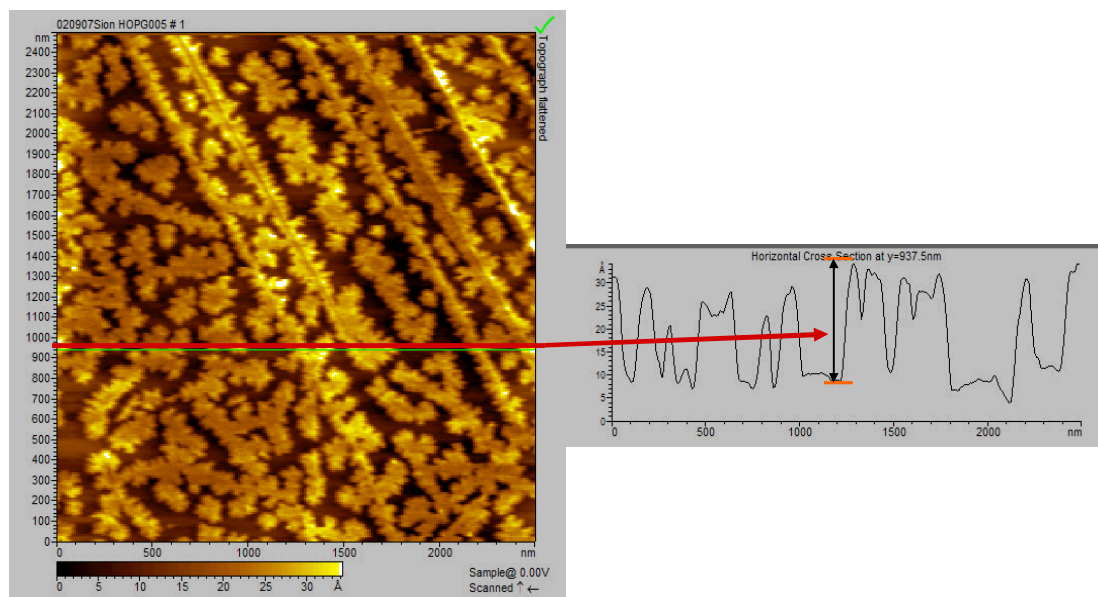
Fig. 3.4: AFM image of silicon nanoparticles on an HOPG witness sample. The particles collect to form "snowflake" like structures at the step edges of the HOPG due to the high mobility of the nanoparticles on the substrate. The particles are measured using the z-height, shown on the right, from the flat background of the HOPG.

transmission electron microscopy studies[6], and the size of the particles is determined by measuring the z height against the flat substrate. It is also evident from the images that the nanoparticles aggregate at the step edges of the HOPG. The Si nanoparticles collect at defect sites and step edges[7]. The top and bottom of the HOPG terraces do not have any dangling bonds and are atomically flat (reference?). This flat surface is an ideal substrate to be used in the determination of the sample sizes. The right side of figure 3.4 shows the z-height of the deposited nanoparticles for a cross section of the image. The z-height of many particles is measured to obtain a histogram of sizes. Then this data is fit to a Gaussian curve which indicates the size distribution of a particular sample, an example of which is displayed in figure 3.5.

Since HOPG is atomically flat over large regions, the silicon nanoparticles are very mobile on this surface. The high mobility of the nanoparticles allows them to form the snowflake-like structures observed in figure 3.4 that collect at the step edges of the HOPG. Comparable behavior has been reported for both silicon and antimony particles deposited on HOPG substrates[7,8], which has also been attributed to the high mobility of the particles on the atomically flat surfaces.[9]. Through experiments collecting evaporated nanoparticles on other substrates, we have observed that the nanoparticles are not mobile on surfaces such as oxidized silicon or germanium so obtaining separate isolated particles is possible on these surfaces[4].

During inert gas evaporation synthesis of the Si nanoparticles, it is assumed that particle formation occurs in the gas phase and not by nucleation on the surface of the substrate because no annealing is performed after the initial synthesis. Silicon atoms deposited on the surface in the absence of an annealing phase would have insufficient energy to form nanoparticles. Although the particles do aggregate at the step edges, the sizes of the particles do not depend on the features of the substrate. Particle sizes in
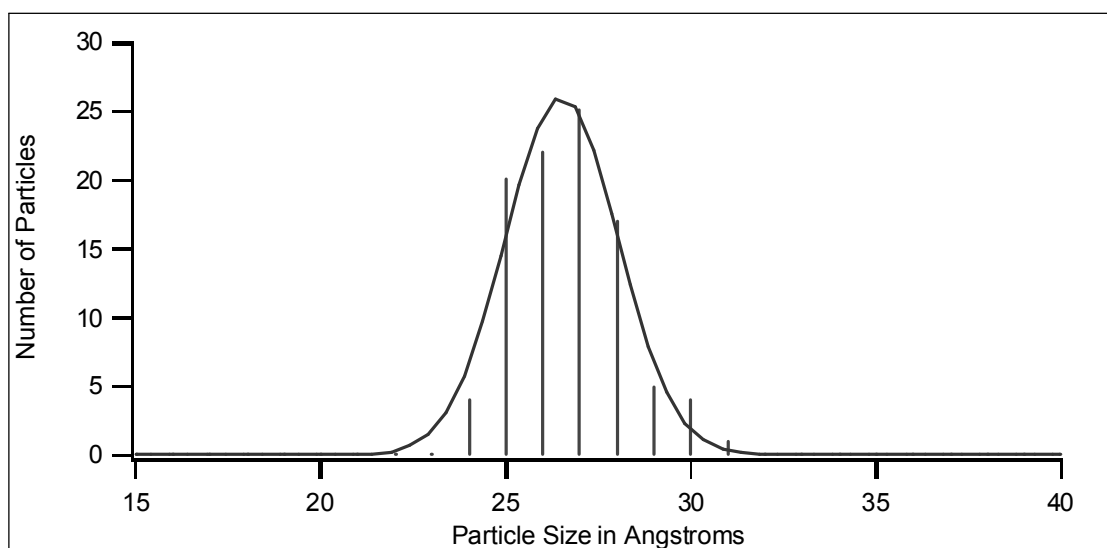
Fig. 3.5: A size distribution curve is determined from the histogram of sizes obtained from the AFM images of nanoparticles.

various regions of each HOPG substrate were measured and were found to be similar in size and morphology.

3.2 Synchrotron Radiation

Synchrotron radiation is the electromagnetic radiation produced by the acceleration of electrons traveling at a velocity close to, approximately 99.99 percent, the speed of light in a magnetic field. In a synchrotron radiation source large dipole magnets guide the electrons around a "curved" orbit within a storage ring. X-ray radiation is emitted tangentially to the curvature of the electron path in the magnetic fields of the ring. In reality, the electron storage "ring" is not circular but a many sided shape with straight sections in which insertion devices are placed to intensify the beam further. A schematic of the x-ray emission is observed in figure 3.6. Examples of insertion devices are undulators and wigglers, which differ from one another in the number and strength of the magnets they contain. These will be discussed further below.

The emitted radiation ranges from hard x-ray to infrared wavelengths, making it useful for many fields of research. Experiments in the fields of biology, chemistry, physics and materials science routinely performed at synchrotron sources. This wide range of scientific breadth makes user synchrotron facilities an extremely valuable resource. A range of energies can be utilized at individual beamlines which provides a significant advantage with respect to monochromatic laboratory x-ray sources.

Another advantage of using synchrotron radiation with respect to typical laboratory sources is the high intensity of the x-ray beam. The emitted x-ray intensities from various synchrotron facilities in the U.S. compared to common laboratory x-ray sources is shown in figure 3.7. The intensity and brightness of the synchrotron sources
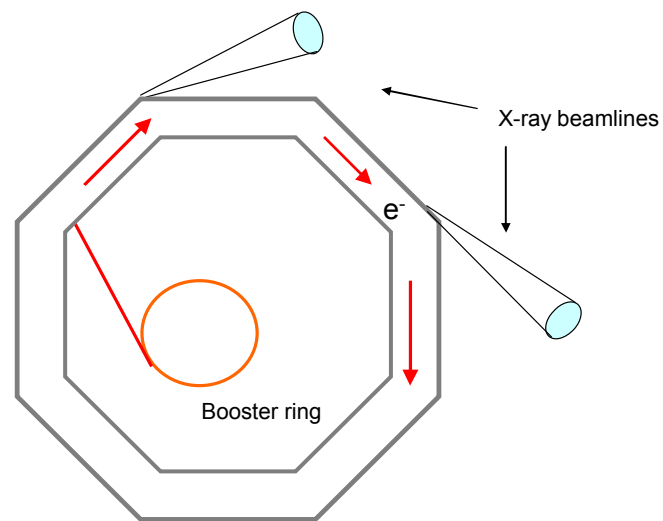
Fig. 3.6: Electrons are accelerated in a booster ring to relativistic speeds and directed around a curved path resulting in x-rays emitted at a tangent from the electron path. Modern day synchrotrons are actually many sided figures, to allow for insertion devices in the straight sections. The booster ring allows the electrons to be accelerated to relativistic speeds before injection into the electron ring.
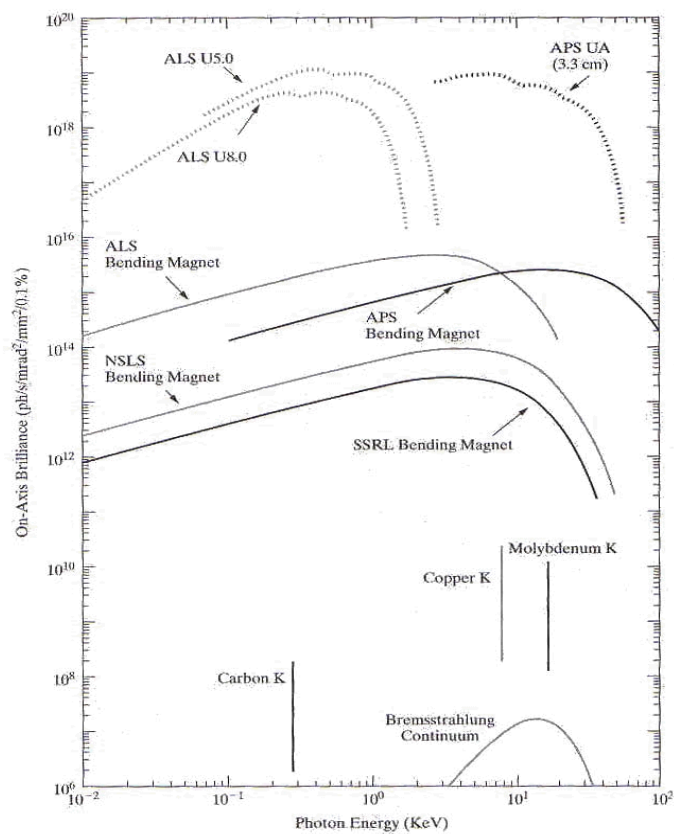
Fig. 3.7: Comparison of the intensities of many U.S. synchrotron light sources and some laboratory sources. Because of the high intensities of synchrotron sources, many experiments are possible that are not previously using low intensity laboratory sources. From Seah and Dench[10].

make them useful tools for many types of materials characterization. The use of high intensity synchrotron radiation can yield significant improvements in signal to noise, which enables the investigation of very small or dilute samples and can drastically reduce the time frame required to collect high quality data. While an experiment with a laboratory radiation source may take 30 minutes to several hours, the same experiment performed with a synchrotron source would take seconds. The associated increase in temporal resolution is essential for the study of fast processes within many fields of research including catalysis[11].

Although it was not utilized in this thesis, another benefit to synchrotron radiation is the capability of time resolution. The electrons orbit within the ring in perfectly timed bunches that allow time dependent experiments to be performed. As mentioned above, the electrons are steered within the storage ring using magnetic fields. Bend magnets curve the path of the electrons, thereby creating the tangential emitted x-ray radiation that is used in the experiments. To account for dispersion of the bend magnet radiation, mirrors are used to refocus the beam such that is has a small cross section at the sample surface. Meanwhile, a monochromator is used to obtain x-ray photons of the desired energy (and with a narrow spectral bandwidth)[12]. Radiation emitted from bend magnets have lower intensity than that emitted from undulators or wigglers. Using a bend magnet is sometimes preferred because damage to the sample is diminished with the lower intensity beam. When measuring samples that are easily damaged by the x-ray beam, such as organics, a bend magnet is often preferred. A schematic of bend magnet radiation is shown in figure 3.8.

In order to intensify the radiation, insertion devices are added to many experimental beamlines. Insertion devices are made up of many small magnets placed in the straight sections of the synchrotron ring and fall into two categories: wigglers and undulators. The focus here will be on undulators since this is the main type of insertion
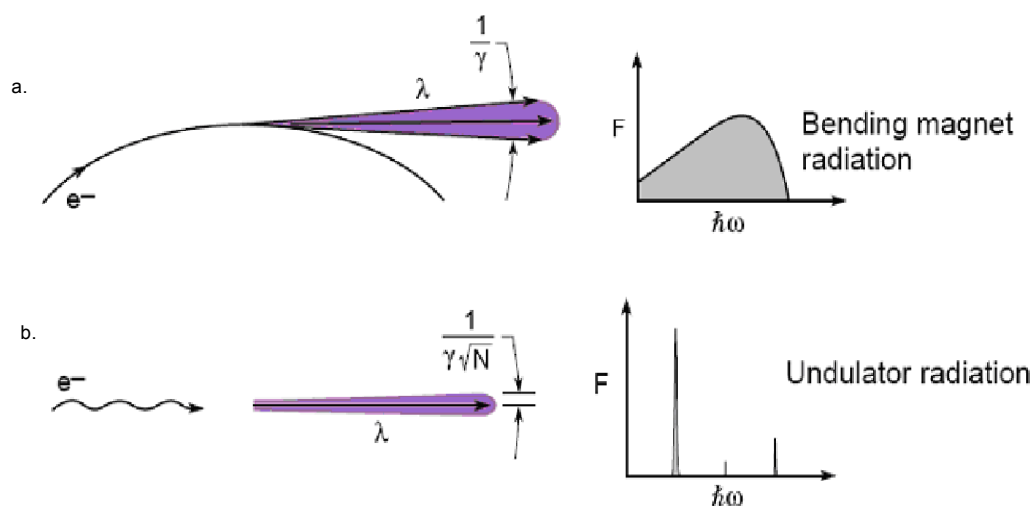
Fig. 3.8: a) Bend magnets cause x-rays to be emitted tangent from the electron ring. This type of magnet gives a broad energy range in a fairly narrow radiation cone. b) Undulators have many magnets put very close together on the top and bottom of the electron beam, this results in a very narrow cone of radiation at a very narrow, intense radiation wavelength said to be partially coherent and tunable. Reproduced from Attwood, Soft x-rays and extreme UV radiation: Principles and Applications[13].

device utilized in this thesis. Undulators are made up of many relatively weak magnets placed above and below the electron ring in opposite polarities. A schematic of the electron path and resulting radiation in an undulator is shown in figure 3.8 b. In this figure, the periods are shown as N, λ is the wavelength of light and γ is a source specific constant. The magnets cause the electrons to bend on multiple occasions in accordance with the number of periods in the undulator. As the electrons travel through the undulator, the periodic magnetic fields induce harmonic oscillations of each electron. Since the electrons are traveling close to the speed of light they can almost keep up with the light that was emitted when they pass through each period of the undulator. Thus, the light emitted at each period is added to at the next bend of the next period and the intensity of light increases. Because of the relative weakness of the magnetic fields, the electrons do not deviate significantly from their original path and, as a consequence, the width of the radiation cone and spectral bandwidth are small. More specifically, the beam dispersion of radiation from undulators is inversely related to the number of periods, N, in the device and the Lorentz contraction factor, γ, which is characteristic of the synchrotron facility[13]. Undulators also decrease the wavelength of the emitted x-rays. This also is dependent on the period, N, of the undulator and the Lorentz contraction factor, γ,

$$\lambda = \frac{\lambda_u}{2\gamma^2}$$
3.1

Where λ is the wavelength of the emitted light, λ_u is the period length of the undulator. Values of γ can be several thousand and are given by:

$$\gamma = 1957 E_e (GeV)$$
3.2

where E_e is the energy of the electron. For the ALS, the Lorentz contraction factor is 3720. A more detailed treatment of insertion devices is available elsewhere[13]. A

schematic of bend magnet and undulator radiation with their relative intensities and spectral bandwidth is provided in figure 3.8. These are the two types of beamlines used in this thesis.

Thus far only the process of producing x-rays in a synchrotron source has been discussed. Next the techniques which use this radiation will be covered. When an x-ray is incident on a sample many by products occur and can be detected, those include ejection of an auger electron, ejection of a core electron, emission of a valence electron etc. Through the analysis of these emitted electrons and photons information about the occupied and unoccupied density of states of the sample is obtained. Which then can be analyzed to map the partial local density of states of a sample both the conduction and valence bands must be studied.

3.3 X-ray Absorption Spectroscopy

X-ray absorption spectroscopy (XAS) is an element specific probe of the unoccupied density of states and the geometrical structure of a material. The energy of the incident x-ray photons is scanned across the binding energy of a core electron of a specific element. When the energy is sufficient to promote an electron from the core level into the lowest lying empty state, the photon is absorbed and a corresponding edge is observed in the absorption spectrum. A schematic of this process is in figure 3.9. This edge region is also called x-ray absorption near edge structure (XANES) or near edge x-ray absorption spectroscopy (NEXAFS) in low Z materials such as carbon. As the photon energy is increased, the electrons are promoted electrons into higher energy vacant states. The XANES/NEXAFS continues until the energy is reached at which the
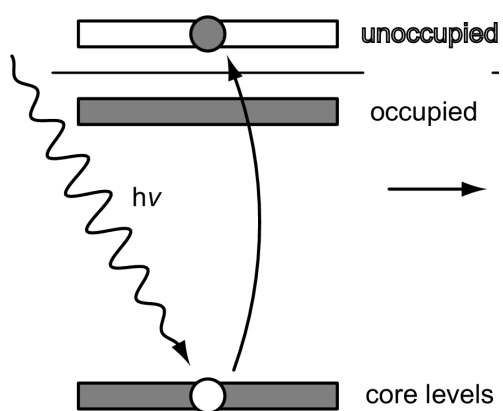
Fig. 3.9: X-ray absorption spectroscopy (XAS) excites an electron into the conduction band and the resulting electron emitted from filling the core hole is detected in this spectroscopy.

photoelectron is emitted from the atom. At this point is the extended x-ray absorption fine structure (EXAFS) which extends up to 1000 eV beyond the absorption edge. EXAFS peaks occur due the scattering and backscattering of photoelectron waves produced when an electron is ionized with more energy than necessary to just eject the electron. Because energy must be conserved the excess energy is converted to a photoelectron wave. This wave scatters out towards other atoms in the material and is backscattered[11]. In this region of the spectrum specific information about the coordination and local atomic structure of the sample can be obtained. In this thesis, the samples will only be characterized using XANES.

The probability of a transition from the initial to final state, $W_{i\text{-}f}$, occurring is given by Fermi's Golden rule:

$$W_{i-f} \propto \frac{2\pi}{\eta} \left| \langle f | H' | i \rangle \right|^2 Q_f(E)$$

3.3

where $\left| \langle f | H' | i \rangle \right|$ is the matrix element of the perturbation H' and Q_f (E) is the density of final states[14].

The bulk silicon $L_{2,3}$ absorption spectrum directly probes the transition probability which then maps the unoccupied density of states (DOS) as shown in the band diagram of figure 3.10a. The absorption $L_{2,3}$ edge of silicon nanoparticles will be probed in this thesis work. A characteristic $L_{2,3}$ edge Si absorption edge x-ray absorption spectrum for bulk Si is displayed in figure 3.10b. The $L_{2,3}$ Si absorption edges for the bulk material are observed at a well-defined absorption onset of 99.84 eV[15]. The $L_{2,3}$-edges formally correspond to the promotion of a 2p electron into vacant s- and d- states according to the dipole selection rules for conservation of angular momentum, $\Delta l = \pm 1$. The $L_{2,3}$ edge of Si maps the partial density of unoccupied states, called the conduction band in semiconductor materials. At this edge movement of the bottom of the conduction band

can be detected. Because the original excited electron is from a core, localized state, the local partial density of states (LPDOS) is determined by these measurements.

Beyond a well-defined onset energy, the $L_{2,3}$ absorption edges for bulk Si exhibit a series of characteristic features. These can be assigned via comparison with the energy diagram obtained from the theoretical treatments, figure 3.10a. The conduction band minimum at X_1 corresponds to the absorption edge onset. The edge itself has a shoulder which is due to the spin-orbit splitting of the 2p degenerate states into $2p_{3/2}$ (A) and $2p_{1/2}$ (B). These two peaks, with a separation of 0.6 eV, are too close to be completely resolved from each other in the spectrum. At the top of the edge are a pair of spin-orbit split features (C) that correspond to absorption to the $L_1 \rightarrow \Gamma_{15}$ flat band state. The two features observed at approximately 102.6 eV (D) result from absorption to the $L_3 \rightarrow \Gamma_{15}$ flat band states[16]. At higher energy, ~106 eV, some broad peaks often appear that correspond to SiO_2. Silicon is usually etched to remove the native oxide but a small amount can re-form due to rapid oxidation in air prior to measurement.

Several different things happen in an atom when an x-ray photon is absorbed. Initially, promotion of the core electron into the conduction band creates a core hole. The hole is then filled by an electron from higher energy filled (valence) states and the energy from this action is emitted via either radiative or non-radiative processes. In the radiative process a photon is emitted. In non-radiative processes the energy is transferred to another electron and because of conservation of momentum, the second electron is ejected from the atom. This is referred to as Auger emission[13], a schematic of this process is illustrated in figure 3.11a. These emitted particles are called electron products and are proportional to absorption of x-rays in the atom. The electron products can be detected to observe the x-ray absorption spectra.
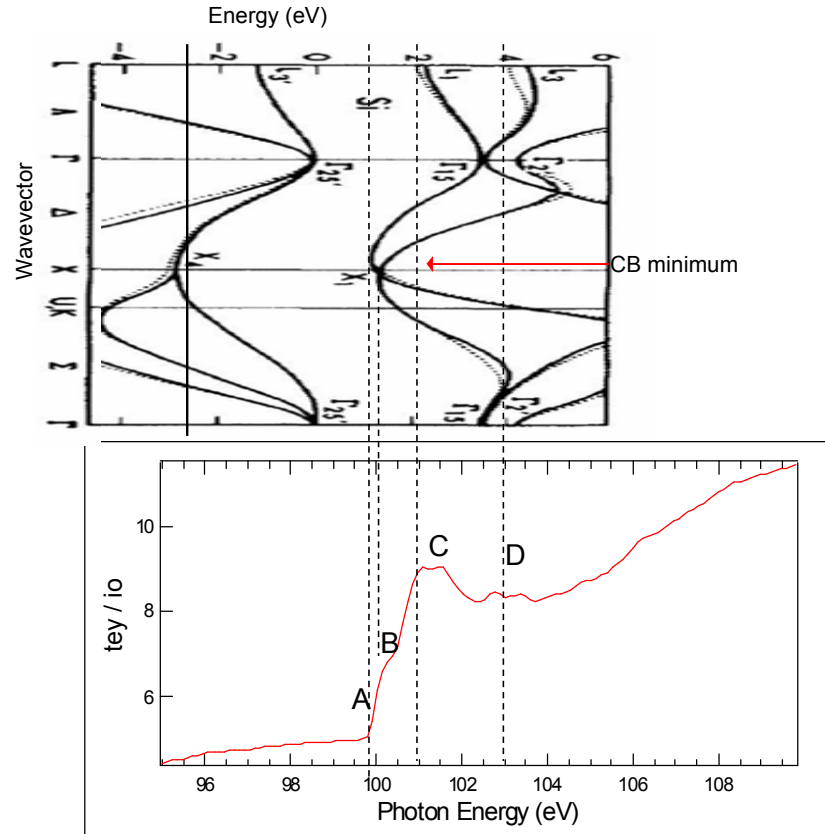
Fig. 3.10: a) Typical x-ray absorption spectrum of the bulk Si $L_{2,3}$ edge correlated to the b) band diagram. The edge onset corresponds to the conduction band minimum shown on the band diagram as X_1. The structure at the top of the peak is a transition $L_1 \rightarrow \Gamma_{15}$ feature and that just beyond the edge around 103 eV, corresponds to the flat band transition $L_3 \rightarrow \Gamma_{15}$[15,16]. Band diagram is reproduced from the psuedopotential calculations of Chelikowsky[17].
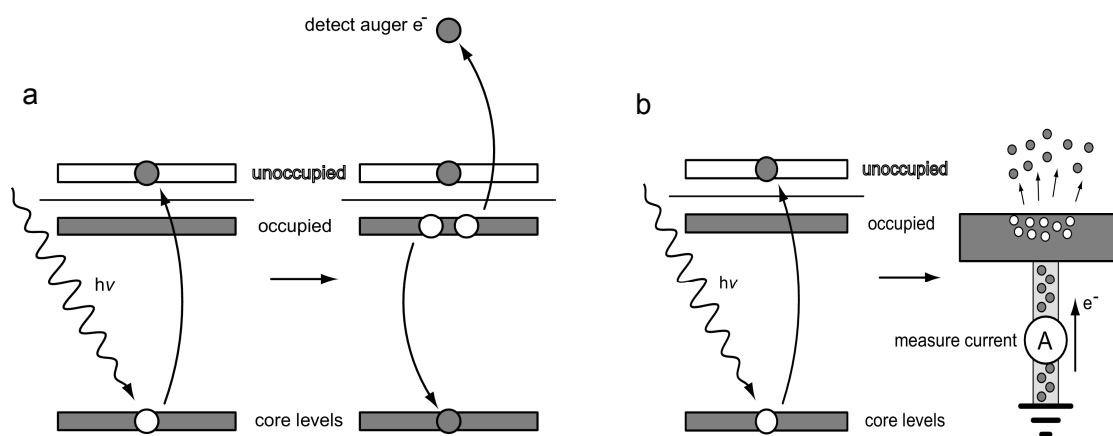
Fig. 3.11: a) Auger electrons are emitted due to conservation of momentum from a two step process. First, a photon ejects an electron from an inner shell to an outer one. Second, an electron fills the hole and an Auger electron is emitted. b) Total electron yield (TEY) measures all electrons emitted from the sample including Auger and subsequent secondary electrons. After the original Auger electron is ejected secondary electrons are created from backscattering. The current is then amplified to collect the signal.

$$\alpha \approx core \quad hole \quad transitions \approx electron \quad products \qquad\qquad 3.3$$

where α is the absorption cross section that dictates how much the material absorbs electrons.

There are several methods for detecting XAS, which include the transmission, electron yield and fluorescence yield modes. The degree of transmission is measured by comparing the x-ray flux before and after the beam passes through a very thin sample. The intensity of the x-ray beam is typically measured as a current from ionization chambers or metal grids/films positioned directly in front of and behind the sample interest. The beam intensity downstream from the sample is called "I zero" (I_0). In the soft x-ray regime, the products produced from x-ray absorption in a material, electrons and photons, are generally measured rather than the transmitted x-ray beam. This is due to the low cross section of electrons in most materials which would necessitate the preparation of extremely thin samples for transmission experiments.

One method of measuring the electron yield produced from an absorption event is to simply measure the current from a grounded sample as it is irradiated by the x-rays from the synchrotron source. As an alternative, one can measure the Auger electrons emitted from the sample. Since the Auger electrons emitted under irradiation have very low kinetic energies in the soft x-ray region of the spectrum, only electrons up to 5-10 Å from the sample surface are emitted and can be measured as a surface sensitive technique, Auger electron spectroscopy (AES). This penetration depth is determined by the scattering cross section which has been found to be similar to most elements at specific energies and is given by the universal curve as determined by Seah and Dench[10]. This curve is shown in figure 3.12. To obtain a more bulk sensitive measurement, the current flowing to the sample to quench the holes produced by
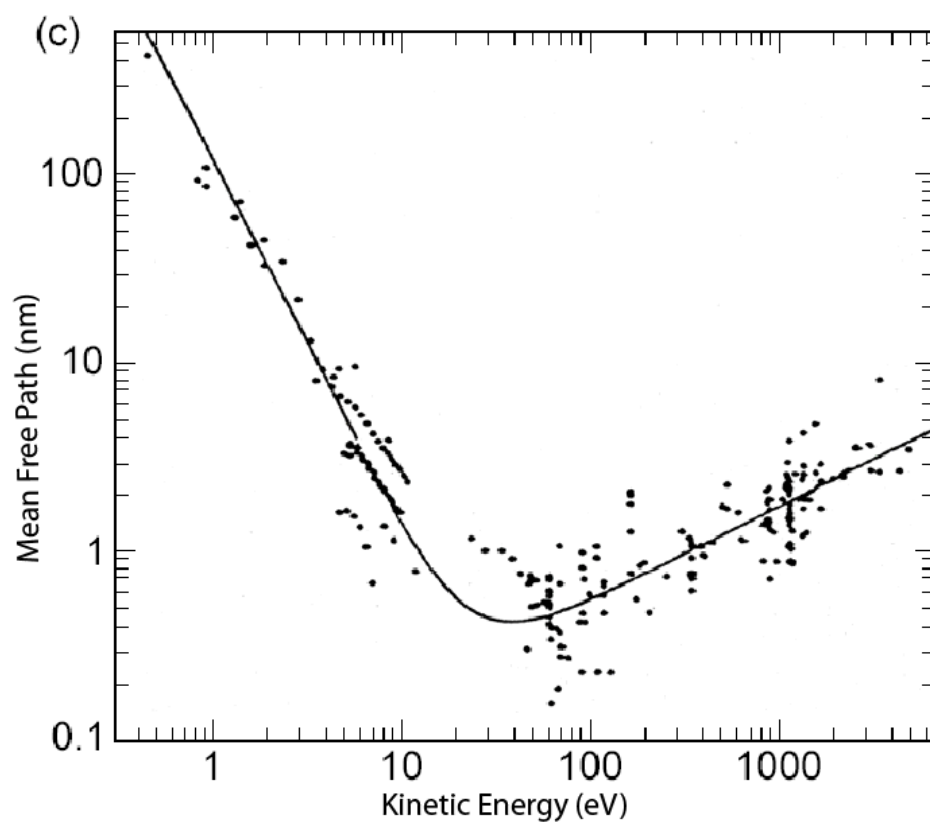
Fig. 3.12: The universal curve shows the mean free path of electrons which correlates to the penetration depth in a sample by kinetic energy. This is called the universal curve because most elements fall on this curve. From Seah and Dench[10].

electrons escaping the sample surface into vacuum is obtained. This is called total electron yield (TEY). The electrons are collected by simply measuring the current to the sample as it is irradiated with x-rays. This process is shown in figure 3.11b. The simplicity of data collection makes XAS in total electron yield a popular and effective characterization method. In this research total electron yield (TEY) will be used predominantly as the signal is large and it can penetrate deep enough to investigate the bulk of the small nanoparticles.

One can also measure the fluorescence photons emitted from the sample of interest to obtain the fluorescence yield (TFY). The fluorescence photons have much greater escape depths than the Auger electrons and, as such, the TFY signal is more sensitive to bulk than AES. Although a wide variety of detectors can be used to detect the fluorescence photons, channel plates have been used to obtain the data presented in this thesis. Significantly, the fluorescence yield signal is often very small with respect to the TEY or AES signals for low-Z elements, including silicon. This is due to higher yields of Auger emission vs. fluorescence in lower Z elements, as illustrated by the graph in figure 3.13. It is often useful to record the TFY and TEY signals simultaneously to provide as a comparison between the bulk and surface of the material of study. X-ray absorption spectroscopy (XAS) is a powerful, element specific technique used for the electronic structure characterization of the conduction band in this project. The absorption edge of XAS gives information about the unfilled electronic states in the atom.
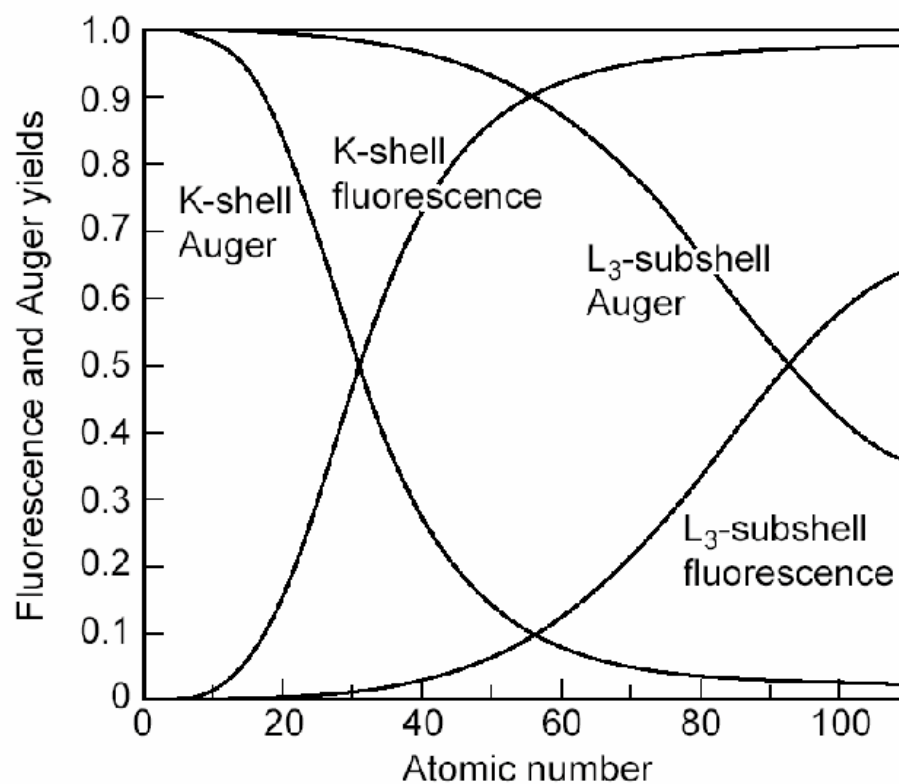
Fig. 3.13: Yields of fluorescence and Auger emittance by atomic number. Lower atomic numbers yield lower fluorescence and higher Auger electrons. From Attwood[13].

3.4 Soft X-ray Fluorescence (SXF)

In soft x-ray fluorescence spectroscopy (SXF), incident x-rays excite core electrons into the unoccupied states leaving a hole in the core. This hole is filled by an electron from the occupied states which releases energy. This energy is frequently released radiatively as fluorescence. In SXF, the fluorescence photons are detected and mapped according to the energy of the fluorescence. This technique is used to probe the highest energy filled states, called the valence band in a semiconductor. By changing the energy of the incident radiation one can probe the exact energy of interest within the valence band. This process is depicted in figure 3.14. As in XAS, the localization of the core hole makes SXF an element specific technique.

Due to low the fluorescence yields and generally low efficiencies of SXF detectors, it is necessary to use synchrotron radiation for these measurements to improve the signal to noise ratio[18]. However, when using synchrotron radiation, silicon exhibits a clear, strong emission spectrum thus making it possible to analyze even dilute samples of silicon using SXF. In this experiment, the sample is irradiated at slightly higher energies than the Si L_2 absorption edge to ensure excitation of only the valence electrons within the sample and not any electrons from the surface oxide contaminant. Emission spectra are then recorded at multiple excitation energies to map out the transition from the valence band to the silicon $2p_{3/2}$ core hole. This technique is also bulk sensitive because the mean free path of photons is larger than that of electrons. This bulk measurement allows us to probe the crystalline Si core rather than surface oxide. This gives SXF an advantage over photoemission spectroscopy which utilizes electrons for measurement.
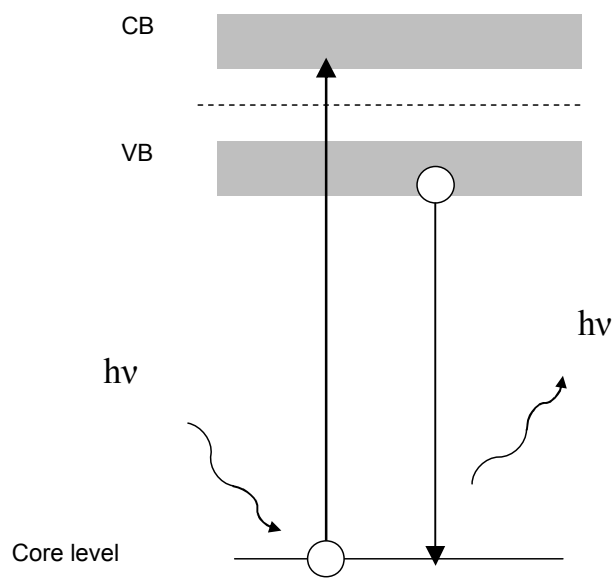
Fig. 3.14: In soft x-ray fluorescence (SXF) a core electron is excited into the valence band and the emitted fluorescence spectroscopy is measured in this spectroscopy.

As with XAS, bulk Si has a characteristic SXF spectrum, an example of which is presented in figure 3.15b. This spectrum has three peaks, marked A, B and C on the spectrum. The low energy peak (A) consists of low lying 3s states and the center peak (B) consists of s-p hybridized states. The onset of the high energy peak (C) gives the position of the valence band maximum as correlated to the band diagram, 3.15a. This peak is corresponds to p states within the valence band[19]. It may seem strange that p states are probed given the $\Delta l = \pm 1$ selection rule, but it is the hybridization with the s-states that makes this possible. Both the $2p_{3/2}$ and $2p_{1/2}$ states contribute to the bulk Si spectrum as the sample has been irradiated at an excitation energy of 105 eV, far above the absorption onset. The excitation energy of the SXF spectra is important, because of energy dependent features which are excited under resonant excitation conditions. This is evident in resonant inelastic x-ray spectroscopy (RIXS). RIXS is scattering that leads to a valence electron-hole pair in the final state and provides additional information about the wavevector, which complements the local partial density of states information obtained by XAS and SXF. The spectral shape in the RIXS region varies by excitation energy[19]. This region occurs at the energy where the L_2 contribution to the edge is no longer excited but the L_3 is still excited (around 100 eV).

By combining SXF (valence band maximum) and XAS (conduction band minimum) spectra the entire band gap can be mapped. This band gap be used for comparison with band gap information obtained from optical techniques, which is often complicated by substrate or matrix contributions to the luminescence[20].
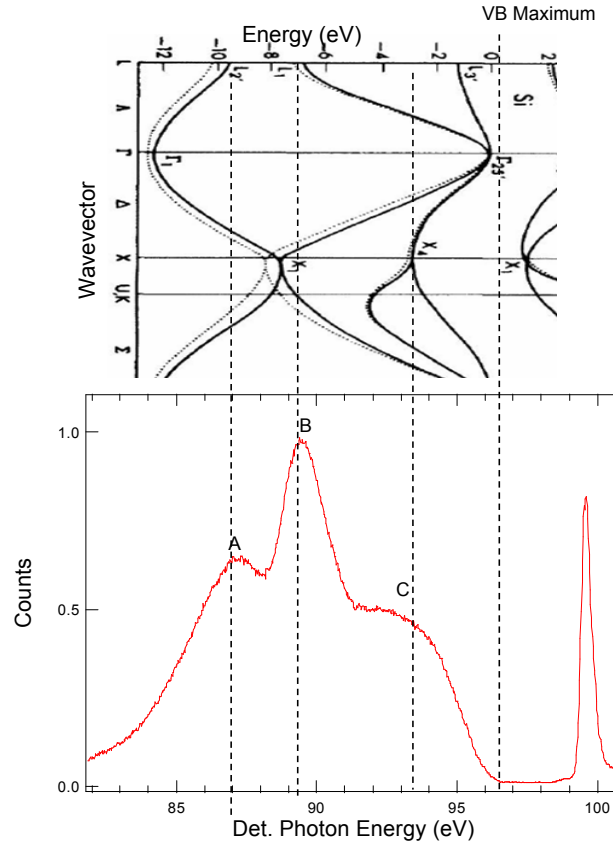
Fig. 3.15: Silicon L$_{2,3}$ emission edge with peaks corresponding to a calculated band diagram as connected via the dashed lines. The spectrum has three characteristic peaks labeled A, B and C which correspond to s states, s-p hybrid states and p like states, respectively. Band diagram reproduced from Chelikowsky[17].

3.5 Beamlines and Experimental Analysis Chambers

The research presented in this thesis was performed at two beamlines, which are located at different synchrotron sources. These beamlines are 8.2 at the Stanford Synchrotron Radiation Laboratory (SSRL) at the Stanford Linear Accelerator and 8.0 at the Advanced Light Source (ALS) in Lawrence Berkeley National Laboratory.

Beamline 8.2 at SSRL is located on a bend magnet. The experimental chamber at this beamline is equipped to perform x-ray absorption with measurements in the TEY and AES modes.

Beamline 8.0 at the ALS is located on a straight section of the storage ring that contains an undulator for producing partially coherent and tunable radiation. A schematic of this beamline can be observed in figure 3.16 and a picture in figure 3.17. Beamline 8.0 provides the capability for performing XAS in both the total electron yield and fluorescence yield modes. This beamline is also equipped with a Rowland circle grating spectrometer with a photon counting area detector which is used for soft x-ray fluorescence (SXF)[21].

Characterization
Chamber

Focusing mirror

Switchyard

Exit slit

Branch line to other analysis
chambers

Entrance slit

M_0 Mirror

Spherical gratings for
selecting energy range

Undulator

Barn Doors

X-ray beam
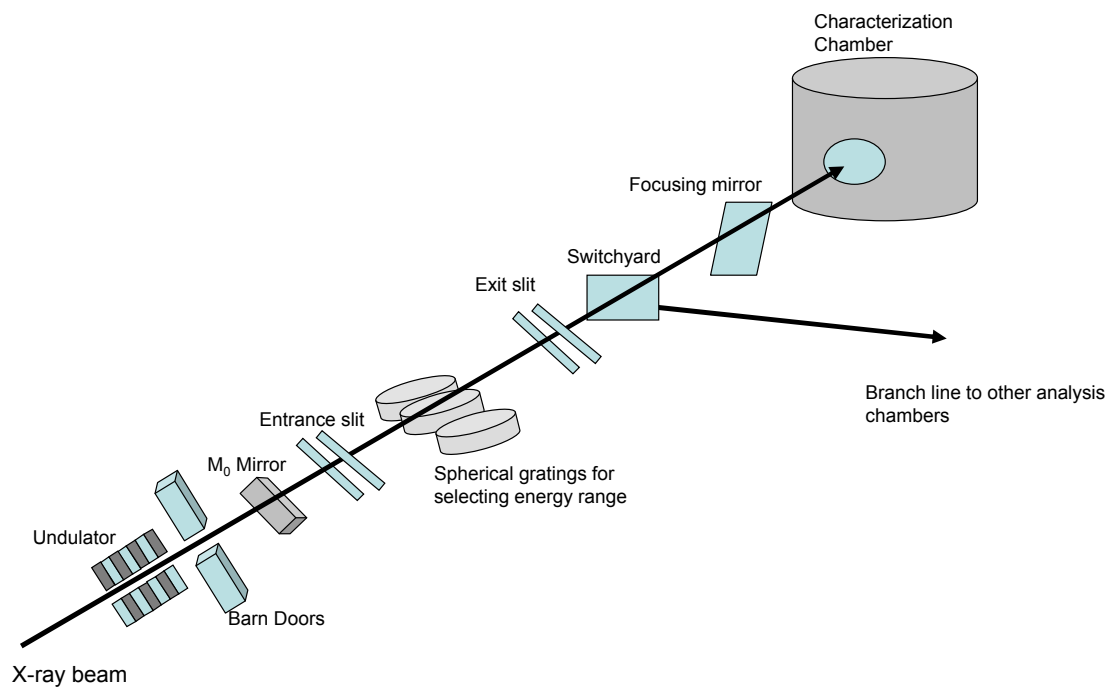
Fig. 3.16: Simplified schematic of beamline 8.0 at the advanced light source in Lawrence Berkeley National Laboratory. The x-rays from the undulator are first focused by the M0 mirror and then energy selected by the spherical gratings. Just before the characterization chamber, the beam is focused again by a vertical focusing mirror. Additional control over the energy resolution can be obtained by limiting the incident light with entrance and exit slits.
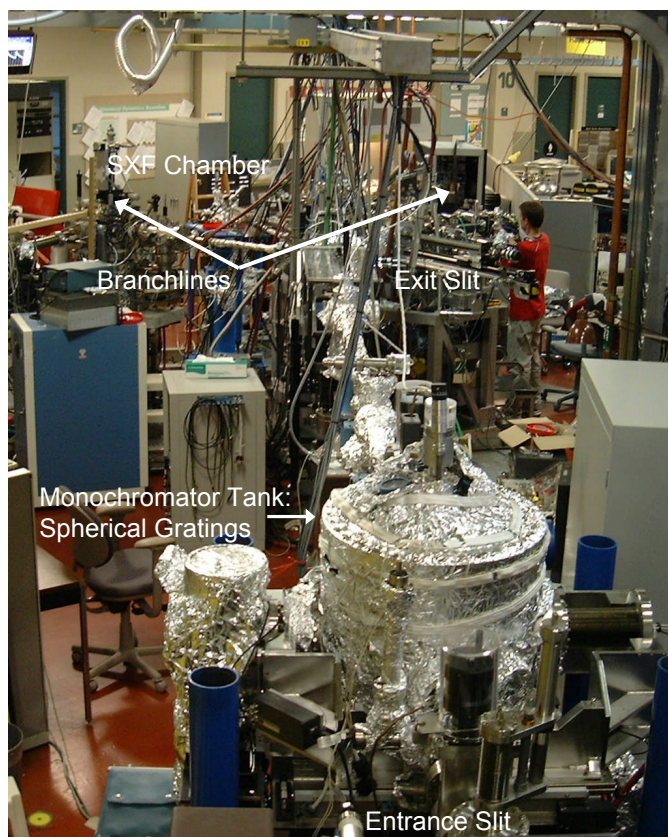
Fig. 3.17: Picture of beamline 8.0 at ALS**.** The major components of the beamline are labeled.

References

[1]   G. Binnig, Quate, C.F., Gerber, Ch., "Atomic Force Microscope," Physical review letters **56** (9), 930 (1986).

[2]   C. Rigetti, (Molecular Imaging).

[3]   Q. Zhong, Innuss, D., Kjoller, K., Elings, V.B., "Fractured polymer / silica fiber surface studied by tapping mode atomic force microscopy," Surface Science Letters **290**, L688-L692 (1993).

[4]   C. Bostedt, University of Hamburg, 2002.

[5]   G.L. Miessler and D.A Tarr, *Inorganic Chemistry*. (Prentice Hall, Upper Saddle River, NJ, 2000).

[6]   T. van Buuren, Dinh, L.N., Chase, L.L., Siekhaus, W.J., Terminello, L.J., "Changes in the electronic properties of si nanocrystals as a function of particle size," Physical Review Letters **80** (17), 3805 (1998).

[7]   P. Scheier, Marsen, B., Lonfat, M., Schneider, W.-D., Sattler, K., "Growth of Silicon Nanostructures on Graphite," Surface Science **458**, 113 (2000).

[8]   M. Heyde, Cappella, B., Sturm, H., Ritter, C., Rademann, K., "Dislocation of antimony clusters on graphite by means of dynamic plowing nanolithography," Surface Science **476**, 54-62 (2001).

[9]   S.S. Kushvaha, Yan, Z., Xiao, W., Wang, X-S., "Surface morphology of crystalline antimony islands on graphite at room temperature," Journal of physics:Condensed matter **18** (12), 3425 (2006).

[10]   M.P Seah, Dench, W.A., "Quantitative electron spectroscopy of surfaces: A standard data base for electron inelastic mean free paths in solids," Surface and interface analysis **1** (1979).

[11]   Robert A. Scott, *Physical methods in bioinorganic chemistry: spectroscopy and magnetism*. (University Science Books, Sausalito, Calif., 2000), pp.465-505.

[12]   K.G. Tirsell, Karpenko, V.P., "A genral purpose sub-keV x-ray facility at the stanford synchrotron radiation laboratory," Nuclear instruments and methods in physics research **A291**, 511-517 (1990).

[13]   D. Attwood, *Soft X-rays and Extreme Ultraviolet Radiation: Principles and Applications*. (Cambridge University Press, 1999).

[14]   Joachim Stohr, *NEXAFS Spectroscopy*, 1st ed. (Springer-Verlag, Berlin, 1992), p.403.

[15]   P.E. Batson, "Silicon $L_{2,3}$ near-edge fine structure in confined volumes," Ultramicroscopy **50**, 1-12 (1993).

[16]   A. Bianconi, R. Del Sole, A. Selloni et al., "PARTIAL DENSITY OF UNOCCUPIED STATES AND $L_{2,3}$-X-RAY ABSORPTION SPECTRUM OF BULK SILICON AND OF THE Si(1 1 1) 2 x 1 SURFACE," Solid State Communications **64** (10), 1313 (1987).

[17]   Cohen Chelikowsky J., M., "Nonlocal pseudopotential calculations for the electronic structure of eleven diamond and zinc-blende semiconductors," Physical Review B **14** (2), 556 (1976).

[18]   J. Nordgren, Wassdahl, N., "Soft x-ray fluorescence spectroscopy using tunable synchrotron radiation," Journal of electron spectroscopy and related phenomena **72**, 273 (1995).

[19]   Luning J. Eisebitt S., Rubensson J.E., Settels, A., Dederichs, P.H., Eberhardt W., Patitsas S.N., Tiedge T., "Resonant inelastic soft x-ray scattering at the Si L_3 edge experiment and theory," Journal of electron spectroscopy and related phenomena **93**, 245-250 (1998).

[20]   G. Santana, Monroy, B.M., Ortiz, A., Huerta, L., Alonso, J.C., Fandino, J., Aguilar-Hernandez, J., Hoyos, E., Cruz-Gandarilla, F., Contreras-Puentes, G., "Influence of the surrounding host in obtaining tunable and strong visible photoluminescence from silicon nanoparticles," Applied physics letters **88**, 041916 (2006).

[21]   J.J. Jia, Callcott, T.A., Yurkas, J., Ellis, A.W., Himpsel, F.J., Samant, M.G., Stohr, J., Ederer, D.L., Carlisle, J.A., Hudson, E.A., Terminello, L.J., Shuh, D.K., Perera, R.C.C., "First experimental results from IBM/TENN/TULANE/LLNL/LBL undulator beamline at the advanced light source," Review of scientific instruments **66** (2), 1394 (1995).

Chapter 4:

Inert Gas Evaporation Sample Synthesis

Using the thermal evaporation synthesis, nanoparticles were produced and deposited onto a substrate for subsequent characterization. The size of the nanoparticles produced was controlled through changing the synthesis temperature. The size and morphology of the nanoparticles were characterized using AFM. Narrow size distributions were obtained using this synthesis.

4.1 Previous research

Inert gas evaporation is well suited for nanoparticle synthesis and any subsequent characterization due to the capability of the technique to produce large amounts of sample with small size distributions and a wide range of possible sizes. Another benefit to this synthesis is the ability to produce clean particles in a vacuum and, without exposure to atmosphere, apply characterization techniques. It is also possible to change the surface chemistry in-situ in order to investigate the effects of surface passivation on the nanoparticle properties.

Metal nanoparticles have been prepared by inert gas evaporation for over 85 years. Beeck et. al. [1] performed evaporations in an inert atmosphere in 1940 and their primary interest was in the catalytic properties of the thin films that were created. The technique can be summarized as follows: a metal is heated in a crucible past its melting point in an inert gas, He or Ar, atmosphere. The evaporated metal collides with the inert gas molecules that cool the metal vapor quickly. The rapid cooling of the metal vapor allows for the nucleation size to be very small, as determined by Granqvist et. al.[2] The

evaporated metal creates a "smoke plume" above the crucible in which certain regions create different sizes of particles[3]. Generally, the smallest particles are produced in an area around 2 cm above the crucible[2]. Thus, the sample substrate is placed in this region when preparing nanoparticles. Convection currents can carry the particles further from the crucible within the chamber. In more recent studies on evaporated silicon nanoparticles, quantum confinement effects have been identified in PL measurements and XAS and SXF measurements of the electronic structure[4]. In particular, studies performed by van Buuren et. al. showed size dependent conduction and valence band shifts. The band edges shifted with an inverse exponential relationship to the size[5].

Gas evaporation has been identified as an excellent means of synthesizing nanoparticles due to the fact that it fulfills the four main criteria identified by Granqvist and Buhrman[2]. These criteria are: the ability to 1) form nanoparticles with sizes less than 10 nm, 2) generate nanoparticle samples with small size distributions, 3) produce electrically isolated particles and 4) produce large amounts of sample (up to 1 g). Our group has identified an additional criterion that is also fulfilled: the ability to change surface chemistry, which enables the study of surface effects and use of the material in various applications. Since these are all satisfied with the gas evaporation synthesis, it has been used to produce silicon nanoparticles in this project. As mentioned earlier, silicon and other group IV nanoparticles are not easily synthesized in large amounts with easily modified surfaces and this synthesis fulfills all of the relevant criteria.

4.2 Inert Gas Evaporation: Experimental Chamber

The samples are transferred into the synthesis chamber via a transfer arm within a bellows. The experimental chamber was set up and designed by Christoph Bostedt
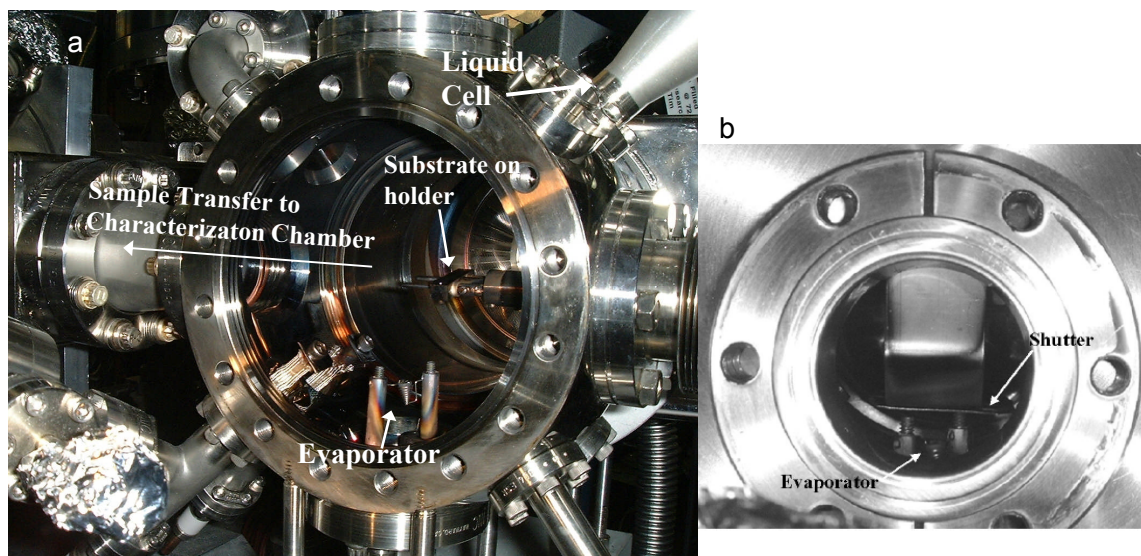
Fig. 4.1: a) Experimental synthesis chamber used in thermal evaporation synthesis of nanoparticles. The components of the chamber are labeled. b) The shutter is shown. This allows for short deposition times.

and a detailed description of it is given in his PhD thesis[6]. A picture of this chamber is shown in figure 4.1 and the components that will be discussed are labeled.   All syntheses of the silicon nanoparticles were performed in a small, 5" inner diameter, chamber with a turbo pump attached to one side port that is backed by a dry roughing pump. These pumps can be isolated from the chamber via a valve which allows for back filling of the chamber with buffer gas during nanoparticle synthesis. The small size of the chamber and large pumping capacity of the turbo pump allow the chamber to be evacuated quickly after the synthesis is performed. A leak valve connected to a helium lecture bottle is also attached to the chamber in order to fill the chamber with buffer gas. Meanwhile, a leak valve and liquid cell enable alcohols or other molecules to be introduced to the experimental chamber for passivation of the Si nanocrystals.

A high current feed-through on a 2 ¾" flange holds the tungsten wire filament. A small boron nitride crucible fits securely into the basket of the filament to ensure even heating of the contents of the crucible. The crucible is filled with pieces of bulk silicon wafers prior to evaporation. Current is flowed through the filament to resistively heat the silicon in the crucible and induce evaporation. A manual shutter is positioned between the evaporator and the substrate to allow for control of the deposition time and to prevent convection currents from forming.

The entire experimental setup is contained in a very small vacuum chamber allowing for a high-vacuum environment which ensures minimal contamination of the nanoparticles. In addition, the synthesis chamber is small enough to be transported to various synchrotron and laboratory based chambers to provide the capability for an in-situ synthesis and characterization set up. The use of a vacuum synthesis method allows the nanoparticles to be synthesized and characterized without contaminating or exposing the particles to air. The results of these studies will be discussed in the following chapter.
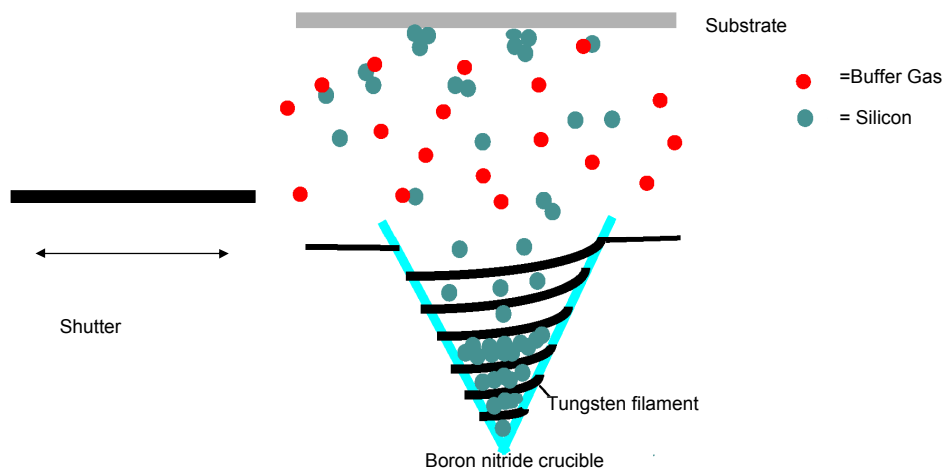
Fig. 4.2: Schematic of the inert gas evaporation synthesis experimental setup. Silicon is evaporated in the presence of a buffer gas. Ballistic collisions with the buffer gas cause the silicon to condense to form nano-sized particles.

4.3 Experimental Method

In gas evaporation synthesis of silicon nanoparticles, the bulk silicon is evaporated from a small boron nitride crucible placed in a tungsten filament. A schematic of the experimental setup can be seen in figure 4.2. Silicon is highly reactive and wets most materials. As a consequence, boron nitride is used because of its high thermal conductivity and low reactivity with silicon. In the process of synthesizing the nanoparticles, the chamber is first back filled with an inert, buffer gas such as helium or argon to a pressure of 250 mTorr. Since the chamber is back filled with buffer gas to a pressure around 10^{-1}-10^{-2} the temperature to which the silicon must be heated in order to create silicon vapor may change. From figure 4.3, a plot of vapor pressure as a function of temperature, it is evident that the silicon must be heated to a temperature between 1500-1800 ˚C to produce particles[6]. Hence, the filament is resistively heated to a temperature within this region to produce Si vapor. The molten silicon is reactive and has a high mobility. It should also be noted that the evaporation current is carefully controlled to be only a few amperes above the melting current because it has also been observed that with enough input energy the silicon can "jump" out of the crucible. The silicon is, at this point, in a supersaturated vapor phase in the buffer gas filled chamber. The buffer gas collides with the silicon atoms and condensation occurs. A substrate placed approximately two centimeters above the crucible collects the atoms as they cool and aggregate into nanometer sized particles. A shutter in the synthesis chamber between the crucible and the collection substrate limits the collection time and stops convection currents from interfering with the synthesis. The shutter is opened only for a few seconds depending on the amount of sample required.

Once the particles reach the substrate surface, no other aggregation or deformation of shape occurs. Some substrates such as HOPG, highly oriented pyrolytic graphite, which do not have many surface bonds available and are atomically flat, allow
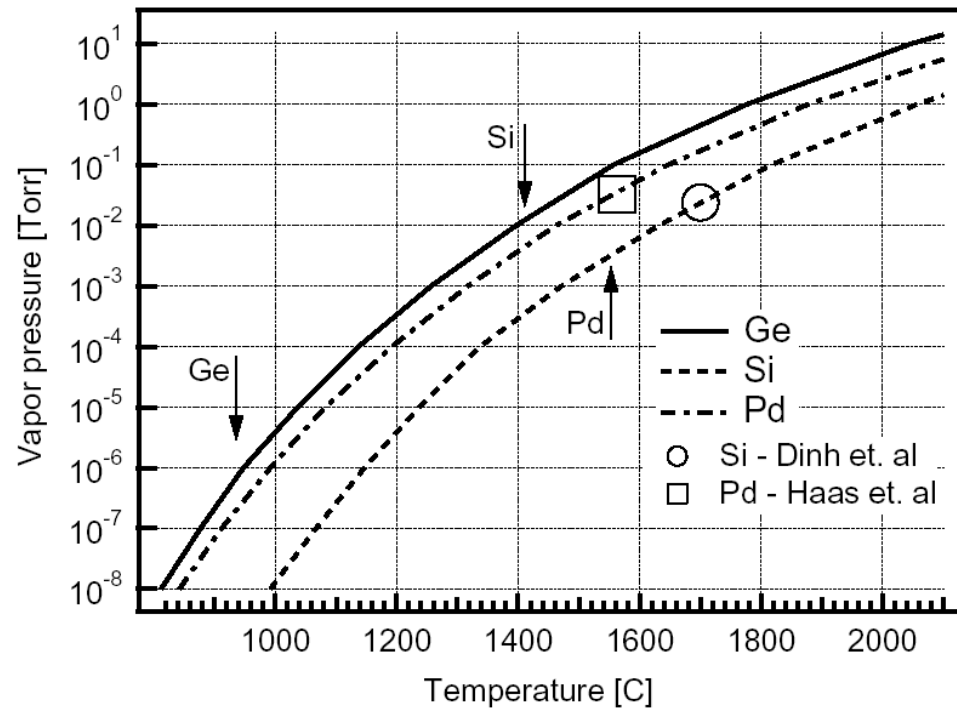
Fig. 4.3: Vapor pressure as function of temperature for silicon, germanium and palladium The melting points of germanium, silicon and palladium are marked with arrows. The vapor pressure data is reproduced Brunner and Batzer[7].

the particles to further form "snowflake" like structures along the step edges.   This grouping is due the high mobility of the particles on the surface and is not indicative of further bonding occurring with the particles. Other substrates, such as polished silicon wafers, have shown that isolated, single, spherical particles form during gas phase synthesis [8].   Passivation of the particles can be achieved using in several methods. In this project, the surfaces were passivated using alcohols evaporated into the experimental chamber through a leak valve with the attached liquid cell. This method has previously been used to passivate clean silicon wafer surfaces by Lay et. al.[9] who found that it resulted in a high level of passivation of the dangling bonds. Our group has also reported that germanium nanoparticles can be passivated using the same method[10].

The majority of the experimental approaches described in the previous paragraphs can be used to synthesize nanoparticles of other materials. In fact, the specific experimental setup presented in this work was previously used by Bostedt to synthesize Ge nanoparticles [6].

4.4 Parameters for the Synthesis of Silicon Nanoparticles

Using the gas evaporation synthesis, it is possible to control the particle sizes by varying either the pressure of the buffer gas in the experimental chamber or the collection temperature via the evaporator current. In previous experiments, variation in the pressure provided excellent control over the particle size[5] but more recent studies on germanium nanoparticles have demonstrated that current variation is a more reproducible, stable method for changing the particle size[6]. Other variables, such as the choice of filament, buffer gas and current can also influence the experimental results.

The effect of these parameters on the synthesis of Si nanoparticles will be discussed further below.

An important variable in this synthesis is the buffer gas used. Although argon and helium have both been used as the buffer gas for gas condensation experiments, it has been demonstrated by Bostedt[6] that germanium nanoparticles synthesized using helium as the buffer gas exhibit less dependence on the pressure of the gas. This allows more flexibility in the pressure of the buffer gas, which is extremely useful because there are slight, but inevitable, variations in the pressure between experiments. Previous studies on Ge nanoparticles have illustrated that the larger Ar buffer gas, roughly 10 times the mass of He, affects the synthesis of Ge nanoparticles much more than He[6]. The buffer gas serves to cool the evaporated material with ballistic collisions leading to condensation of nanoparticles. However, if the buffer molecules are too large more collisions will occur after condensation which interferes with the particle trajectory toward the substrate. This could create some larger particles and decrease the amount of sample produced[2,6]. In the synthesis of smaller Si nanoparticles, the effects of using Ar as a buffer gas become even more acute. Some tailing and broadening of the size distribution for the Ge nanoparticles was also observed when using He as the buffer gas, but the effects were not as great as for Ar[6]. Hence, helium was used in the majority of the experiments described in this thesis to minimize these effects.

The pressure of the buffer gas has been varied by previous experimenters to change the size of the nanoparticles. Variation of the buffer gas pressure was performed to determine the relationship of the buffer gas pressure to the size of the particles. Contrary to previous syntheses of Si nanoparticles in Ar buffer gas[4,5], very little pressure dependence on particle size was seen in the current studies. These results are consistent with the results discussed above for Ge nanoparticles synthesized in He, where only a small variation in size was sent with pressure variation[6].

The final method of size control when using the gas evaporation synthesis is to use current variation to vary the temperature of the crucible. Increasing the input filament current increases the temperature of the crucible in the evaporator. This experiment uses a tungsten filament which becomes brittle after heating to high temperatures and exposure to air. As a result, subsequent heating often causes the filament to break. Although each filament has different characteristics, the experimental results are stable and reproducible for a single filament. The relative conditions for each filament also create reproducible results. Although each filament requires a different current to induce melting of the Si, samples that were made from two different filaments at a current 1 amp above the melting current produced particles that were similar in size. In order to reproduce the synthesis with different filaments, the melting current of each filament was noted and particle size was correlated to the difference between the current applied and the melting current used.

In order to get an accurate statistical measurement of the nanoparticle sizes, over 100 particles were measured with AFM for each sample. The size distribution curves from various currents of a single filament are shown in figure 4.4.

A detailed study of current vs. particle size was performed for Si nanoparticle synthesis in both He and Ar. A graph showing the particle size vs. deposition current for particles grown in He is displayed in figure 4.5 and a set of data for particles grown in Ar is shown in figure 4.6. The size of the nanoparticles has a roughly linear relationship with the evaporation current for each buffer gas.
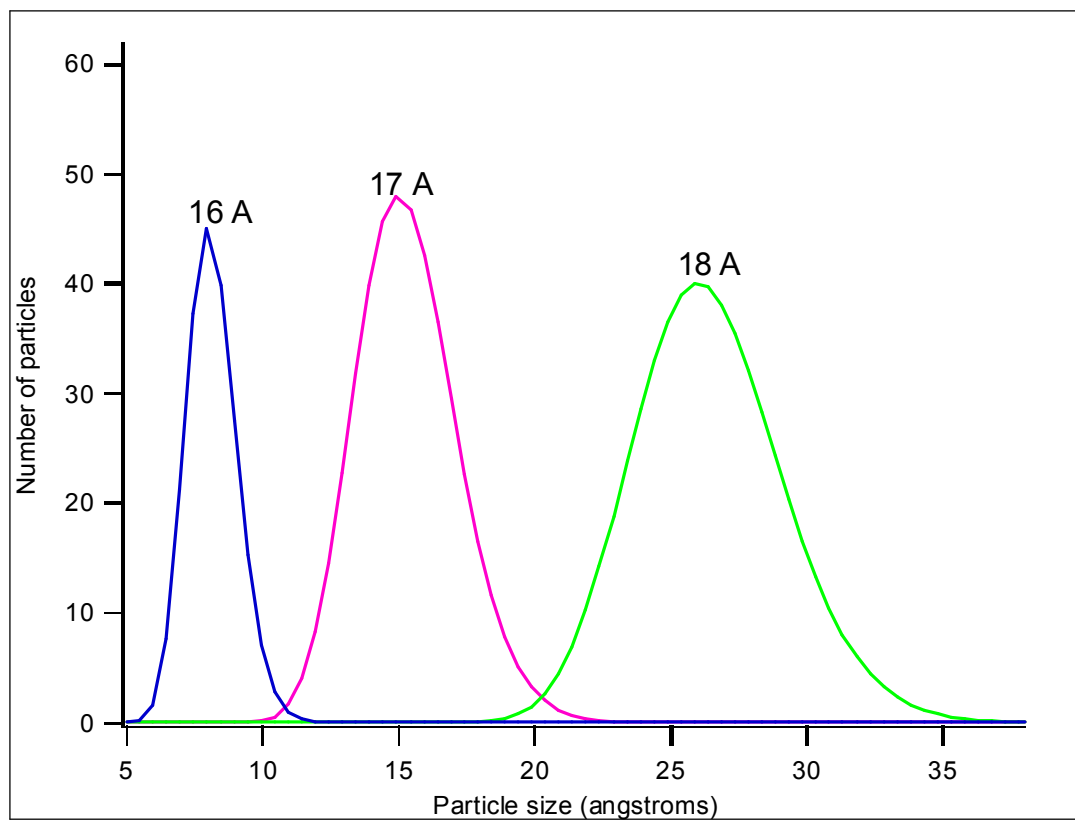
Fig. 4.4: Size distribution curves for the synthesis of Si nanoparticles at various currents in He buffer. The synthesis currents are marked above each curve.
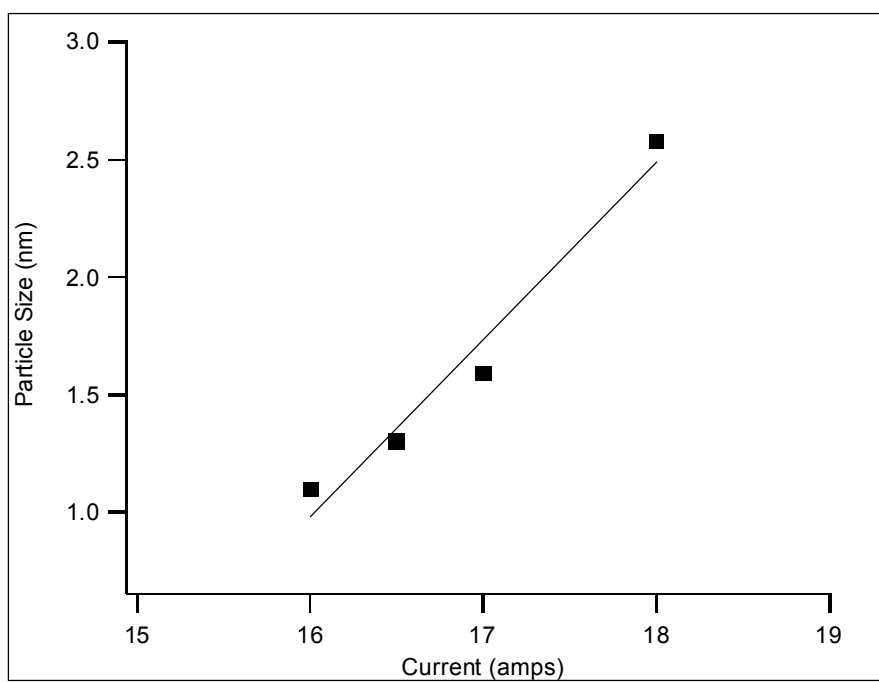
Fig. 4.5: Nanoparticle size as a function of deposition current for particles made using and helium as the buffer gas. The relationship is reproducible and roughly linear.
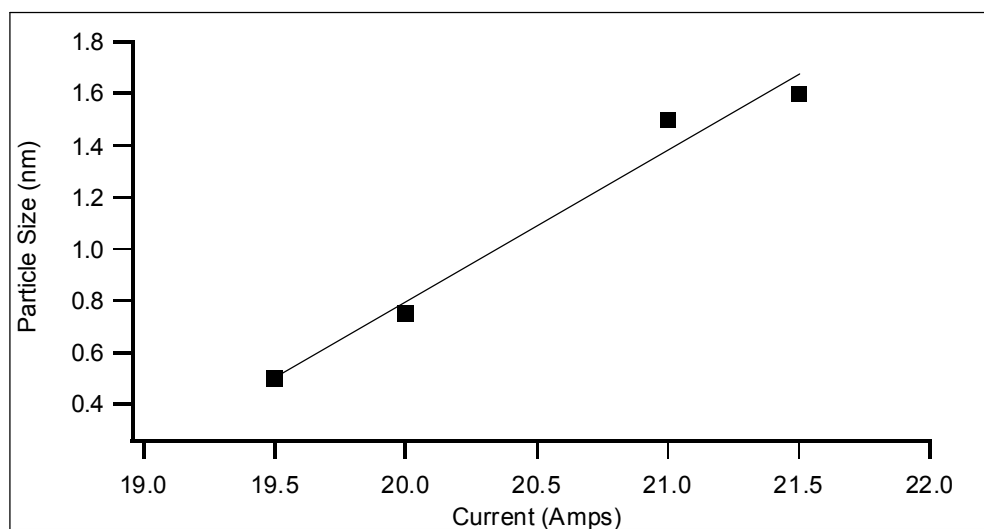
Fig. 4.6: Nanoparticle size as a function of current for particles synthesized in argon. As with the He synthesized particles, the relationship is reproducible and linear. The Ar synthesized particles also seem to have a similar slope to those made in He.

References

[1] O. Beeck, Smith, A.E., Wheeler, A., "Catalytic activity, crystal structure and adsorptive properties of evaporated metal films," Proceedings of the royal society A **177**, 62 (1940).

[2] C.G. Granqvist and R. A. Buhrman, "Ultrafine metal particles," Journal of applied physics **47** (5), 2200 (1976).

[3] S. Yatsuya, Kasukabe, S., Uyeda, R., "Formation of ultrafine metal particle by gas-evaporation techinque- aluminum in helium," Journal of crystal growth **24/25**, 319 (1974).

[4] L. N. Dinh, L. L. Chase, M. Balooch et al., "Optical properties of passivated Si nanocrystals and SiOx nanostructures," Physical Review B **54** (7), 5029-5037 (1996).

[5] T. van Buuren, Dinh, L.N., Chase, L.L., Siekhaus, W.J., Terminello, L.J., "Changes in the electronic properties of si nanocrystals as a function of particle size," Physical Review Letters **80** (17), 3805 (1998).

[6] C. Bostedt, University of Hamburg, 2002.

[7] W.F. Brunner, Batzer, T.H., *Practical Vacuum Techniques*. (Reinhold Publishing Corporation, 1965).

[8] C. Bostedt, van Buuren, T., Willey, T.M., Nelson, A.J., Franco, N., Moller, T., Terminello, L., "Characterization of Ge-nanocrystal films with photoelectron spectroscopy," Nuclear instruments and methods in physics research B **199**, 402 (2003).

[9] E.H. Lay, Kirakosian, A., Lin, J.-L., Petrovykh, D.Y., Crain, J.N., Himpsel, F.J., "Alignment of liquid crystals on stepped and passivated silicon templates prepared in ultrahigh vacuum," Langmuir **16**, 6731-6738 (2000).

[10] C. Bostedt, van Buuren, T., Willey, T.M., Terminello, L., "Controlling the electronic structure of nanocrystal assemblies by variation of the particle-particle interaction," Applied physics letters **85** (22), 5334 (2004).

Chapter 5:

Electronic Structure of Thermally Evaporated Silicon Nanoparticles

5.1 X-ray Absorption Spectroscopy (XAS) Measurements of Bulk Silicon for Comparison to Nanoparticles

We use XAS to probe the lowest energy empty states, or bottom of the conduction band, in the synthesized Si nanoparticles. For these experiments, the nanoparticle samples are deposited onto Ge substrates, such that it is possible to distinguish the sample from the substrate. XAS is sensitive to the quality of the prepared samples and can diagnose any problems associated with the synthesis by simply measuring the absorption edge since oxidation can also be easily detected.

As mentioned in the previous chapter, the $L_{2,3}$ x-ray absorption edge maps out the local densities of states of the bottom of the conduction band and is sensitive to changes in the electronic structure of the nanoparticles caused by quantum confinement. The nanoparticle XAS spectra are compared to a bulk Si spectrum as a means of calibration. The bulk silicon $L_{2,3}$ absorption edge spectrum shows the characteristic sharp absorption onset, corresponding to the L_3 edge, and the spin orbit splitting at 0.6 eV higher energy, corresponding to the L_2 edge ($2p_{1/2}$ degenerate state).[1] At higher energy, 105 eV, there is often a peak which corresponds to SiO_2. A silicon wafer is usually etched to remove the native oxide from the samples but, due to the high reactivity of Si, the wafer oxidizes rapidly and a small peak is seen in the spectrum. As discussed in chapter 3, XAS data can be collected via TEY. A representative bulk Si XAS spectra measured in TEY is shown in figure 5.1. The XAS measurements on these samples are generally measured using TEY where current from the secondary
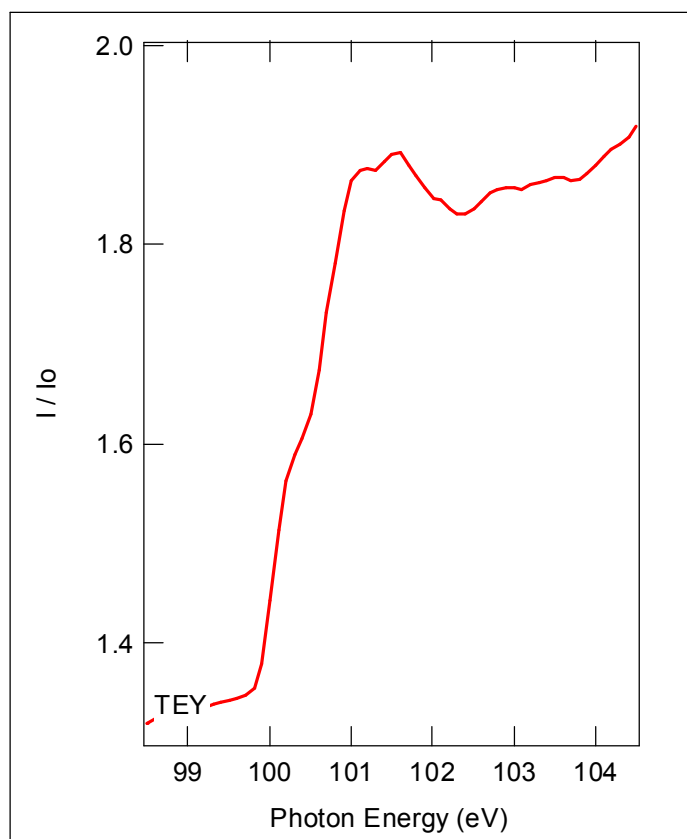
Fig. 5.1: Bulk Si XAS spectra in TEY collection mode.

electrons produced is measured and amplified using a Keithley current amplifier. Gains on the amplifier are generally 10^8 or 10^9.

One of the most important benefits of using XAS and SXF is that the conduction band can be measured independently from the valence band. Most bandgap measurements are performed using optical techniques that measure the total bandgap. These measurements cannot provide information on the electronic structure that can be obtained by deconvolution of the conduction and valence bands, such as the effects of quantum confinement on the individual band edges. XAS and SXF can be used to map the conduction and valence bands respectively of Si nanoparticles by probing the s-p densities of states.

5.2 XAS Measurements of Isolated Silicon Nanoparticles

Isolated nanoparticle samples were made using the inert gas evaporation synthesis discussed in the previous chapter. The synthesis chamber was back filled with He buffer gas to a pressure of 250 mTorr and the evaporator was heated slowly to the evaporation current. The crucible was then held at the deposition current to allow the temperature to stabilize the shutter was opened. The shutter was opened for less than one second to allow the nanoparticle sample to collect on the Ge substrate. Under these sample preparation conditions, we obtain very dilute nanoparticle films, less than a monolayer of nanoparticles deposited on the Ge surface. A representative AFM image of a sample under these preparation conditions is presented in figure 5.2.

It has been predicted that the bandgap of the nanoparticles will increase with decreasing size within a specific size region (the Bohr exciton radius). The Bohr exciton
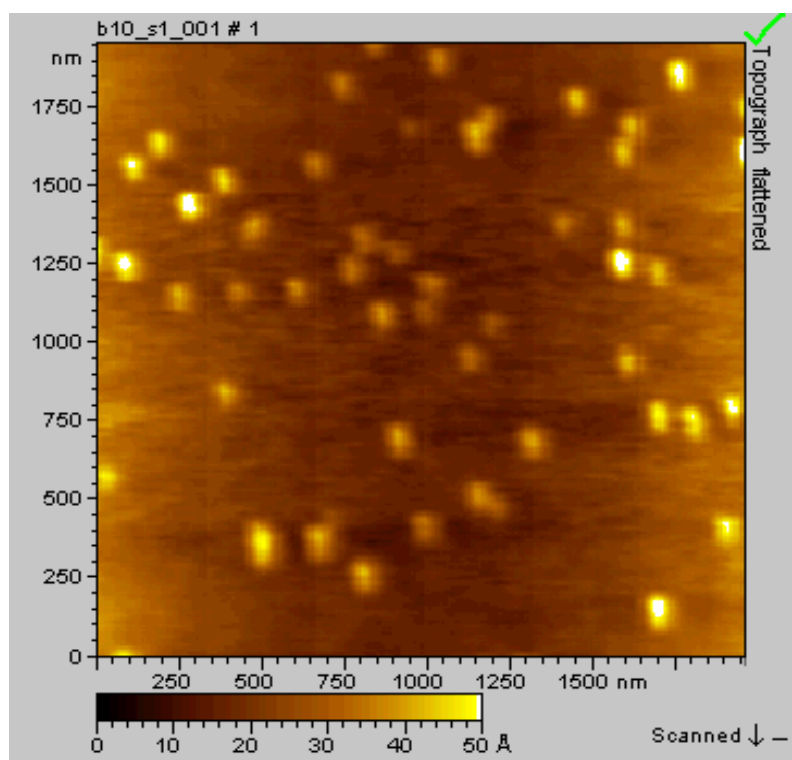
Fig. 5.2: AFM image of isolated Ge nanoparticles deposited on a flat silicon wafer[2].

radius for Si is 4.9 nm so this implies that nanoparticles of diameter less than 10 nm will exhibit quantum confinement effects[3]. We can experimentally observe quantum confinement effects be observing the shift in the edge features towards higher or lower energy with decreasing particle size when performing our XAS and SXF measurements, respectively.

Nanoparticle spectra are generally exhibit fewer and broader features than the corresponding bulk spectra. These nanoparticle spectra are compared to the bulk spectrum in figure 5.3. The nanoparticle samples are especially distinctive from the bulk spectrum due to the lack of spin-orbit splitting features. There are several theories for the absence of any spin-orbit splitting features in the nanoparticle spectra. A large size distribution has been reported to broaden the edge features in porous silicon, thereby obscuring the spin-orbit splitting[4]. More specifically, each particle size will have a slightly different edge position, resulting in a broadened conglomerate nanoparticle spectrum. explanation seemed plausible until spin-orbit splitting features were observed in nanoparticle samples with very large sample size dispersities[5,6] . An alternative explanation can be attributed to the presence of core excitons or electron-hole pairs. Although excitons have been observed as distinct features at the absorption threshold in CdS nanoparticles[7], sharp excitonic features are not observed in the Si $L_{2,3}$ edges. Since neither of these explanations seem to explain why we do not observe the spin-orbit splitting in our samples, another mechanism must be responsible for this effect. Therefore, we propose that surface disorder interferes with the spin-orbit splitting, which is responsible for washing out the edge features. Similar evidence of this has been observed in the valence band of similarly synthesized germanium particles where careful characterization of the surface structure and first principle calculations determined that surface disorder and reconstruction, but not a size effect, was the cause of the broadened features at the edge[8]. Although this does not definitively determine that this
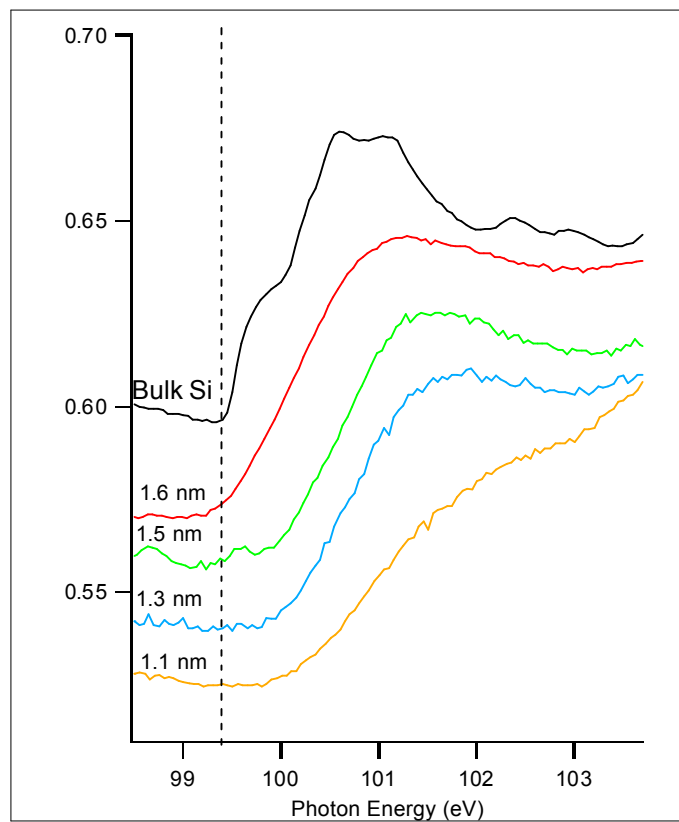
Fig. 5.3: Unpassivated, isolated samples show large shifts with respect to the bulk reference. The size of the particles are noted on the spectrum, decrease from top to bottom starting with bulk Si to 1.1 nm. All particles were synthesized at 250 mTorr He buffer gas pressure. The smallest sample is shifted 0.68 eV.

is the case in Si, these particles are similar enough to make the comparison and shows that disorder on the surface of evaporated nanoparticles can lead to broadening of the structure in x-ray spectra.

As shown in figure 5.3, the position of the Si absorption edge shifts toward higher energy as the particles decrease in size. The edge position of each nanoparticle spectra is determined through careful measurements of the absorption spectra the position of the absorption edge in the bulk spectrum is measured by finding the crossover point between a line extrapolated from the top of the edge feature above the L_2 edge and another line at the base line. The top of the edge feature above the L_2 edge is used instead of the top of the edge above the L_3 edge because the nanoparticle samples do not exhibit any spin-orbit splitting. This provides a self consistent means of measuring the absorption edge in the absence of spin-orbit splitting. The extrapolation technique is demonstrated for both the bulk and nanoparticle spectra in figure 5.4. Each edge is measured multiple times and an average position is determined. Upon analysis, the largest nanoparticle samples are not shifted to higher energy when compared to bulk but are actually shifted slightly to lower energy. As the size decreases, the edge shifts toward higher energy, with a maximum shift of 0.6 eV for the smallest sample in this work.

The sizes of the nanoparticles were determined by AFM and a plot showing the conduction band shift as a function of size can be seen in figure 5.5. From this plot, it can be seen that at smaller sizes the magnitude of the shift increases as the size of the particle decreases but makes a large drop at 1.6 nm and the absorption edge does not shift. Due to the nature of these experiments, the electronic structure of the nanoparticles seems to be effected by more than just the size of the particles but also the proximity to other particles. The amount of particles also increases with increasing particle size and at larger sizes no size dependent shift of the absorption edge is seen
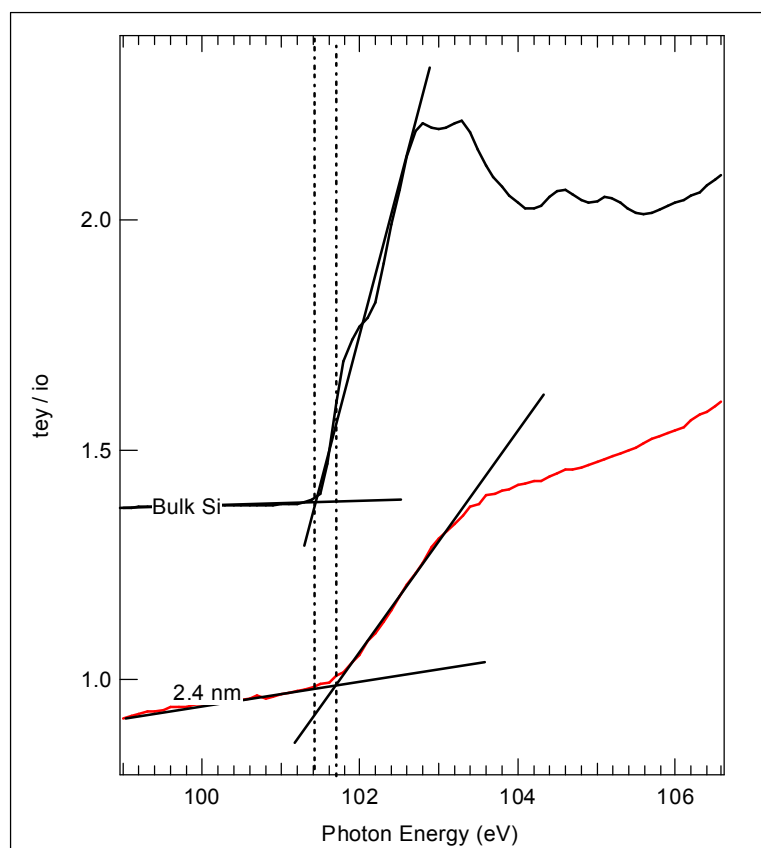
Fig. 5.4: Demonstration of determination of edge position. The pre-edge background is extrapolated to the edge until is crosses the extrapolated edge line.
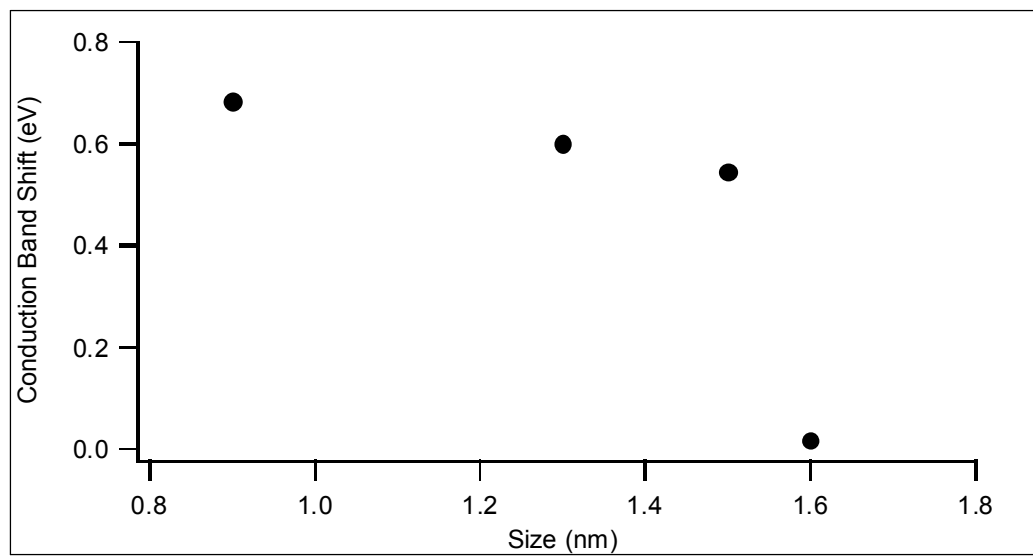
Fig. 5.5: Conduction band shift as a function of size for isolated particles.

although the sizes are well within the range of quantum confinement. It may also be that oxidation on the substrate surface passivated any dangling bonds on the nanoparticle surfaces which leads to an increase in the absorption edge shift. As the nanoparticle proximity decreased, the particles may have begun to touch. These effects are discussed in the next chapter.

5.3 XAS of Thick Films of Silicon nanoparticles

As described previously, the CB shifts for Si nanoparticles disappear at larger particle sizes. This observation cannot be attributed solely to quantum confinement effects, as the CB shift going from a 1.5 nm to 1.6 nm particle is 0.6 to 0 eV, respectively. Treating the quantum confinement effect as the only explanation for edge shifts may be acceptable in an ideal single particle system or for monodispersed particles, however, for real world applications (i.e. devices), the nanoparticles will need to be close together or touching (i.e. multilayers)[9].

Using the inert gas evaporation synthesis method, thicker films of nanoparticles can be produced by simply increasing the deposition time. An AFM image of a thick film of nanoparticles is shown in figure 5.6. Several experiments were conducted to determine the effect of the particle-particle interaction on the absorption spectra of the nanoparticles and can be seen in Figure 5.7. In this figure, the spectrum of an isolated nanoparticle sample produced as described above (i.e. less than one second shutter exposure) is shown compared to the spectrum of a sample synthesized under the same conditions but the shutter was left open for several seconds (producing a multilayer). These experimental conditions should produce samples of exactly the same size, with the only differences arising from the amount of sample that is collected on the substrate. Interestingly, the XAS data in figure 5.7 indicate that the isolated sample is shifted with
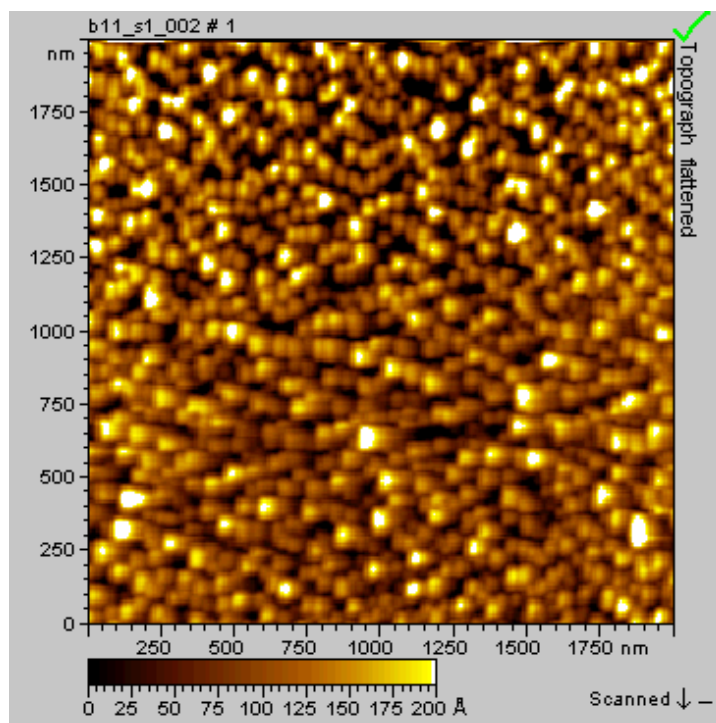
Fig. 5.6: AFM image showing a thick film of Ge nanoparticles deposited on a silicon wafer[2].
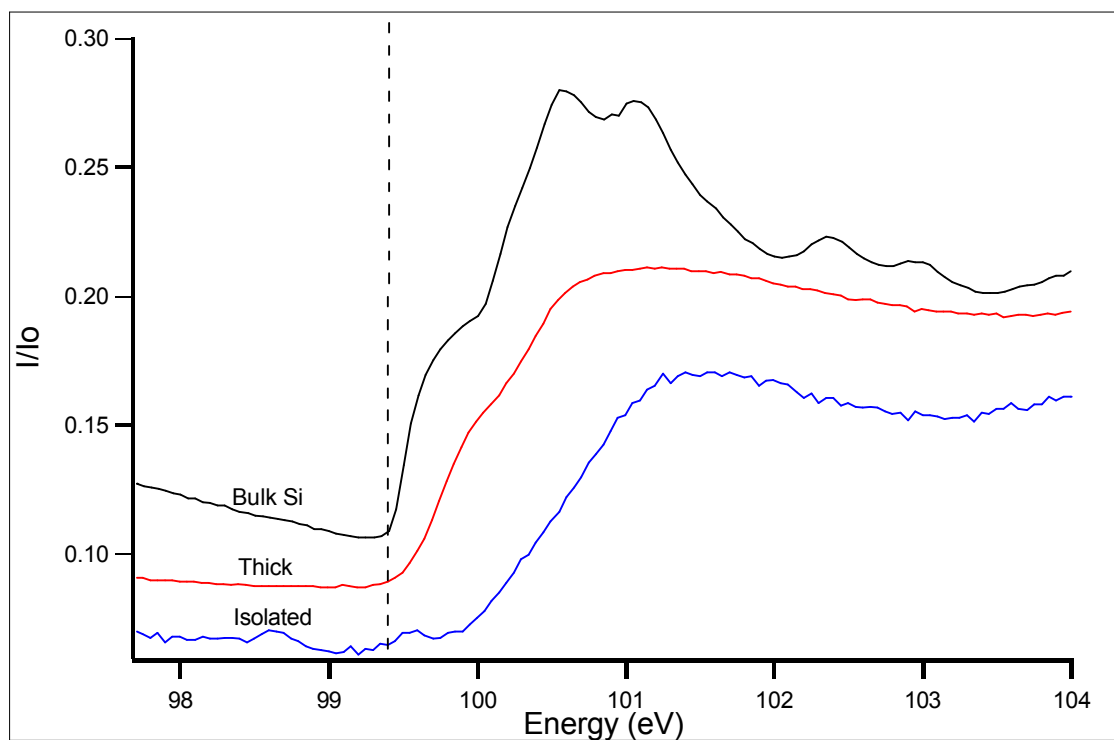
Fig. 5.7: Proximity effects are shown by the large difference in shift between a thick unpassivated and isolated unpassivated sample. Both samples were made in He buffer gas at a pressure of 250 mTorr and 17 A of current on the evaporator. The particles were determined to be 1.5 nm. The thick sample shows no shift compared to the bulk Si spectrum but the isolated particles show a large shift.

respect to the bulk spectrum while the multilayer sample shows no shift relative to bulk Si. These results suggest that the electronic structure of isolated and multilayer, or thick, samples is inherently different, although the particle sizes have not changed.

There are several possible reasons for this change in the absorption edge in the thick samples. First, by changing the preparation conditions, the sample sizes could have increased which would decrease the quantum confinement effect and reduce the edge shift relative to bulk. However, studies, both from this research and previous research on Ge nanoparticles[2], showed that both the isolated and thick samples produced the same sized particles when produced under the same synthesis conditions. Since the background of the thick films of nanoparticles is difficult to measure the size against, a portion of the substrate was masked during sample deposition and the particles were measured at the interface of the masked region and the exposed region where there were some individual particles. As both synthetic strategies produced the same sized particles, an alternative possibility is needed to account to the reducing in edge shift sin the thick samples. Particle agglomeration could account for the observed edge shifts as agglomeration will effectively produce a larger particle which will in turn decrease the quantum confinement effects[10]. AFM studies on Ge nanoparticles have indicated that particle agglomeration does occur in the thick samples[2] and is responsible for the lack of edge shift in the Ge L_e edge spectra[10]. Even in the absence of particle agglomeration, a decrease in edge shifts can occurs due to the particles "touching", or being in close proximity to one another. Bostedt et al. calculated that two 1.6 nm nanoparticles in close proximity would effectively become a 2.0 nm and have the corresponding edge shift[10]. When individual unpassivated nanoparticles come into close contact, their electronic properties can no longer be explained in terms of a single particle. Electron delocalization (i.e. wavefunction overlap) can occur between two particles, and this interaction can cause the reduction of observed quantum confinement

effects. There are two ways to solve either the agglomeration or correlation problems: one could (1) prepare a sample of only monodispersed isolated particles or (2) use a method of physically separating the nanoparticles, such as a molecule placed on the surface. A molecule attached to the surface of a nanoparticle is often called a passivant because in direct gap nanoparticles passivation is used to increase the luminescence by eliminating non-radiative energy release.

Surface passivation seems to be an obvious choice as it not only solves the problem off the particle-particle interaction, but also tackles another problem which is observed on nanoparticle surfaces: dangling bonds. Passivation of nanoparticle surfaces has been used extensively in II-VI nanoparticles to remedy dangling bonds on the nanoparticle surface and decrease the non-radiative deactivation processes which hamper the band edge photoluminescence[11] and it is thought to have the same effect in silicon[12]. Proper passivation of the nanoparticle can fulfill dangling bonds on the surface of the nanoparticle and can help to restrict the avenue of electron/hole energy release to be limited to band edge recombination[13,14]. This is observed in the absorption edge by a red shift of the edge position with respect to the position of the bulk spectrum.

5.4 Effects of Passivation on Absorption Edge Shifts

In this work alcohol groups were adsorbed onto the nanoparticles with the goal of passivating their surfaces and preserving the quantum confinement effects. In the present study, both methanol and ethanol were used to passivate the particles. Previous studies by Lay et. al. have shown that these molecules attach via chemisorption effectively to a clean bulk silicon surface[15,16].

5.4.1 Methanol Passivation

The synthesis of alcohol passivated Si nanoparticles is the same as described in the isolated nanoparticle synthesis except that the alcohol was attached to the surface of the nanoparticles through the use of a liquid cell. After the buffer gas was evacuated from the chamber, the alcohol vapor from the liquid cell was introduced into the cluster chamber via a leak value to achieve a pressure of 1×10^{-6} Torr. The nanoparticles were exposed to this environment for 1 minute for the purposes of passivation with methanol. Then the chamber was evacuated so the alcohol would not interfere with the synthesis of the next layer of particles. The passivation was conducted after each deposition of silicon nanoparticles in order to allow the alcohol to attach to each layer of particles. This was performed for five deposition layers to produce a thick sample. Representative absorption edges of isolated, methanol and ethanol passivated particles are shown in figure 5.8 and the results of all the samples measured in each of these passivation experiments are shown in figure 5.9. Although methanol is a small molecule, the results show that by putting methanol on the surface of the particles some amount of passivation is achieved. An increase in edge shift as size decreases is seen in the results of this study.

The XAS spectra of the methanol passivated particles showed increasing edge position shift with decreasing size analogous to the trends with the isolated samples but the shifts for the methanol samples were not quite to the same magnitude as the isolated samples. The fact that surface passivation can retain shifts in the CB edge but not to the sample degree as the isolated system implies that both passivation and proximity effects exist in the methanol passivated nanoparticles (Figure 5.10). In figure 5.10, three possible conditions of the nanoparticles are illustrated, including isolated, touching and passivated with methanol nanoparticles. In the case of the isolated nanoparticles,
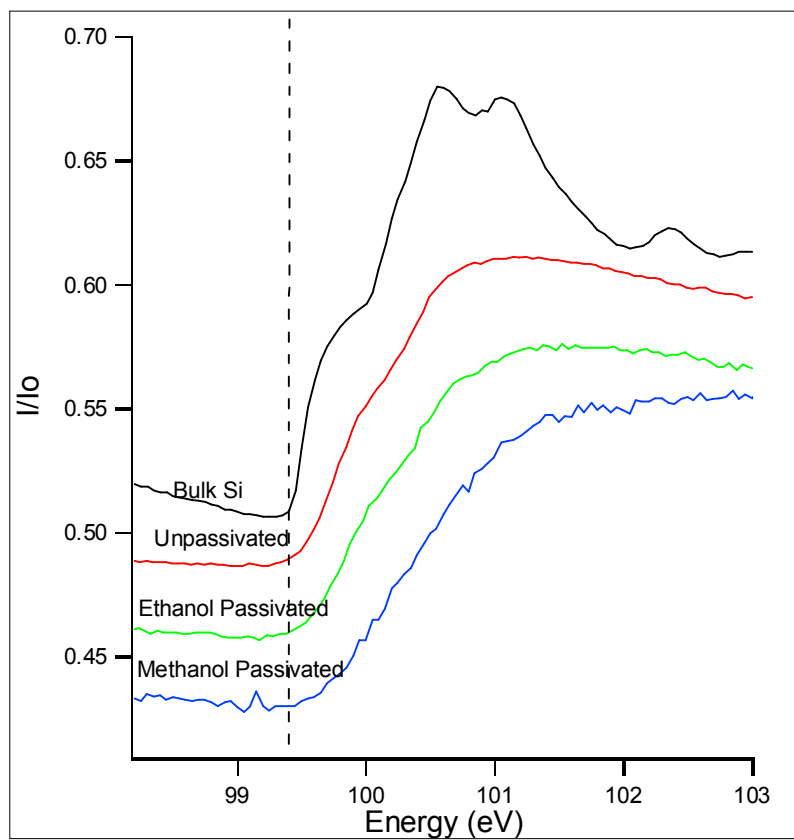
Fig. 5.8: XAS spectra demonstrating the effect of passivation on the Si $L_{2,3}$ edge of unpassivated, methanol, and ethanol passivated Si particles as compared to bulk Si.
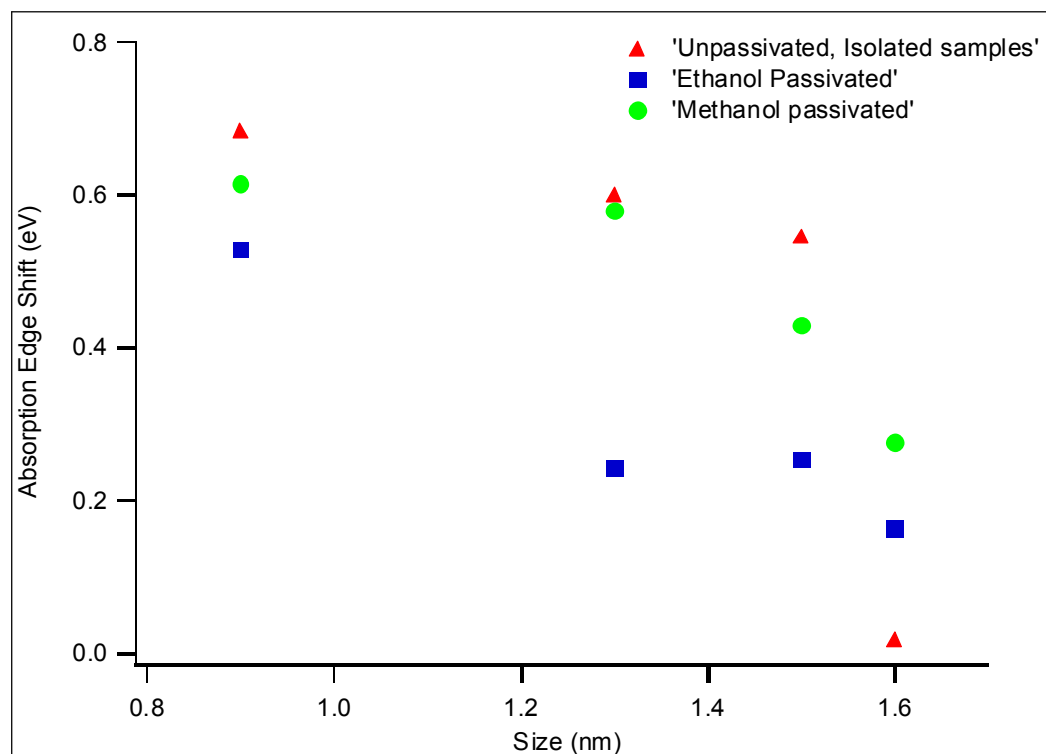
Fig. 5.9: Comparison of the different surfaces environments in three thick samples. Unpassivated and ethanol passivated samples did not exhibit quantum confinement induced edge shifts when compared to bulk Si. Methanol did show that passivation preserved these effects.
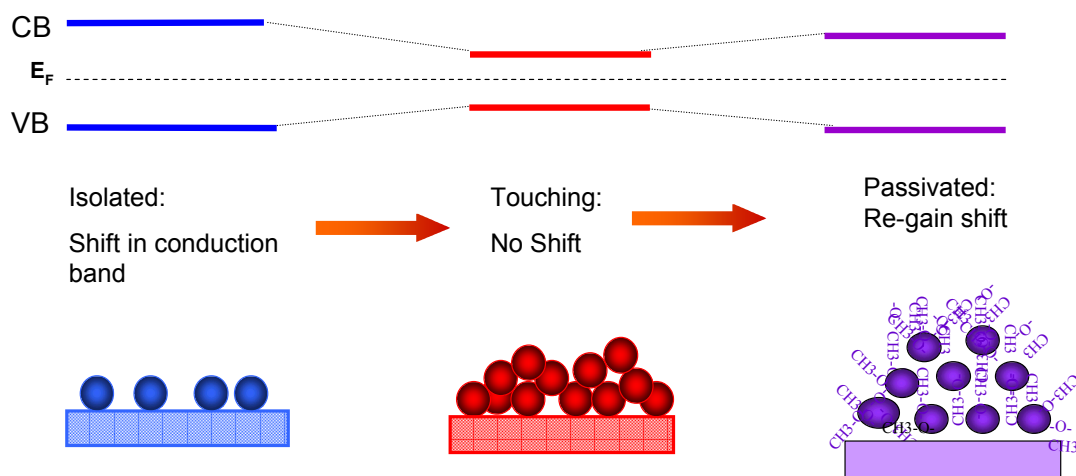
Fig. 5.10: Illustration of the effects of proximity and methanol passivation on the band gap of silicon nanoparticles.

confinement widens the bandgap of the nanoparticles as evidenced from the XAS data. The electronic structure of the thick samples are affected by correlation and aggregation as discussed in the previous section and results in a bandgap narrowing. When the methanol is put on the surface of the nanoparticles, many of the problems in the unpassivated thick samples are alleviated leading to a widening bandgap as observed in the isolated nanoparticles.

As already stated, it should be noted that the methanol passivated samples did not completely regain the shifts observed in the unpassivated, isolated samples. While the smallest isolated sample showed a shift of 0.7 eV, the smallest passivated sample only showed a shift of 0.5 eV. While this does indicate some passivation of the nanoparticles, this result implies that the particles are not completely passivated. The possibility of incomplete passivation in the nanoparticle surface led us to attempt passivation with longer chain alcohol molecules.

5.4.2 Ethanol Passivation

Although methanol appeared to isolate the particles from each other, there was still some difference between the confinement edge shifts seen in the isolated particles and the passivated particles. A logical explanation for this behavior is that this is due to the small size of methanol still allows some correlation between the nanoparticles. Therefore, a larger molecule, ethanol, was used to passivate the nanoparticle surfaces in an attempt to increase the separation between them. Figure 5.9 provides a graphical comparison of the three surface structures, unpassivated, ethanol and methanol passivated. The surprising result from these experiments was that passivation with ethanol, figure 5.8, did not increase the shift in the energy of the absorption edge compared to the shift obtained for methanol passivated particles. In addition, very thick

ethanol passivated nanoparticle samples did not show any shift at all while similarly prepared samples passivated with methanol did show absorption edge shifts.

Although the reason for the lack of increased passivation using ethanol was not unambiguously identified, it is thought that the ethanol may have actually been too large to fit between the nanoparticles or possibly that steric effects may have limited the amount of ethanol that would attach to surface. Another possibility is that the ethanol did not attach to the surface of the particles as effectively as methanol, which would then result in less effective surface passivation. Irrespective of the underlying reasons for the absence of any shift for the ethanol passivated samples, methanol was used for the remaining passivation experiments.

5.5 SXF of Bulk Silicon

The mapping of the valence band states is accomplished through soft x-ray fluorescence (SXF) also called soft x-ray emission (SXE). As described in the previous chapter, incident x-rays excite the core electrons into the empty states and an x-ray photon is emitted due to a valence electron recombining with the core hole left by the absorption process. In this technique the incident x-ray energy is fixed and the energies of the emitted photons are energy resolved with a grating spectrometer.

The bulk crystalline silicon SXF spectrum is characterized by the three broad peaks evident in figure 5.11. These peaks occur at 89 (A), 91.5 (B) and 96 eV (C) when the sample is excited at 102 eV well above the edge onset. These peaks are associated with $3s$ states, strong s-p hybridization and p states, respectively[17]. This spectrum contains contributions from transitions to both the $2p_{1/2}$ and $2p_{3/2}$ degenerate states which are separated by 0.6 eV due to spin-orbit splitting. As the sample is excited with lower energies, noticeable changes in the SXF spectrum are observed including
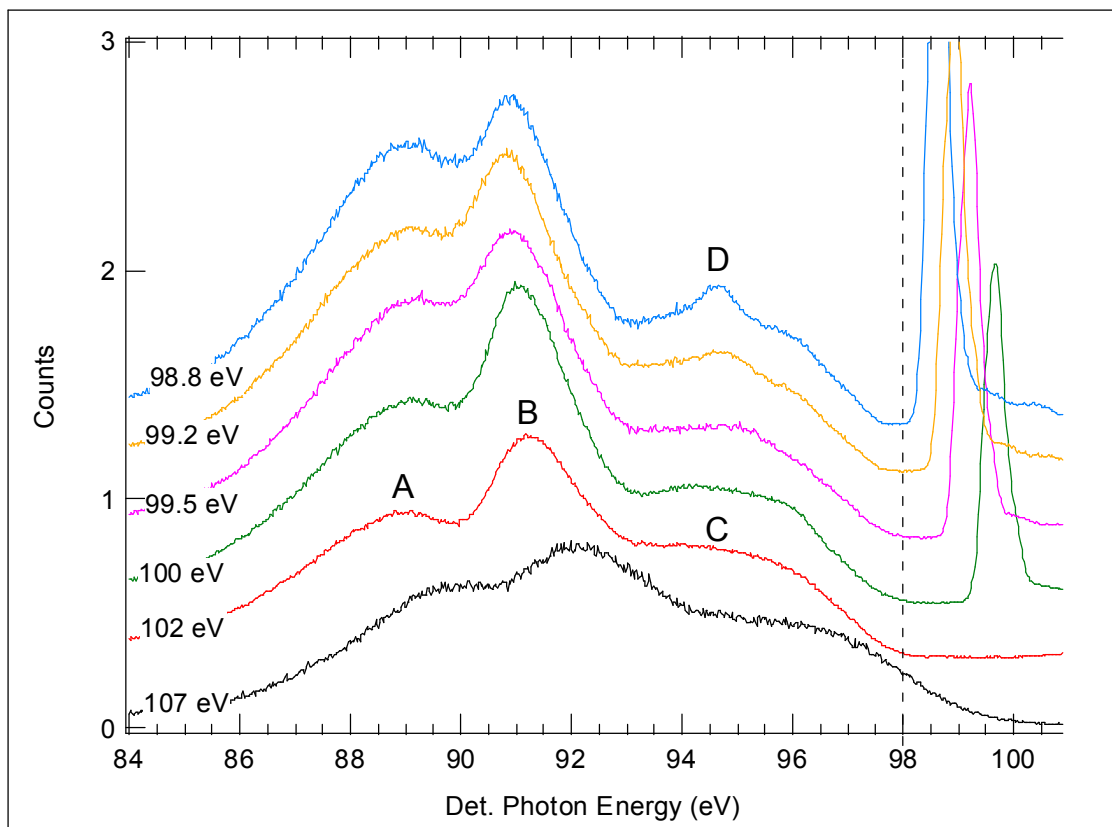
Fig. 5.11: Silicon SXF spectra excited at increasing energy from top to bottom. When excited below the L$_2$ edge the edge position shifts toward lower energy and the RIXS peak is observed (D). The crystalline Si has three characteristic peaks, marked A, B and C, which broaden when the oxide peaks are excited at higher energy as in the spectrum excited at 110 eV.

broadening of the two low energy peaks. Resonant inelastic x-ray scattering (RIXS) effects at excitation energies below the $2p_{3/2}$ threshold. At low excitation energy (E_{ex}=98.8 eV), an observable sharpening of the edge arises due to deactivation of the $2p_{1/2}$ state and produces a shift of the edge by ~0.6 eV. In addition, at these lower photon energies, a new feature arises in the SXF spectrum (D) which is a RIXS effect. Due to the large dispersion in the SXF spectra with photon energy, all experiments have to be excited at photon energies high enough to include all spin orbit splitting components of the edge but not too high in energy to include emission from the oxide features. To this end, all the SXF spectra for the nanoparticle samples (and bulk Si standard) were all taken at the same excitation energy (100 eV) to obtain an accurate and self-consistent comparison of the VB DOS. The high energy edge position is measured to determine the upper limit of the valence states and is marked on the spectra by a dashed line.

5.6 Quantum Confinement Effects on the Emission Edge

The probability of fluorescence emission is much less likely than Auger decay for Si, as discussed in chapter three and illustrated by figure 3.13. As a consequence, more sample is needed to perform SXF measurements than absorption measurements, which prevented measurement of the valence band for the isolated nanoparticle samples. However, thick samples of nanoparticles do not exhibit quantum confinement edge shifts and, as such, careful passivation of the nanoparticles was needed to enable measurement of the valence band edge shifts of these particles. The samples were made in layers, first a layer of nanoparticles was deposited onto the substrate and then passivated with methanol. This was repeated until the sample was thick enough to perform SXF measurements. Because of this, the valence band data from these

samples will be compared to the absorption data from the same thicker, passivated samples in the total bandgap determination and not the isolated samples.

Representative SXF spectra of silicon nanoparticles are shown in figure 5.12 and are compared with bulk Si as a reference. Most observable are a small smearing of the DOS features in the nanoparticle samples and shifting of the VB edges to lower energy with decreasing particle size consistent with quantum confinement. The smallest sized nanoparticles showed a shift of over 0.6 eV. This data is plotted in figure 5.13a and the valence band to conduction band shift ratio is shown in figure 5.13b.

5.7 Total Bandgap Determination

From the SXF and XAS data the total bandgap can be determined. Since the conduction and valence band edge shifts have been experimentally measured in the Si nanoparticle samples, the bandgap can then be determined by the relationship,

$$E_{gap}(NP) = \Delta CB + \Delta VB + E_{gap}(bulk) \qquad\qquad 4.1$$

where $E_{gap}(NP)$ is the bandgap energy for the nanoparticle, ΔCB and ΔVB are the conduction band and valence band shifts, respectively due to quantum confinement, and $E_{gap}(bulk)$ is the bulk Si bandgap (1.1 eV at 300 K)[18]. Figure 5.13a shows the size vs. shift for both the conduction and valence bands. The ratio of the shifts of the valence and conduction bands can be seen in figure 5.13b. The relationship between these two is roughly linear with a ratio of 2:1. In previous studies of silicon nanoparticles, the valence band shifts to conduction band shift ratio was 2:1 [19] and the band gap was taken
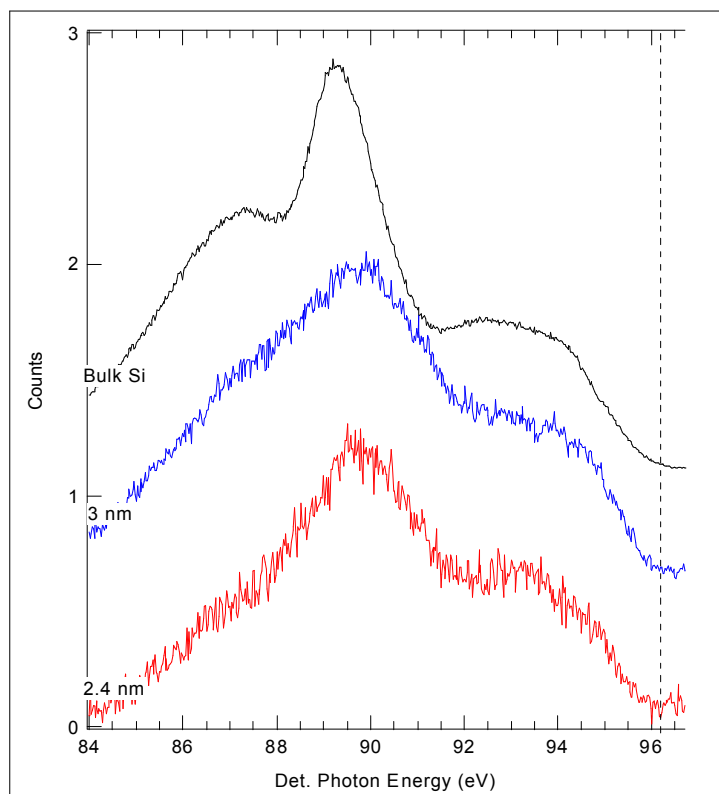
Fig. 5.12: Valence band (SXF) measurements of silicon nanoparticle samples. Bulk silicon SXF is shown in the top spectrum decreasing in size to 2.4 nm.
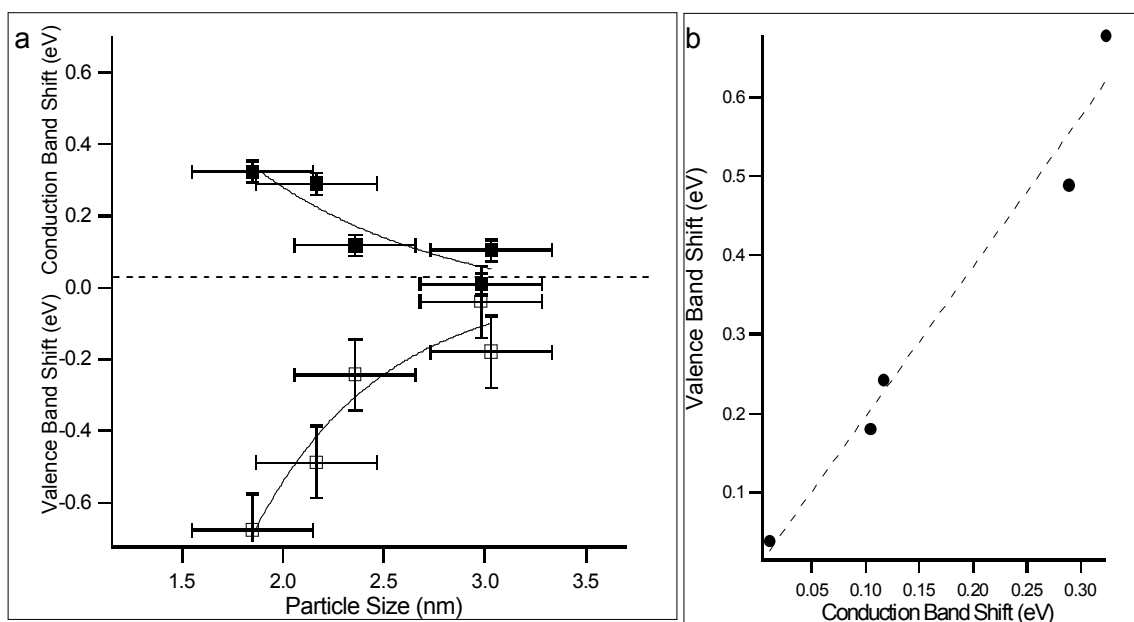
Fig. 5.13: **a)** Size vs. shift, for both conduction band and valence band and **b)** valence band vs. conduction band shift the ratio between VB:CB is ~2:1.

as

$$E_{gap}(NP) = 3\Delta CB + 1.1eV \qquad\qquad 4.2$$

Figure 5.14 shows the Si nanoparticle size vs. bandgap and it is observed that the band gap increases with decreasing size. This is in agreement to both previous experimental results and also computationally determined bandgap measurements[19,20].

Several theoretical models, discussed in chapter 2, have attempted to predict the confinement effects of the bandgap on silicon nanoparticles. The models that give bandgaps closest to those experimentally measured to date, are the psuedopotential plane wave method determined by Reboredo et. al.[20] and density functional theory by Puzder et. al.[21,22].

The calculated bandgaps from Reboredo et. al.[20] predict much larger band gap widening with particle size than observed in the work presented in this thesis and a comparison of these values is given in figure 5.15. Overestimation of the band gaps by many different theories has been a common problem in the literature[19]. Several reasons may account for the differences between the experimental and theoretical bandgaps. First, these theoretical shortcomings may arise from surface and proximity effects and have been proposed to be due to the differences in surface passivation[19]. Surface passivation of the Si nanoparticles with methanol was originally intended to suppress proximity effects on the band edge shifts, however, as discussed earlier, these effects were not completely suppressed. Second, the differences between the experimental and theoretical bandgaps may also be due to differences between the actual measurements and the assumptions made in the calculations. The calculations assume single nanoparticles with no particle-particle interaction, while this situation is much more difficult to achieve experimentally. Although every effort was made to produce

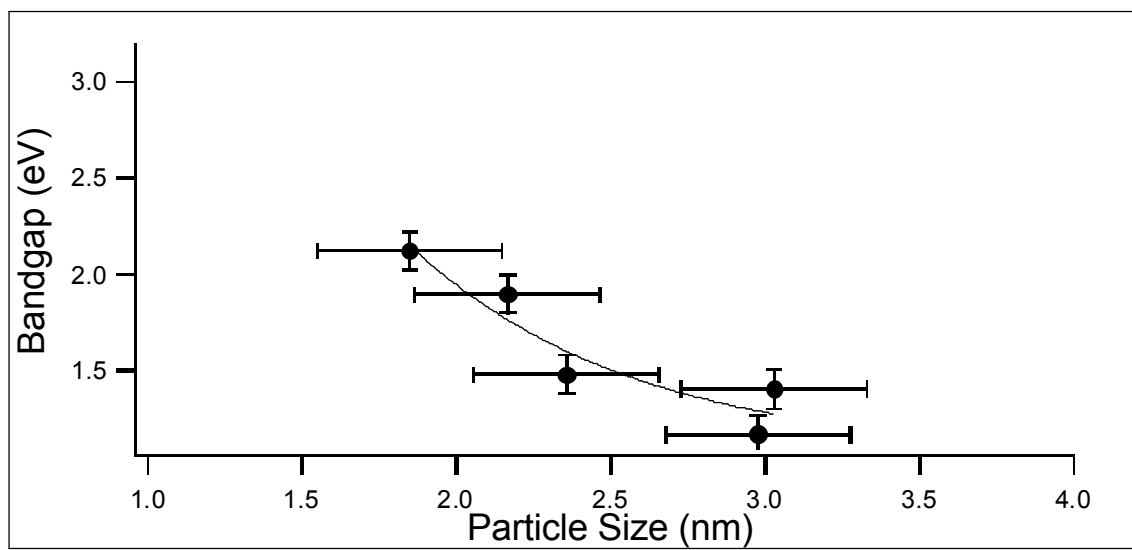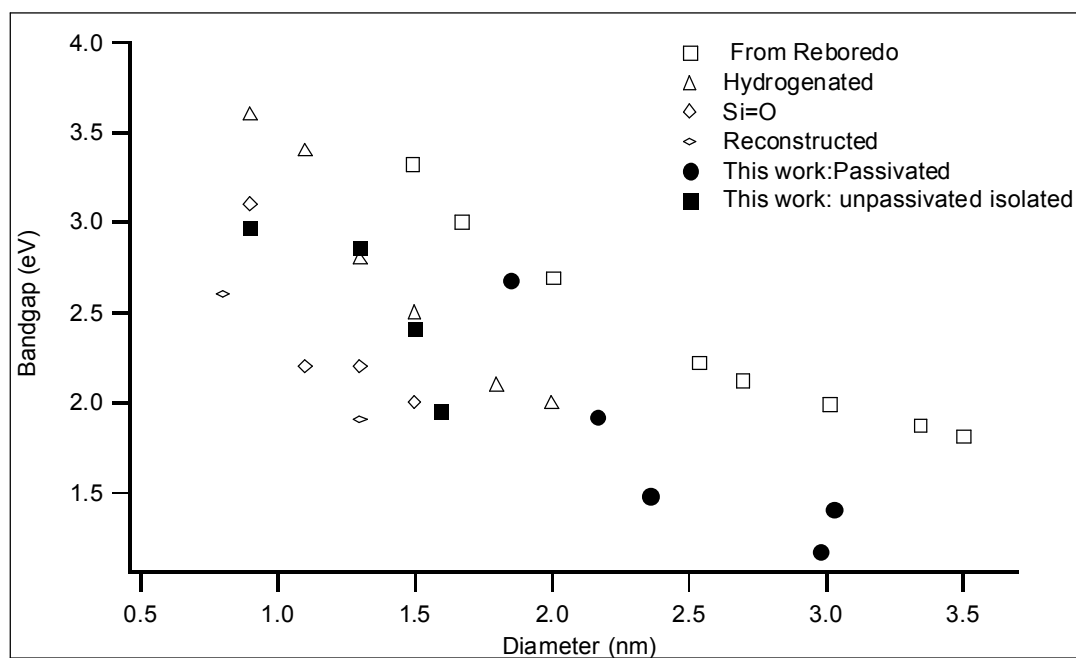**Fig. 5.14**: Size vs. Bandgap for methanol passivated nanoparticles.

Fig. 5.15: Experimental bandgaps from the present data compared to calculated bandgaps from Reboredo et al.[20] and Puzder et. al. (hydrogenated, Si=O and reconstructed)[21,22] Reboredo calculated bandgaps predict much larger than those experimentally measured here. Puzder et. al. had much closer predictions to our experimental results.

monodispersed nanoparticles, it is conceivable that even when preparing the isolated particles (i.e. Less than a monolayer of particles) some particles may be touching. The introduction of particle-particle interactions could lead to wave function leakage leading to smaller bandgaps in the experimental data. Third, the equation used to determine bandgap in this work, equation 5.1, does not take into account the binding energy of the exciton [20].

A more plausible explanation for the discrepancy between experiment and theory lies in the modeling of the nanoparticle surface. In another publication by Reboredo[23], it is shown that surface termination may actually play an even larger role than confinement on the band edge shifts. It was predicted that methyl passivated surfaces will have narrower gaps compared to hydrogen passivated particles. Although the valence band edges of the isolated particles was not measured, assuming the same ratio of the band shifts seen in the passivated particles these particles can be compared to the theoretical predictions as well, figure 5.15. These samples are closer to the theoretical predictions but still do not match completely.

The calculations of Puzder et. al.[21,22] take into account more detail in the surfaces of the Si nanoparticles. Three different surface terminations were investigated, hydrogenated, oxide passivated and reconstructed. These calculations, plotted in figure 5.15, exhibit a much closer agreement with our experimental data. Although similar exist in these calculations as the calculations by Reboredo, it seems that proper modeling of the nanoparticle surface allows theory to approach bandgap values close to our experimental values. The passivated samples produced here are quite close to the theoretically obtained values for hydrogenated surfaces. The isolated particles show a smaller bandgap and are closer to the reconstructed and Si=O surfaces. This seems reasonable since the isolated particles may have some oxygen from the substrate present on the surface or have reconstructed the dangling bonds to minimize energy.

5.7 Doped Silicon nanoparticles

A recent trend in silicon nanoscience research is the study of doped nanoparticle with an emphasis on understanding how the guest dopant can affect the electronic structure of the host nanoparticle. One of the most important properties studied are the photoluminescence properties. Researchers have been interested in understanding the mechanism of light emission in Si nanoparticles and finding a way to control both the frequency and line width of the PL. An obvious choice for a chemical dopant in silicon is erbium, as erbium has been used in many light emitting devices due to its of its bright PL at 1535 nm, the same wavelength of current silica optical fiber technology[24,25]. The bright emission at 1535 nm from Er^{3+} states is due to an intra band (internal) $4f$ transition ($^4I_{13/2} \rightarrow \, ^4I_{15/2}$). This corresponds to the region of low loss for silica optical fibers. Silicon based optical sources would integrate easily into these systems and the demand for sources compatible with fiber systems is in high demand.

The use of a silicon nanoparticle as a sensitizer, or antenna, for erbium PL has been previously studied[24]. Physically, the nanoparticle is excited by a photon and produces an electron-hole pair. This electron-hole pair non-radiatively transfers its energy to the Er center via a dipole-dipole interaction (Förster energy transfer). A non-radiative decay to the $^4I_{13/2}$ state is followed by a radiative decay to the $^4I_{15/2}$ state which is the characteristic 1535 nm emission[25]. This emission could be used in many applications including waveguide amplifiers[25]. Figure 5.16 shows a schematic of nanocrystal stimulated emission of Er^{3+}. When the nanoparticle is excited the emission couples to the Er ions via dipole-dipole transfer. A non-radiative decay to the $^4I_{13/2}$ state is followed by a radiative decay to the $^4I_{15/2}$ state which is the characteristic 1535 nm emission[25].

In these experiments, the evaporation parameters were similar to those of the isolated nanoparticle synthesis; however a second evaporator was added which
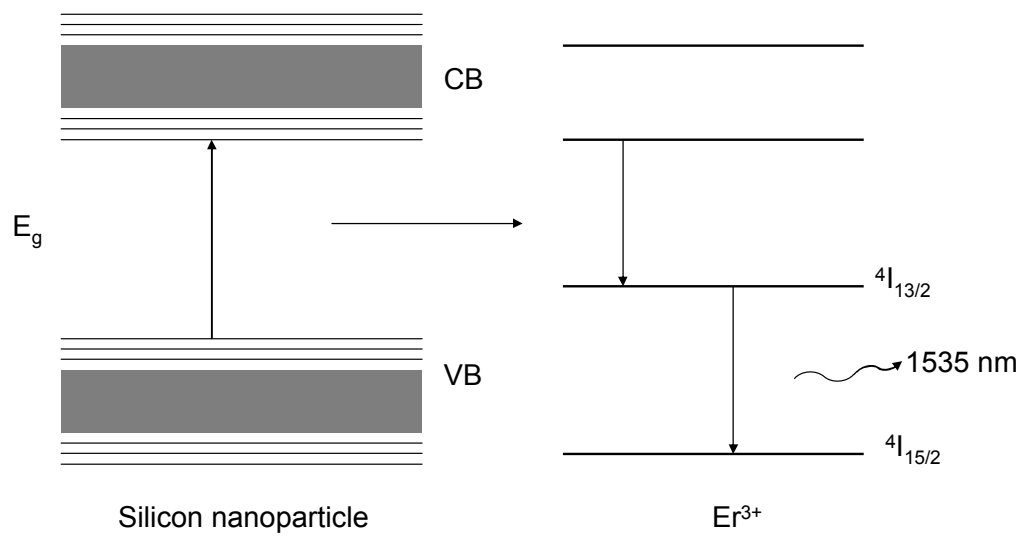
Fig. 5.16: Schematic of excitation of the intra 4*f* transition ($^4I_{13/2} \rightarrow \, ^4I_{15/2}$) of Er^{3+} stimulated by silicon nanocrystal emission. Reproduced from Kenyon[25].
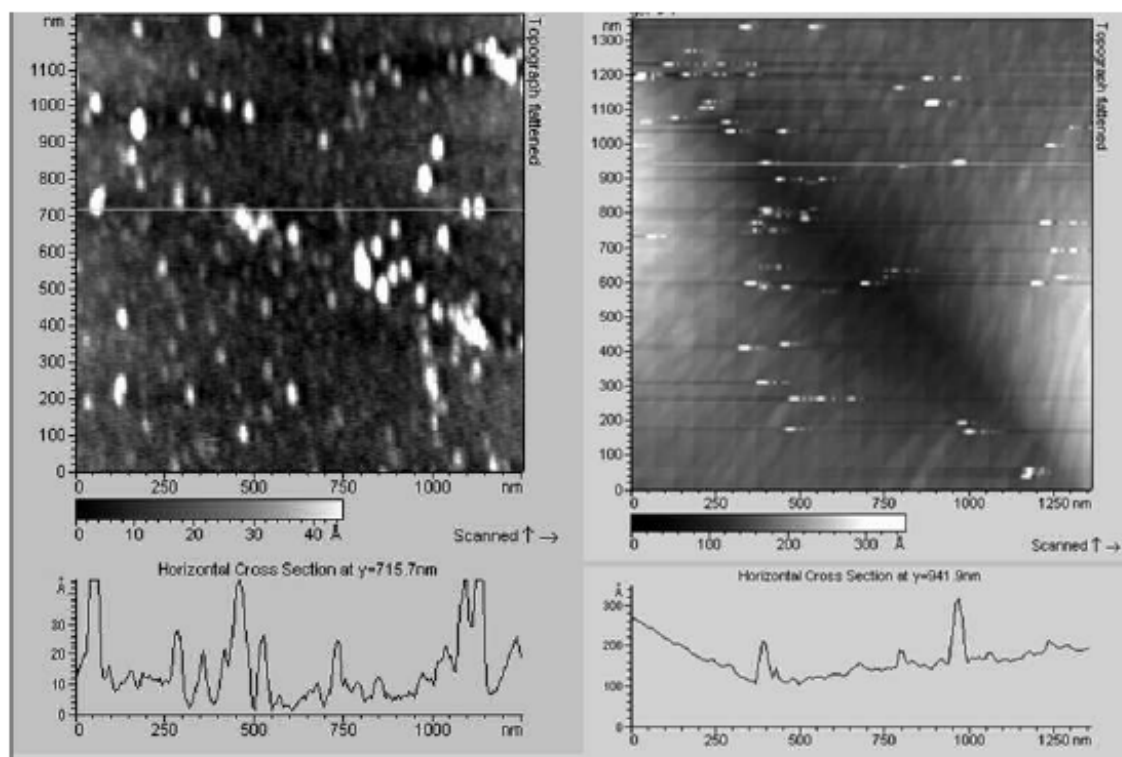
Fig. 5.17: AFM images showing a) nanoparticles are still formed when small amounts of Er are added to the nanoparticles but b) larger structures form when too much Er is added.

contained erbium. The erbium was co-evaporated with the silicon to incorporate erbium into the silicon nanoparticles. AFM images of Er doped Ge nanoparticles have confirmed that nanoparticles do form in this synthesis, although AFM cannot prove the Er is incorporated into the particle[26]. In Ref. 26, Er M_5 edge XAS was used to probe the chemical state of Er in the Ge nanoparticle for confirmation that the Er dopant resided in the Si nanoparticle. Both Er metal (oxidation state: 0) and Er_2O_3 (oxidation state: 3+) were used as standards and the Er M_5 edge spectra of these samples were compared to the Er M_5 edge spectra of the Ge/Er nanoparticle. A close agreement in the peak positions between the nanoparticle and Er_2O_3 spectra was observed allowing the identification of the oxidation state of the Er in the nanoparticle to be 3+. This result is significant as it provides direct evidence that the chemical state of the Er changes from evaporation to incorporation in the nanoparticle. Similar measurements can be used to prove the chemical state of Er in Si nanoparticles.

Er M_5 edge spectra for both Er_2O_3 and a Er/Si nanoparticle are presented in figure 5.18. The nanoparticle erbium edges were slightly shifted from the Er_2O_3 peak position, but not at the same energy as Er metal. This could mean that a slightly different form of erbium was present in the Er/Si nanoparticles then was observed in Er/Ge nanoparticles. Nonetheless, there is direct proof that the oxidation state of the Er in the Si nanoparticle has changed from evaporation indicating that the Er dopant is incorporated in the Si nanoparticle.

In addition to the Er M_5 edge, the Si $L_{3,2}$ absorption edge was monitored with increasing erbium content (figure 5.19). Although small amounts of Er did not effect the position of the silicon absorption edge, larger amounts did reverse the shifted edge back to the position of bulk silicon. Through AFM images it was seen that with the addition of large amounts of Er, nanoparticles were no longer produced and most likely larger structures of silicon and Er are formed[26]. This shows that small amounts of Er can be

added to Si or Ge without disrupting the structure of the nanoparticles or the quantum confinement effects. This preliminary study showed that Er doping of silicon nanoparticles is possible using this method. In addition, there is promise that the produced materials may contain the optically active Er^{3+} state that is required for any technological uses.
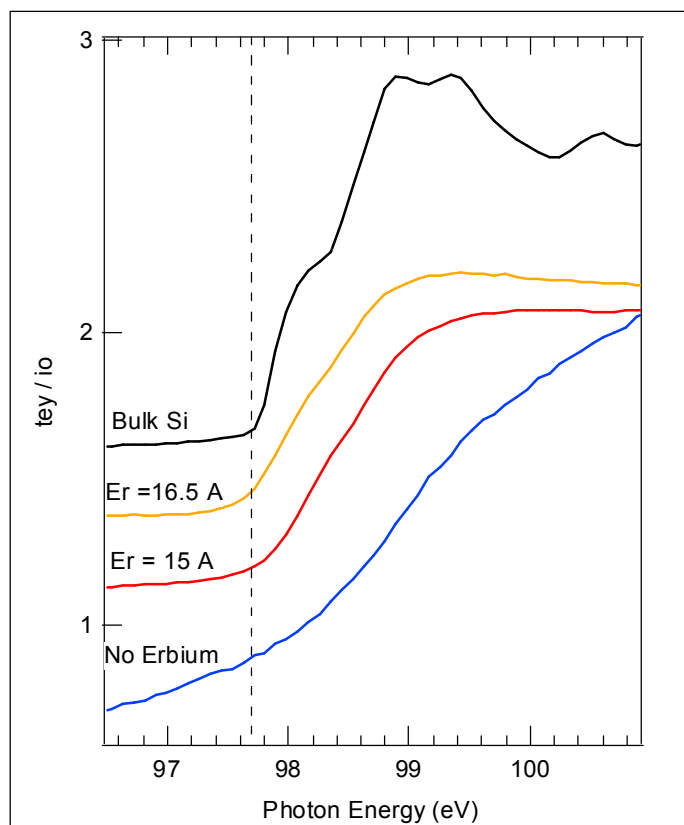
Fig. 5.18: Si $L_{2,3}$ edge spectra of Er doped silicon nanoparticles. Small amounts of Er added to the nanoparticles does not change the electronic structure drastically.
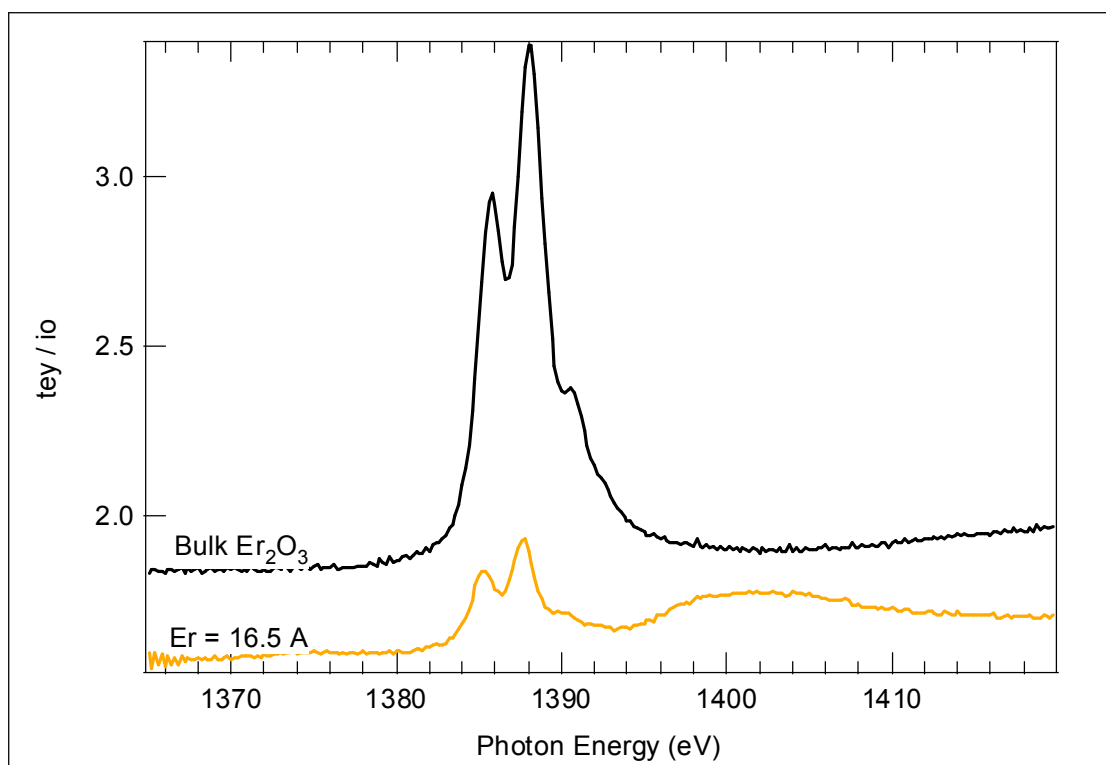
Fig. 5.19: Erbium edge of Er doped silicon nanoparticles. Bulk Er_2O_3 compared to the nanoparticle samples shows that Er is present in the nanoparticles.

References

1   A. Bianconi, "Core excitons and inner well resonances in surface soft x-ray absorption (SSXA) spectra," Surface Science **89**, 41-50 (1979).

2   C. Bostedt, University of Hamburg, 2002.

3   A. D. Yoffe, "Low-dimensional systems: quantum size effects and electronic properties of semiconductor microcrystallites (zero-dimensional systems) and some quasi-two-dimensional systems," Advances in Physics **42** (2), 173-266 (1993).

4   S. Eisebitt, Patitsas, S.N., Luning, J., Rubensson, J.E., Tiedje, T., van Buuren, T., Eberhardt, W., "Soft-x-ray fluorescence of porous silicon: electronic structure of si nanostructures," Europhysics letters **37**, 133 (1997).

5   J. Heitmann, F. Muller, L. Yi et al., "Excitons in Si nanocrystals: Confinement and migration effects," Physical Review B **69**, 195309 (2004).

6   A. Zimina, Eisebitt, S., Eberhardt, W., "Electronic structure and chemical environment of silicon nanoclusters embedded in a silicon dioxide matrix," Applied physics letters **88**, 163103 (2006).

7   J. Luning, Rockenberger, J., Eisebitt, S., Rubensson, J.-E., Karl, A., Kornowski, A., Weller, H., Eberhardt, W., "Soft X-ray spectroscopy of single sized CdS nanocrystals: size confinement and electronic structure," Solid State Communications **112**, 5-9 (1999).

8   A.J. Williamson, Bostedt, C., van Buuren, T., Willey, T.M., Terminello, L., Galli, G., Pizzagalli, L., "Probing the Electronic Density of States of Germanium Nanoparticles: A Method for Determining Atomic Structure," Nanoletters **4** (6), 1041-1045 (2004).

9   C. Striemer, Krishnan, R., Fauchet, P., "The Development of Naocrystalline Silicon for Emerging Microelectronic and Nanoelectric Applications," JOM **56** (10), 20-25 (2004).

10   C. Bostedt, van Buuren, T., Willey, T.M., Terminello, L., "Controlling the electronic structure of nanocrystal assemblies by variation of the particle-particle interaction," Applied physics letters **85** (22), 5334 (2004).

11   A.R. Kortan, R. Hull, R.L. Opila et al., "Nucleation and growth of CdSe on ZnS quantum crystallite seeds, and vice versa, in inverse micelle media," Journal of american chemical society **112**, 1327 (1990).

12   R. Q. Zhang, J. Costa, and E. Bertran, "Role of structural saturation and geometry in the luminescence of silicon-based nanostructured materials," Physical Review B **53** (12), 7847 (1996).

13   S. Godefroo, M. Hayne, M. JIVANESCU et al., "Classification and control of the origin of photoluminescence from Si nanocrystals," Nature nanotechnology **3** (174) (2008).

14   A.P. Alivisatos, "Semiconductor clusters, nanocrystals and quantum dots," Science **271** (5251), 933-937 (1996).

15   D.A. Lapiano-Smith, F.J. Himpsel, and L.J. Terminello, "The chemisorption and reaction of diethysilane on silicon (100) and (111) surfaces," Journal of applied physics **74**, 5842 (1993).

16   E.H. Lay, Kirakosian, A., Lin, J.-L., Petrovykh, D.Y., Crain, J.N., Himpsel, F.J., "Alignment of liquid crystals on stepped and passivated silicon templates prepared in ultrahigh vacuum," Langmuir **16**, 6731-6738 (2000).

17   Luning J. Eisebitt S., Rubensson J.E., Settels, A., Dederichs, P.H., Eberhardt W., Patitsas S.N., Tiedge T., "Resonant inelastic soft x-ray scattering at the Si L_3

edge experiment and theory," Journal of electron spectroscopy and related phenomena **93**, 245-250 (1998).

[18] R. E. Hummel, *Electonic properties of materials*. (Springer, New York, NY, 2001).

[19] T. van Buuren, Dinh, L.N., Chase, L.L., Siekhaus, W.J., Terminello, L.J., "Changes in the electronic properties of si nanocrystals as a function of particle size," Physical Review Letters **80** (17), 3805 (1998).

[20] F. Reboredo, Franceschetti, A., Zunger, A., "Dark exitons due to direct coulomb interactions in silicon quantum dots," physical Review B **61** (19), 13073 (2000).

[21] A. Puzder, Williamson, A.J., Grossman, J.C., Galli, G., "Computational Studies of the optical emission of silicon nanocrystals," Journal of american chemical society **125**, 2786-2791 (2003).

[22] A. Puzder, A.J. Williamson, F.A. Reboredo et al., "Structural stability and optical properties of nanomaterials with reconstructed surfaces," Physical review letters **91** (15), 157405 (2003).

[23] F. Reboredo, Galli, G., "Theory of alkyl-terminated silicon quantum dots," Journal of physical Chemistry B **109**, 1072-1078 (2005).

[24] M. Fujii, Yoshida, M., Hayashi, S., Yamamoto, K., "Photoluminescence from SiO_2 films containing Si nanocrystals and Er: Effects of nanocrystalline size on the photoluminescence efficiency of Er^{3+}," Journal of applied physics **84** (8), 4525 (1998).

[25] A.J. Kenyon, "Quantum confinement in rare-earth doped semiconductor systems," Current Opinion in Solid State and Materials Science **7**, 143-149 (2003).

[26] R.W. Meulenberg, T.M. Willey, J.R.I. Lee et al., "Photoemission and X-Ray Absorption Studies of Er Centers in Ge Nanocrystals," In progress (2008).

Chapter 6:

Electronic Structure of Silicon Nanocrystal Multilayers

In this chapter, I will discuss how the synthetic strategies used in producing silicon nanoparticles can affect the electronic structure of the nanoparticles. Synchrotron based x-ray absorption spectroscopy (XAS) and soft x-ray fluorescence (SXF) techniques have been used to characterize the electronic structure of crystallized amorphous silicon/silica (a-Si/SiO$_2$) and nanocrystalline silicon/silica (nc-Si/SiO$_2$) multilayer samples of thicknesses below 10 nm. In this chapter, I report on the conduction and valence band edges of nanoparticles in both of these samples and compare our highly localized electronic measurements with photoluminescence data in an effort to determine the true source of luminescence. The electronic structure from the nc-Si/SiO$_2$ multilayers will be compared to that of the evaporated nanoparticles (Chapter 5) and interestingly, these two samples exhibit very different behavior.

6.1 Amorphous Si/SiO$_2$ Multilayers

These samples were prepared by Rishikesh Krishnan at the University of Rochester under the supervision of Philippe Fauchet[1]. Multilayer samples are made by alternately depositing amorphous Si and amorphous SiO$_2$ films on Si wafers through radio frequency (RF) magnetron sputtering. RF magnetron sputtering is a deposition technique where a target is bombarded with ions resulting in the ejection of atoms and molecules. The samples were then characterized using transmission electron microscopy (TEM) to determine layer thickness.

The electronic structure was characterized using x-ray absorption spectroscopy (XAS) and soft x-ray fluorescence (SXF) techniques. These experiments were performed at the undulator beamline 8.01 at the Advanced Light Source at Lawrence Berkeley National Laboratory[2]. The x-ray energy is scanned through the absorption edges and is detected in total electron yield (TEY), where the total photocurrent into the sample is collected as a function of photon energy. All spectra are normalized to the current given from a highly transmissive gold grid. The resolution of this experiment was less than 0.1 eV at the Si $L_{2,3}$ edge. The SXF spectra were measured in the fluorescence endstation on a Rowland circle grating emission spectrometer with an area detector. The spectrometer is situated at an angle 90 degrees from the incident x-rays. In SXF the incident x-ray energy is kept constant and the spectrometer detects the emitted photons within the selected range. The presented data was all collected at an excitation energy of 98.2 eV.

XAS and SXF have been used to map the band edges of the a-Si/SiO_2 multilayers. XAS and SXF give element specific information about the electronic structure which can distinguish between the amorphous silicon and amorphous SiO_2 layers. In XAS a SiO_2 peak is present at 105 eV because of the change in oxidation state of the silicon in Si-O. In SXF the electrons are excited below this peak to avoid exciting the oxidized silicon, as the observed VB features would be dominated by contributions from the silica layer.

The amorphous silicon (a-Si) SXF spectrum has much broader, less defined peaks than a crystalline silicon SXF spectrum therefore the collected data is compared against a thicker amorphous silicon spectrum rather than a bulk crystalline Si. Although the thickest amorphous Si sample is fairly small in size, the spectrum does not exhibit quantum confinement and is deemed a suitable reference standard for our experiments. The SXF spectra of the a-Si samples are shown in figure 6.1a and it is clearly seen that

no shift is seen in the valence band edge with decreasing layer thickness. These results are contrary to those observed by Lockwood et. al. where the x-ray photoelectron spectroscopy (XPS), using a Al Kα x-ray source, measured the valence band shift of materials synthesized in the same method[3]. The difference between in these seemingly similar experiments can be explained by considering the inherent difference between SXF and XPS. XPS measures the binding energy of electrons emitted from the core levels. Since electrons have a much shorter mean free path at the measured energy of 1.5 keV, only the top layer of the sample is penetrated. SXF is a bulk technique since photons have a larger mean free path and is therefore measuring the energy of the occupied electrons from the all the layers in the sample. Also, the use of a laboratory x-ray source makes the measurements by Lockwood et. al. questionable since low signal to noise ratios are often seen in spectra measured at this energy range. Synchrotron measurements have the benefit of much higher flux leading to clear, high signal to noise spectra. These advantages make SXF a better technique to use to measure the valence band of these samples.

The Si $L_{2,3}$ XAS edge gives specific information about the *s* and *d* DOS. The a-Si/SiO$_2$ XAS data showed that the conduction band does exhibit a size dependent (i.e. layer thickness) shift when compared to a thick amorphous Si reference (Figure 6.1b), consistent with a previous report by Lockwood et. al.[3] The conduction and valence band shifts as a function of layer thickness are shown in figure 6.2. Also included in this plot are the results presented in the previous chapter from the gas phase synthesized Si nanoparticles. Since the a-Si/SiO$_2$ multilayers are confined in only one direction, one can envision figure 6.2 as contrasting the electronic structure of 1-D confined (multilayers) and 3-D confined (nanoparticles) materials. Although confinement may play a large role in any observed shifts in the CB edge, one must consider the effect that lattice mismatch induced strain has on the absolute energy of the CB edge[1]. A conduction band shift
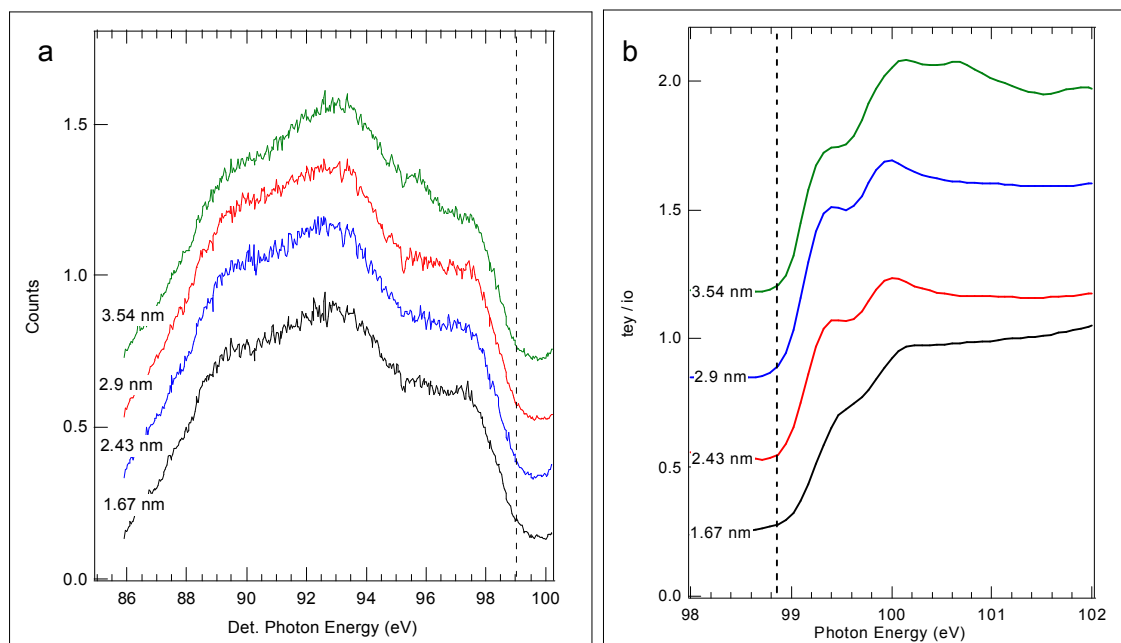
Fig. 6.1: a) SXF data shows that the valence band of the amorphous multilayer samples does not shift with decreasing size except for a slight shift in the smallest sample, while b) the XAS does show a small shift with decreasing layer thickness.
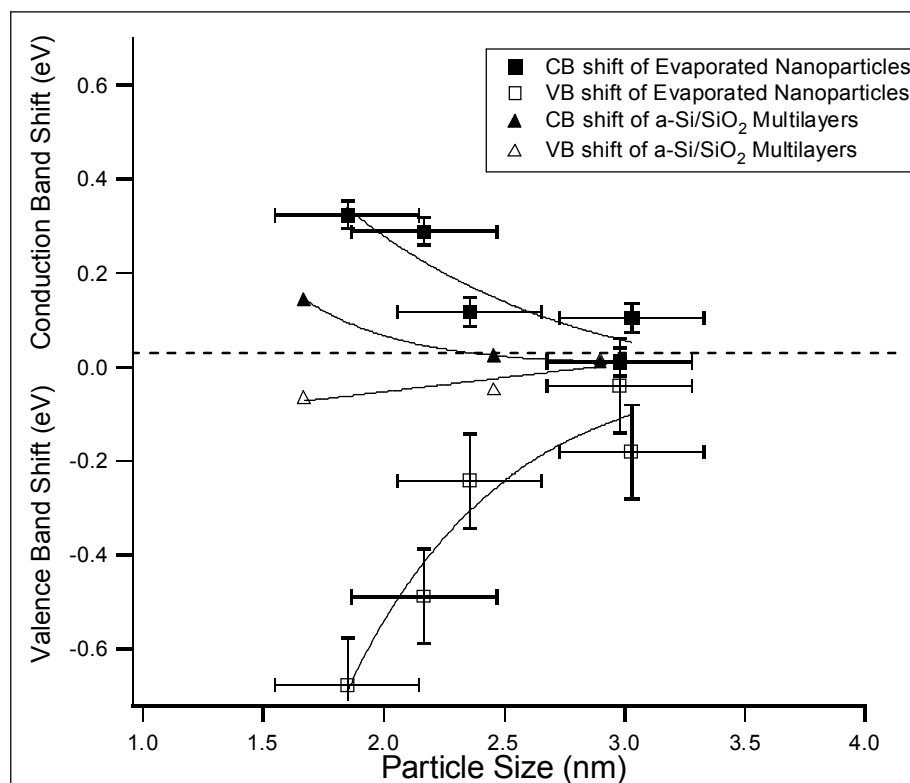
Fig. 6.2: CB and VB shifts of a-Si/SiO$_2$ multilayer samples compared to CB and VB shifts of evaporated silicon nanoparticles.

towards higher energy has been observed in strained Si and strained Si/Ge alloys by Batson[4]. As the strain in the thinner layered samples is likely to be higher than in the thicker layered sample, it is conceivable that strain effects may play a role in the size dependent shifting of the conduction band. To add further evidence to strain as a factor, Raman spectroscopy of these samples showed a strain induced shift of the Raman peak[1]. This is consistent with previous Raman measurements of porous silicon in which strain was also cited for the shifting of the Raman peak[5].

6.2 Nanocrystalline Si/SiO$_2$ Multilayers

The nanocrystalline Si/SiO$_2$ (nc-Si/SiO$_2$) multilayers were synthesized by Krishnan[1] by first producing a-Si/SiO$_2$ multilayers Followed by subsequent crystallization of the Si layers producing oxide terminated nanocrystals[1]. The a-Si layers were crystallized by rapid thermal anneal (RTA) at 950 ˚C followed by a longer furnace anneal at 1050 ˚C. The RTA serves to induce nucleation of the nanocrystals and the long furnace anneal allows growth to the desired size as well as decreasing any defects in the layers[1,6,7]. The samples were then characterized using transmission electron microscopy (TEM) to determine layer thickness, morphology and structure of the nanoparticles. The electronic structure of these samples was investigated, as with the previous amorphous samples, using XAS and SXF. These measurements were also taken under the same experimental conditions at ALS in LBL.

The multilayer samples were imaged using TEM to determine layer thickness and nanoparticle morphology (figure 6.3a). The TEM image shows that the interfaces between the Si and SiO$_2$ are very abrupt with smooth layers. High resolution images and diffraction confirm that the SiO$_2$ is amorphous and was not crystallized by the annealing step. The high resolution image in figure 6.3b shows the presence of lattice fringes in the particles indicating that they are crystalline. The nanoparticles are elliptical in shape with

oxide

Si

20 nm

5 nm
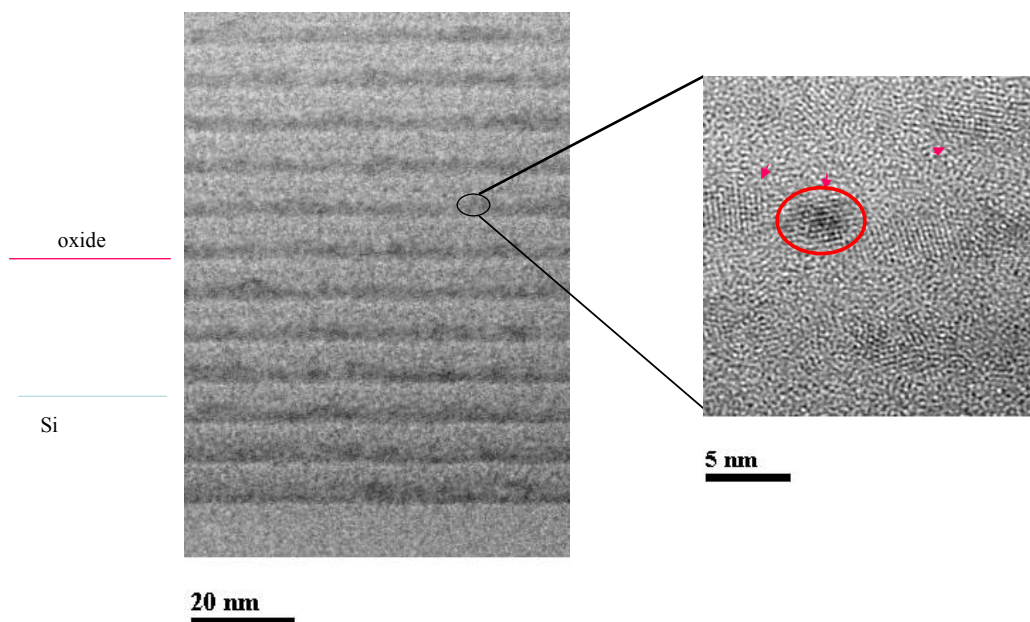
Fig. 6.3: a) Cross section TEM images of an nc-Si/a-SiO2 multilayer showing periodicity of the nc-Si and a-SiO2 layers. The nc-Si layer was 3.2 nm thick and the a-SiO2 layer was 5 nm thick. b) High resolution lattice image at thinner areas. The Si nano-clusters are separate from each other and are indicated by the arrows. The nanoparticles are elliptical in shape with typical sizes of this particular sample, lateral dimension 4-6 nm, height 2-3 nm. Images reproduced Krishnan[1].

typical sizes of this particular sample, lateral dimension 4-6 nm, height 2-3 nm. XAS and SXF have been used to map the band gap of the nc-Si/SiO$_2$ multilayers. XAS and SXF give element specific information about the electronic structure which can distinguish between the crystallized silicon and amorphous SiO$_2$ layers. In XAS a SiO$_2$ peak is present at 105 eV because of the change in oxidation state of the silicon in Si-O. As with the amorphous samples, in SXF the electrons are excited below this peak to avoid exciting the oxidized silicon.

It was ensured that only the Si nanoparticle cores are measured in the SXF spectra and not the SiO$_2$ layers, by exciting only the 2p core levels of Si and omitting the oxide region of the spectrum which occur at higher energy. Figure 6.4a shows the SXF spectrum of the samples decreasing in size from 10 nm to 1.8 nm. These spectra are compared to the bulk spectrum with the smallest samples showing a shift in the edge toward lower energy, consistent with quantum confinement. The distinct peaks in the SXF spectra indicate crystalline nanoparticles since amorphous silicon emission spectra have broader, much less defined peaks[8].

Figure 6.4b shows the XAS spectra at the Si L$_{2,3}$ edges from nc-Si/SiO$_2$ multilayers with varying thickness of nc-Si layer. It can be seen that these samples show a size dependent absorption edge shift when compared to the bulk silicon spectrum. The thickest samples do not show any shift from the edge of bulk silicon and, in fact, are somewhat shifted toward lower energy. The absorption spectra show clear spin orbit splitting of the 2p$_{1/2}$ and 2p$_{3/2}$ components which has been observed in SiO/SiO$_2$ multilayer samples[9] but this is not seen in either porous silicon or evaporated silicon nanoparticles[10-12]. This lack of spin-orbit splitting feature is most likely due to surface disorder and not size distribution. Because of the RTA in this synthesis, the sample surfaces are most likely more ordered with fewer defects than the samples produced with the gas phase synthesis. It is possible that by annealing the evaporated particles

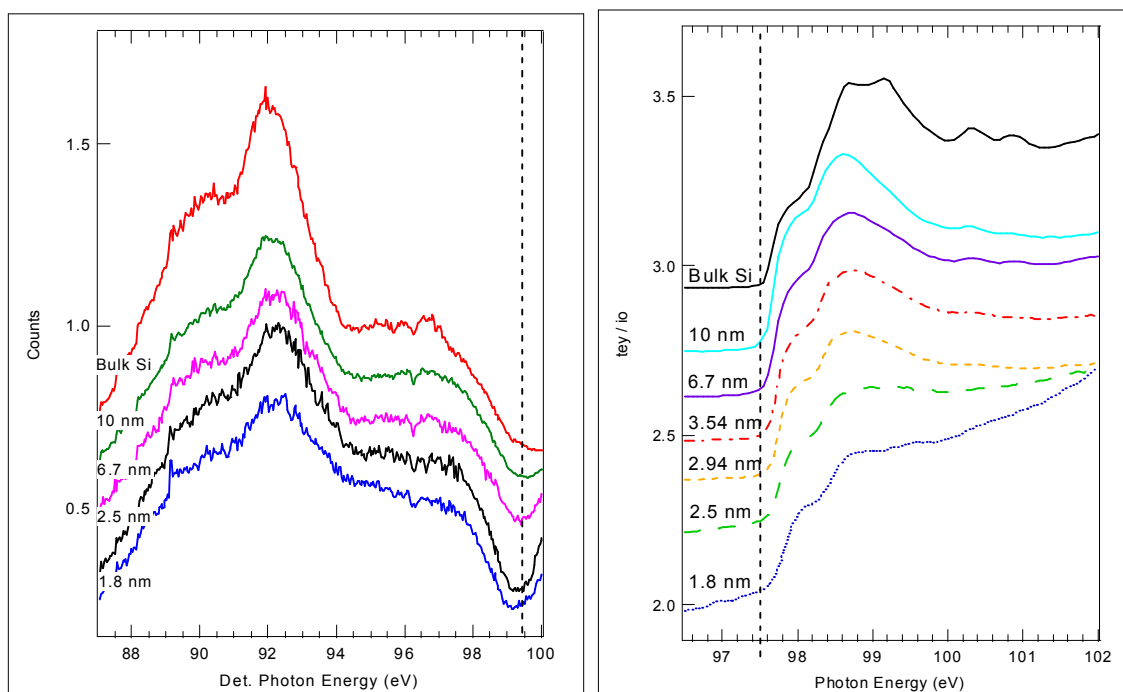**Fig. 6.4:** The a) SXF and b) XAS spectra of $L_{2,3}$ edge spectra of crystallized multilayer samples compared to bulk silicon. Layer thickness decreases from top to bottom in both plots. a) The SXF edges of the thinnest samples show shifts up to 0.3 eV. In b) the absorption edge position of the thickest sample, 10 nm, shows no difference from bulk silicon but the thinnest sample, 1.8 nm, is edge shifted by 0.18 eV.

the spin-orbit splitting features would appear in the spectra. The conduction and valence bands shift as a function of layer thickness of the nc-Si/SiO$_2$ multilayer samples and are plotted in figure 6.5 with the total band gap as determined by synchrotron methods of the nc-Si/SiO$_2$ multilayers displayed in figure 6.6. For comparison, photoluminescence (PL) spectroscopy peak energies are included on this plot. The PL peak energies give a lower bandgap than that observed by our methods. This may be because surface states are contributing to the PL and creating inter-gap states that decrease the PL peak energy. A recent study on the source of PL from similar structures showed that surface states may be the source of PL from these structures if the surface defects are not completely eliminated by the anneal[13].

6.3 Electronic Structure Comparison to Evaporated Particles

As the nc-Si/SiO$_2$ multilayer particles are intrinsically passivated as a by-product of the synthesis, comparison of this system versus the thermal evaporation synthesis in Chapter 5 can be performed. Although the nc-Si/SiO$_2$ particles exhibit good luminescence properties, the quantum confinement induced shifts in both the conduction and valence bands are smaller than those observed in the evaporated nanoparticle synthesis. Although the size range of the two nanoparticle samples is similar, the edge shifts are quite different both in magnitude and the general trend of the data.

The VB and CB edge shifts of the nc-Si/SiO$_2$ particles were found to be smaller than either the isolated or methanol passivated nanoparticles produced via the evaporation synthesis. The multilayer band shifts are compared to samples synthesized via evaporation methods in figure 6.7. The multilayer samples show the edge shifts increasing with decreasing sample size. For the nc-Si/SiO$_2$ samples the ratio of valence to conduction band shift is 1.5:1 which is different than the previously reported ratio of
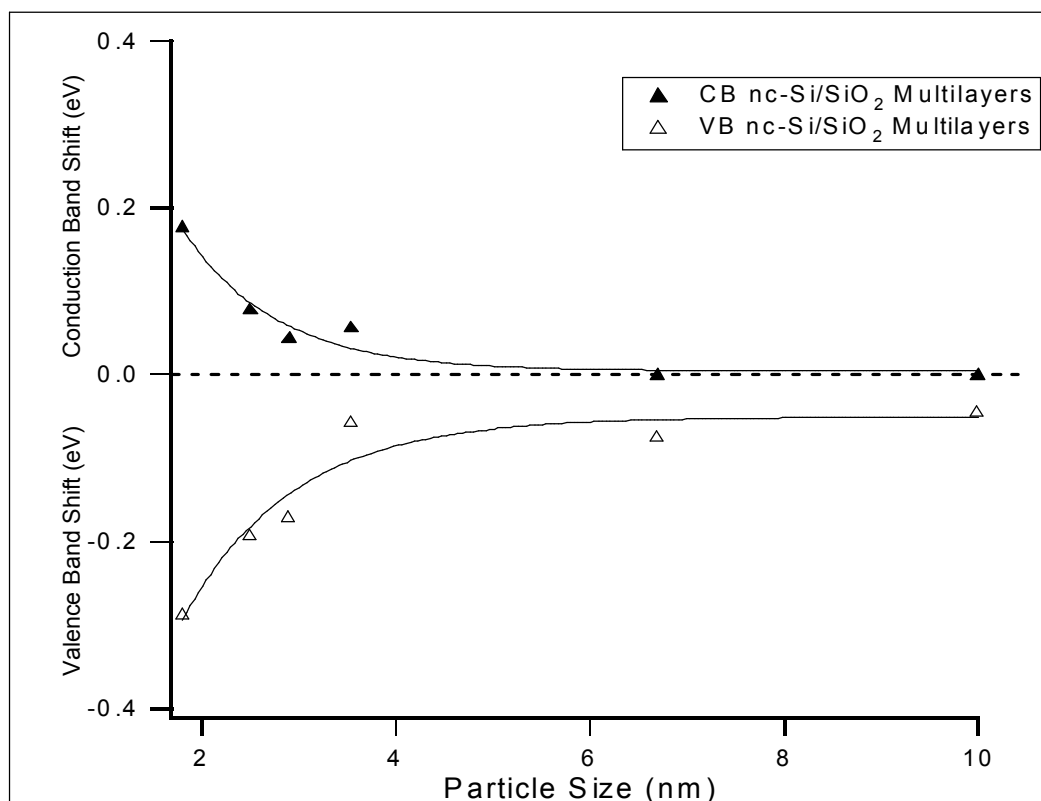
Fig. 6.5: Changes in conduction and valence bands as a function of layer thickness. Edge shifts are measured against bulk silicon spectra in both the XAS and SXF measurements. Valence band shifts are roughly 1.8 times the shift of the conduction band.

Fig. 6.6: Bandgap as a function of layer thickness squares are determined by Eg = ΔCB+ΔVB+1.12 from the XAS and SXF data. Triangles are the PL peak energies from multilayer samples reproduced from[1].

Fig. 6.7: Comparison of band shifts of evaporated silicon nanoparticles and multilayer samples.

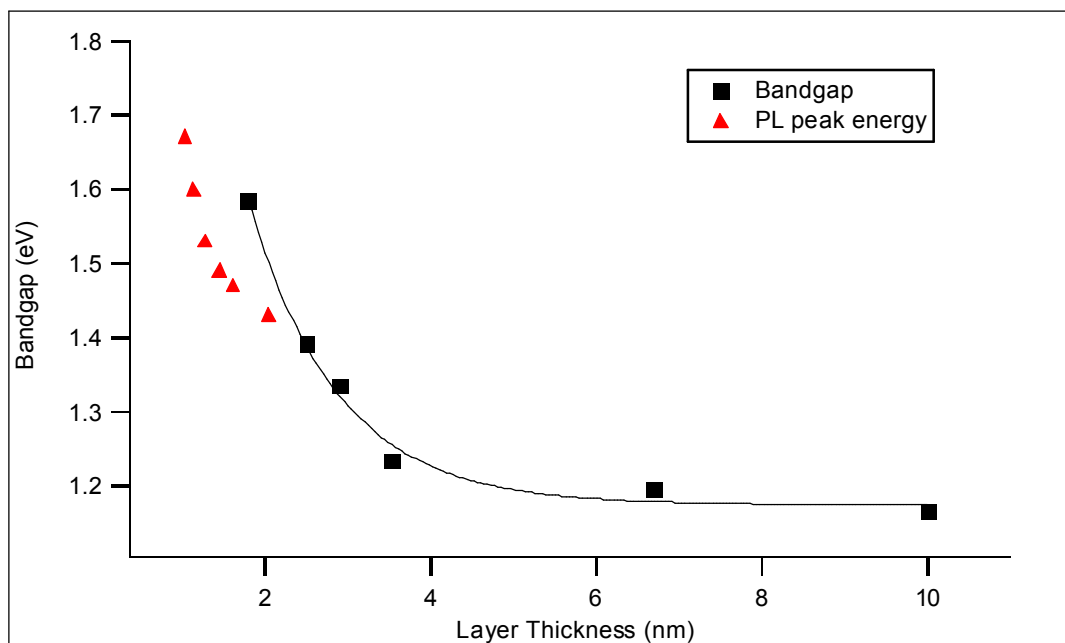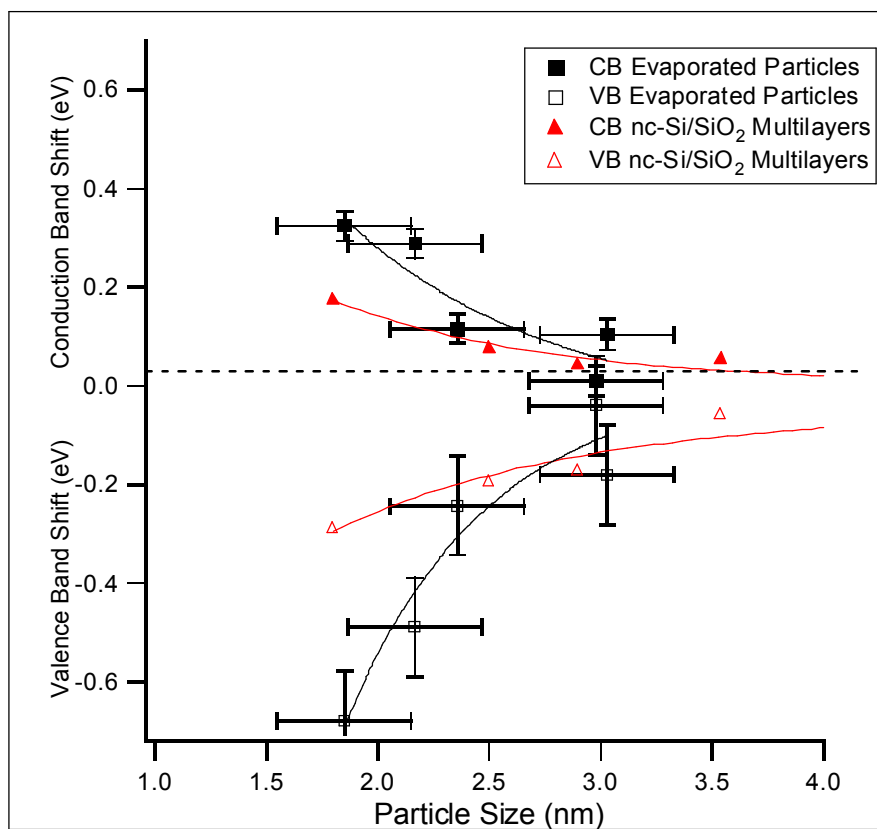2:1[12] measured from samples synthesized via evaporation techniques and also from the data from the evaporation samples from previous chapters.

The differences in the electronic structures between these two types of samples may arise from a number of sources. First, the multilayer samples are elliptical while the evaporated particles are spherical. TEM images showed that the multilayer particles are not spherical but slightly elliptical in shape. Although the nanoparticle size is confined in one direction by the layer thickness, the planar directions do not have this restriction. TEM images of the planar view of the nanocrystalline multilayer show the shape of the nanocrystals for layers smaller than 5 nm to be roughly ellipsoidal with aspect ratios (W/L) ranging from 1:1.1 to 1:1.4[1]. Samples of layers larger than 5 nm have higher aspect ratios, 1:3 to 1:4, and are more rectangular in shape. Theoretical studies on the effect of shape on the confinement in nanocrystals, indicate that the bandgap is affected by elongation in one direction [14,15]. These calculations have not been performed on silicon nanoparticles however, and the effect on these structures is unknown. A comparison can be made to the confinement of nanorods and nanoparticles. A study performed on InAs nanorods showed that the ratio of length to diameter affected the bandgap measurements dramatically[16,17]. As the length/diameter decreased, the bandgap increased giving evidence that an elongation of one direction can decrease the bandgap[16,17]. Second, the difference in surface passivation in these two types of samples. The evaporated samples are passivated using methanol while the multilayer samples are completely surrounded by oxide. Calculations on the effects of different surface passivations have shown that oxygen passivation can lower the bandgap of the nanoparticles if the surface is not reconstructed[18,19]. This may be due to the more localized oxygen states that create a stronger electron-hole binding energy[18]. Third, the synthesis method of the multilayer samples could also be causing the lack of edge shifts in these samples. There is a large lattice mismatch between amorphous silicon and

silica which leads to a large amount of tensile stress in the annealed samples. It is believed that the stress is annealed out in the recrystallization process but is the possibility exists that some stress remains and contributes to the DOS. This is often observed in strained silicon samples where the conduction band is shifted toward higher energy causing a widening of the bandgap without any quantum confinement effects present[4].

A graph summarizing the band gap for the multilayer samples and the evaporated samples is shown in figure 6.8. The bandgap of the multilayer nanoparticle samples was also measured using photoluminescence spectroscopy. This measurement obtained bandgaps smaller than that using the synchrotron methods possibly due to inner-gap states that decrease the PL energy.

Similar nc-multilayer samples were characterized using XAS and SXF by Zimina et. al.[9] The results we have obtained from the nc-Si/SiO$_2$ multilayer samples are contrary to the results found by Zimina et. al.[9] in their study of Si nanocrystals crystallized from SiO/SiO$_2$ multilayers. That study found that although the valence band of similar samples was shifted by 0.5 eV in a 2 nm sample, no shift in the conduction band spectrum of the sample was observed. The samples measured here clearly show a shift in the absorption edge toward higher energy with the smallest, 1.8 nm, sample showing a 0.17 eV shift, well within the resolution of this technique. It can also be noted that the valence band shifts in our study are only half the magnitude observed by Zimina. Differences of this magnitude could only be due to very different DOS in the two structures which is puzzling since both structures emit bright PL spectra in the same region. This clearly points to luminescence sources other than quantum confinement in these multilayer samples.
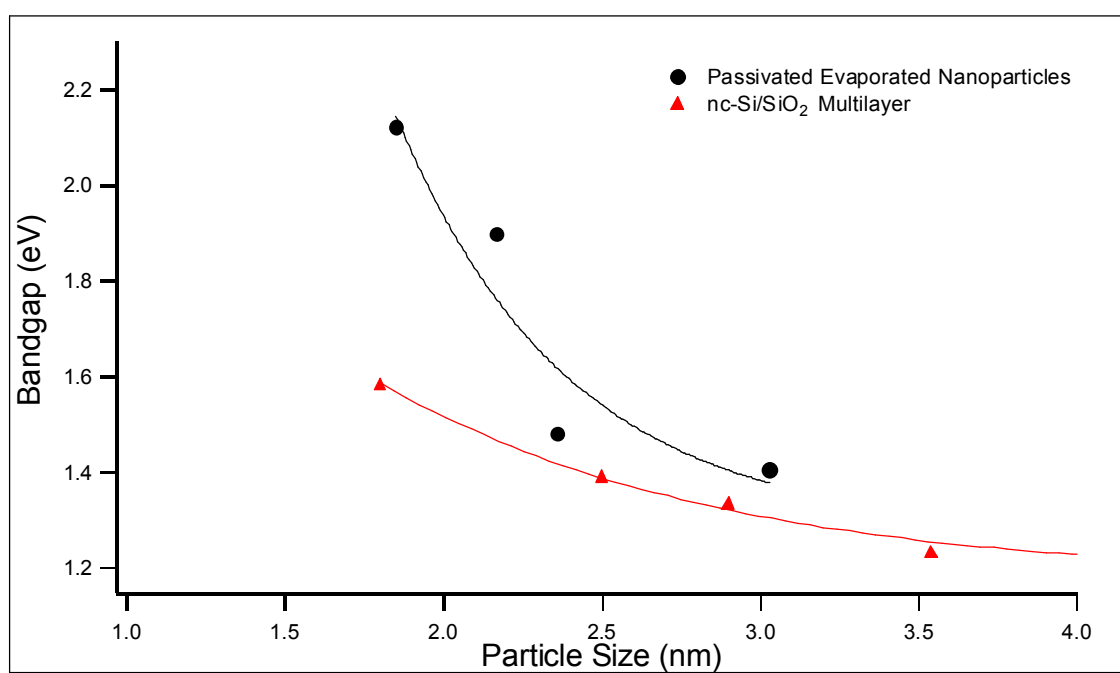
Fig. 6.8: Comparison of the measured bandgap of thermally evaporated nanoparticles to recrystallized multilayer samples.

References

[1] R. Krishnan, University of Rochester, 2005.

[2] J.J. Jia, Callcott, T.A., Yurkas, J., Ellis, A.W., Himpsel, F.J., Samant, M.G., Stohr, J., Ederer, D.L., Carlisle, J.A., Hudson, E.A., Terminello, L.J., Shuh, D.K., Perera, R.C.C., "First experimental results from IBM/TENN/TULANE/LLNL/LBL undulator beamline at the advanced light source," Review of scientific instruments **66** (2), 1394 (1995).

[3] D.J. Lockwood, Z.H. Lu, and J.-M. Baribeau, "Quantum confined luminescence in Si/SiO$_2$ superlattices," Physical Review Letters **76** (3), 539 (1996).

[4] P.E. Batson, "Near-edge conduction band electonic states in SiGe alloys," Journal of Electron Microscopy **49** (2), 267 (2000).

[5] J. von Behren, T. van Buuren, M. Zacharias et al., "Quantum confinement in nanoscale silicon: the correlation of size with bandgap and luminescence," Solid State Communications **105** (5), 317-322 (1998).

[6] L. Tsybeskov, Hirschman, K.D., Duttagupta, S.P., Zacharias, M., Fauchet, P.M., McCaffrey, J.P., Lockwood, D.J., "Nanocrystalline-silicon superlattice produced by controlled recrystallization," Applied physics letters **71**, 43-45 (1998).

[7] Lockwood D.J. Grom G.F., McCaffrey J.P., Labbe H.J., Fauchet P.M., White B., Diener J., Kovalev D., Koch F., Tsybeskov L., "Ordering and self-organization in nanocrystalline silicon," Nature **407**, 358 (2000).

[8] K.E. Miyano, D.L. Ederer, T. A. Calcott et al., "Band structure effects in the excitation-energy dependence of Si L$_{2,3}$ x-ray emission spectra," Physical Review B **48**, 1918 (1993).

[9] A. Zimina, Eisebitt, S., Eberhardt, W., "Electronic structure and chemical environment of silicon nanoclusters embedded in a silicon dioxide matrix," Applied physics letters **88**, 163103 (2006).

[10] Y.F. Hu, Boukherroub R. Sham, T.K., "Near edge x-ray absorption fine structure spectroscopy of chemically modified porous silicon," Journal of electron spectroscopy and related phenomena **135**, 143-147 (2004).

[11] T. van Buuren, Tiedje, T., Dahn, J.R., Way, B.M., "Evidence for quantum confinement in porous silicon from soft x-ray absorption," applied physics letters **60**, 3013 (1992).

[12] T. van Buuren, Dinh, L.N., Chase, L.L., Siekhaus, W.J., Terminello, L.J., "Changes in the electronic properties of si nanocrystals as a function of particle size," Physical Review Letters **80** (17), 3805 (1998).

[13] S. Godefroo, M. Hayne, M. JIVANESCU et al., "Classification and control of the origin of photoluminescence from Si nanocrystals," Nature nanotechnology **3** (174) (2008).

[14] J. Li, Wang, L.-W., "Shape effects on electronic states of nanocrystals," Nanoletters **3** (10), 1357-1363 (2003).

[15] Q. Zhao, Graf, P., Jones, W., Franceschetti, A., Li, J., Wang, L.-W., Kim, K., "Shape dependence of band-edge exciton fine structure in CdSe nanocrystals," Nanoletters **7** (11), 3274-3280 (2007).

[16] W. H. Buhro and V.L. Colvin, "Semiconductor Nanocrystals: Shape matters," Nature materials **2**, 138 (2003).

[17] S. Kan, T. Mokari, E. Rothenberg et al., "Synthesis and size-dependent properties of zinc-blende semiconductor quantum rods," Nature Materials **2**, 155 (2003).

[18] A. Puzder, Williamson, A.J., Grossman, J.C., Galli, G., "Surface chemistry of silicon nanoclusters," Physical Review Letters **88** (9), 097401 (2002).

[19] E. Draeger, Grossman, J., Williamson, A., Galli, G., "Optical properties of passivated silicon nanoclusters: The role of synthesis," Journal of chemical physcis **120** (22), 10807 (2004).

Chapter 7:

Conclusions and Future Work

In this thesis work, the electronic structure of silicon nanoparticles prepared by various synthetic methods was investigated. Nanoparticle samples produced via two different synthesis methods were investigated: (1) a thermal evaporation synthesis and (2) recrystallization of amorphous silicon multilayers. Both synthetic methods yielded similar sizes and shapes of Si nanoparticles but gave very different electronic structure results.

In Chapter 5, silicon nanoparticles were synthesized via thermal evaporation. This synthesis allows for the production of crystalline silicon nanoparticles in a reproducible manner in an ultra-clean environment. In addition, the surface chemistry of the particles and particle number density proximity can be controlled in an effort to engineer the nanoparticle properties. These studies demonstrated that properties such as proximity (i.e. interaction of particles), which have sometimes previously been overlooked, do significantly affect the electronic properties of the nanoparticle. The conduction band edge of isolated, unpassivated particles was found to shift toward higher energy with decreasing particle size consistent with quantum confinement theory. Multiple layers of unpassivated nanoparticles, however, did not show size dependent shifts. Electronic correlation of the unpassivated nanoparticles (i.e. the particle-particle interaction) leads to, essentially, bulk band edge positions without quantum confinement effects because of overlapping wavefunctions that no longer confine the electron to a single particle. These experiments on proximity effects on the electronic structure

suggested that surface passivation is necessary for the conservation of quantum confinement effects and the engineering of electronic properties in Si nanoparticles.

Among the molecules selected for surface passivation of the Si nanoparticles, methanol proved to be an effective method to preserve quantum confinement effects that were observe din the isolated, unpassivated system. Although the band edge shifts of methanol passivated particles were not quite the magnitude of the isolated particles, the surface passivation scheme did allow for the synthesis of thick layers of nanoparticles, a feat unachievable for thick unpassivated nanoparticle films. Of particular note, the surface passivation allowed for the measurement of the valence band edge spectra via soft x-ray fluorescence. The surprising result was that ethanol did not increase the passivation effects and in very thick samples no edge shifts were observed.

Successful measurement of the valence band edge along with the conduction band measurements allowed for a determination of the entire band gap of the passivated nanoparticles. The band gaps of the methanol terminated Si particle are similar to the values obtained for hydrogen termination Si particles[1]. An interesting question that can be studied in the future is whether the slight deviations in band gaps between hydrogen and methanol terminated Si particles arises solely to experimental error or is due to surface termination[2,3].

The continuation of this research will involve the investigation of different alcohol molecules to determine if passivation with longer chain alcohol groups is possible. Other molecules, such as those with thiol groups, may also be attached to the surface of these molecules. With this thiol termination, it is envisioned that an array assembly of nanoparticles may be created via self-assembled monolayers (SAMs). SAMs are molecules which adsorb on a surface and spontaneously order via intramolecular forces (figure 7.1). By creating self assembled arrays of nanoparticles the possibility of integration into optoelectric devices increases.
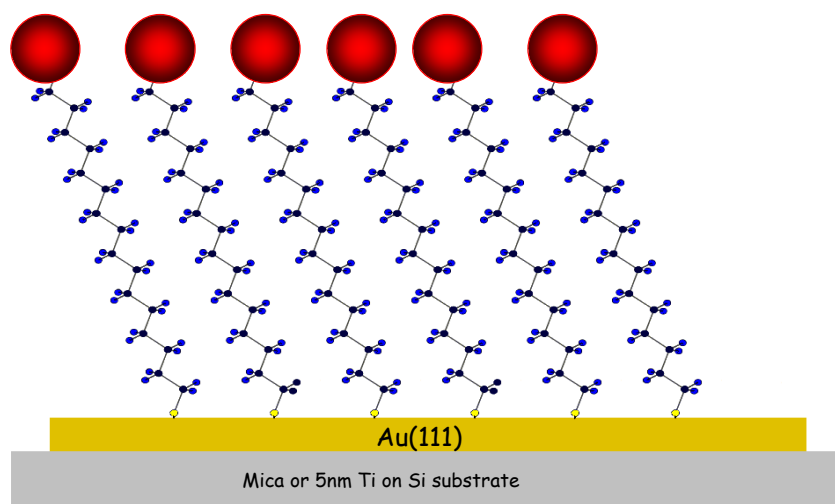
Fig. 7.1: Long chains of organics with a sulfur on one end of the chain assemble into self assembled monolayers (SAMs). The sulfur bonds to a gold surface and van der Waals interactions between chains cause alignment and ordering in SAMs. Silicon nanoparticles can be passivated with a thiolated carbon chain which will then self assemble. Head group of molecule can be changed for chemical functionality and better attachment to nanoparticles.

An obvious area of potential research in the thermally evaporated nanoparticle system is the optical properties. Due to the observation of size dependent band gaps via x-ray spectroscopy, the observation of light emission via photoluminescence (PL) spectroscopy should be feasible. By coupling the optical measurements to the electronic structure measurements presented in this thesis, the source of luminescence can be determined as quantum confinement and surface states have both given evidence to contribute to the PL. The PL experiments are somewhat difficult to perform due to the dilute nature of these samples and although an initial attempt at acquiring this data was made, no conclusive results were obtained. Figure 7.2 shows a preliminary PL spectrum showing luminescence from a thick, methanol passivated nanoparticles. The PL is not completely understood for these particles as an in depth study was not performed.

Part of this thesis included the study if doped Si nanoparticle.. For the doped samples the main goal was to produce erbium doped silicon nanoparticles and understand the effects that the Er dopant had on the Si nanoparticle electronic structure. It was observed that as erbium was evaporated with the silicon, doped nanoparticles were formed and the confinement effects were not diminished until large amounts of erbium were introduced. Further optical experiments on these samples are needed to determine if the nanoparticle can effectively act as an antenna for the erbium centers.

As a comparison to the thermally evaporated nanoparticles, the electronic structures of a-Si/SiO$_2$ and nc-Si/SiO$_2$ multilayer samples were investigated. The a-Si/SiO$_2$ multilayers did show absorption edge (CB) shifts, but did not show any emission edge (VB) shifts. This indicates that the bandgap was widening in these samples but only due to the conduction band and suggest that and interplay of both quantum confinement and strain may be affected the electronic structure in the systems. The nc-Si/SiO$_2$ samples did show both absorption and emission edge shifts but not to the same

ratios as the evaporated nanoparticles. This could be due to passivation or shape differences in the samples.
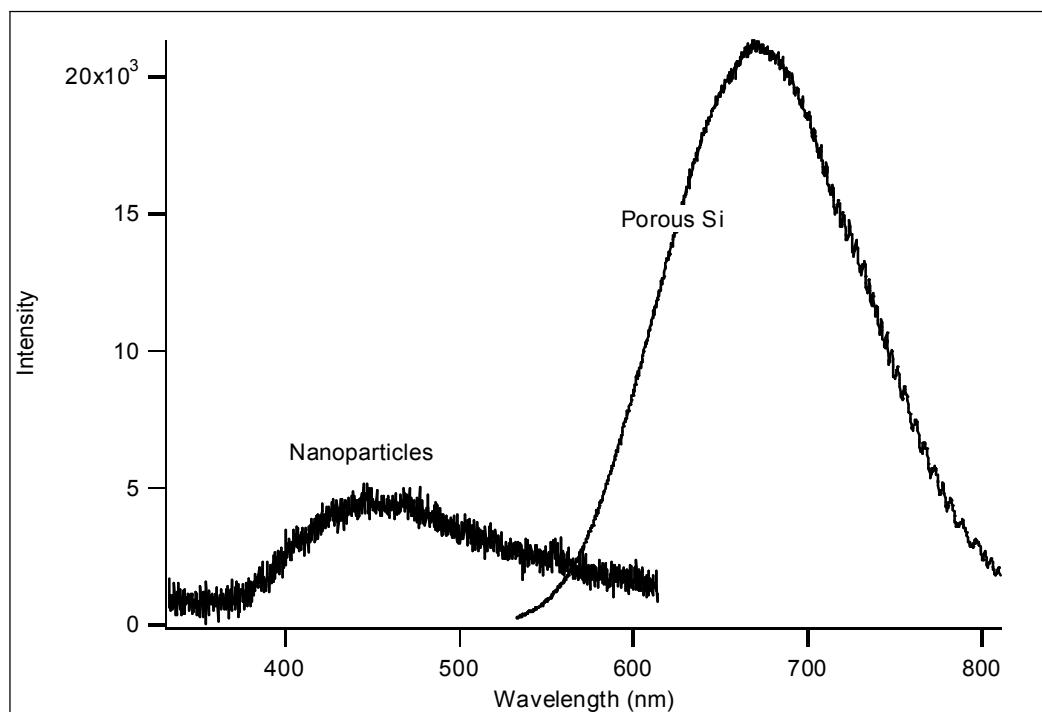
Fig. 7.2: Preliminary photoluminescence spectrum from deposited silicon nanoparticles. The nanoparticle spectrum is shifted toward higher energy than the spectrum of porous silicon.

References

[1] T. van Buuren, Dinh, L.N., Chase, L.L., Siekhaus, W.J., Terminello, L.J., "Changes in the electronic properties of si nanocrystals as a function of particle size," Physical Review Letters **80** (17), 3805 (1998).

[2] E. Draeger, Grossman, J., Williamson, A., Galli, G., "Optical properties of passivated silicon nanoclusters: The role of synthesis," Journal of chemical physcis **120** (22), 10807 (2004).

[3] A. Puzder, Williamson, A.J., Grossman, J.C., Galli, G., "Surface chemistry of silicon nanoclusters," Physical Review Letters **88** (9), 097401 (2002).

Appendix A:

Characterization of laser induced CdTe nanocrystals inside glass microspheres

Abstract

Glass fibers drawn from a bulk borosilicate glass doped with CdTe were heat treated by a CO_2 laser to form microspheres at the fiber tip. The size of the microspheres varied from 50 to 300 microns. Subsequent reheating of the optically clear microspheres by the CO_2 laser resulted in color changes attributed to the formation of CdTe nanocrystals inside the microspheres. Scanning electron microscopy (SEM) and atomic force microscopy (AFM) have confirmed smooth surfaces of the microspheres, which indicate high quality factors associated with whispering gallery microsphere lasers may be possible. The particle concentration and size have been characterized using transmission electron microscopy (TEM) and photoluminescence spectroscopy (PL). The size, chemistry, and optical properties of these CdTe quantum dots will be presented with a discussion of the applicability of these data to the fabrication of microsphere photonic structures.

A.1 Introduction

Previous chapters of this thesis discussed different methods of quantum dot synthesis. One of these was nanoparticle synthesis inside glasses. Quantum dots have been found to be very stable inside glasses and isotropic materials. Some applications require synthesis inside isotropic materials and the natural passivation results in bright

luminescence. Many applications in optics are possible for these materials including amplifiers for waveguides[1], and non-linear optics. The specific application where we are directing our focus of research is that of coupling the light emitted from the quantum dots to a glass microsphere. These microspheres act as a dielectric resonator, amplifying the quantum dot emission possibly to the point of lasing[2-4]. As discussed in chapter 2, quantum dots emit light of every visible color according to their size and they are valuable as an efficient source of any wavelength of light desired. Coupled to the dielectric microspheres, the quantum dot emission could be amplified and used in applications such as environmental detectors and biosensors[5] or lasers[2-4].

Dielectric microspheres have come into the spotlight because of their promise in many areas of technology. These tiny resonators have possible applications ranging from micro-lasers to environmental detectors to microamplifiers to tools of nonlinear optics[2-5]. They have the unique ability to store optical energy for long times in a very small volume and through innovative coupling devices, this energy could be used for signal processing purposes or lasers of very narrow emission line width. Since the spheres either are fabricated from commercial optical fibers or doped glasses, they are very compatible with present telecommunication technology, which makes them even more promising in the area of telecommunications.

The microsphere resonator theory is the so-called whispering gallery modes (WGM), which take their name from the phenomena of the domed ceilings of old cathedral galleries. It has been observed that two people standing many feet apart under a domed ceiling are able to whisper to each other and be heard perfectly some distance away. The sound is transmitted without loss by orbiting the domed ceiling. The same general concept occurs in the glass microspheres. The light orbits the microsphere via total internal reflection similar to light propagation in waveguides. Because the light is stored in a very small area, amplification of the light occurs[6]. Since the light can orbit

around the microsphere for a very long time without significant energy loss, the light coming out of the microsphere is significantly amplified as light continues to be added via a coupling method but experiences very little loss[7]. Optical WGMs allow light to propagate around a microsphere in a very narrow line because of successive total reflections around the equator of the sphere. This has been demonstrated in many glass systems including, Er:Yb doped phosphate glasses[7], Nd doped tellurite glass[8], Er doped tellurite glass[9], Er doped silica glass and silica glass[10]. Since each dopant produces a different wavelength of emission, a system with different parameters is produced with each glass and is useful in many different applications. Raman emission, another expression of the WGM, has also been observed using a silica microsphere lasing system[3]. By coupling size dependent emission from quantum dots into these systems, different applications could be realized by utilizing the same glass and chemical dopant but simply changing the size of the quantum dots.

The quantum dot has only recently been added to this microsphere system[11]. When the quantum dots are inside of a glass microsphere this luminescence from the quantum dots interacts with the WGMs and effectively lowers the threshold of the input laser. CdSexSl-x quantum dots were embedded into silica microspheres and resonance WGMs were observed. The quantum dots were embedded into the microspheres through annealing at a temperature just above the glass transition temperature, from 580-600° C[11]. Other systems which incorporate nanocrystals into glass microspheres include CdSe/CdZnS nanoparticles[2] and InAs/GaAs nanoparticles[4].

In this paper, cadmium telluride and cadmium sulfide nanoparticle growth was induced by a CO_2 laser inside a glass matrix. The CO_2 laser was used to both create the microspheres and to induce particle growth. Optical and imaging characterization was performed to confirm the presence of nanoparticles.

A.2 Experimental Methods

Previously synthesized B-9 and B-4 glasses[12] doped with CdTe and CdS, respectively, were used in the experiments performed. The components of the CdS doped B-4 glass were as follows in wt %; SiO_2 (56%), B_2O_3 (8%), K_2O (24%), CaO (3%), BaO (9%), and CdS (.5%-1%). The components of the CdTe doped B-9 glass are as follows in wt %: SiO_2 (54.5 %), B_2O_3 (22.6%), K_2O (6.6%), CaO (0.825%), BaO (2.475%), Na_2O (2.26%), Al_2O_3 (1.056 %), ZnO (9.8%), and CdTe (3-5%). These glasses were then formed into fibers using an oxygen flame.

Microspheres are fabricated using a Synrad CO_2 laser to soften and taper a glass fiber at a power of about 3 W. The taper is then placed back into the laser beam to form the microsphere via surface tension at a laser power of 4 W. The diameters of the microspheres range from a few microns to hundreds of microns depending on the application and wavelength of light desired. The power is then decreased to 3 W/mm^2 to induce particle growth inside the microsphere.

The photoluminescence was measured using an argon laser and a nitrogen cooled CCD detector. Transmission electron microscopy images were taken of the particles inside the glass using a Philips CM-12 with a LaB_6 electron source.

A.3 Results

To determine the viability of these experiments and if nanoparticles could be grown using the CO_2 laser, large pieces, bulk, of doped glasses were irradiated using the laser. A CdS doped B-4 bulk glass was irradiated resulting in extensive cracking due to residual stresses in the glass. However, a distinct color change was noted in the glass in the area where the laser beam made contact with the glass, indicating particle growth

Fig. A.1: Shown above is bulk CdS doped glass heat treated using the CO_2 laser. A yellow circle with a diameter just larger than the diameter of the laser can be seen where the nanoparticles formed.

(figure 1). A yellow coloration can be seen in the upper right corner of the glass, indicated by an arrow.

With the success of laser induced nanoparticle growth in the bulk glass, the next experiments grow the nanoparticles directly in the microspheres. In these experiments, the entire microsphere can be engulfed in the laser beam resulting in even heating without residual stresses that cause cracking the bulk glasses. Additionally, microspheres introduce many possible applications as discussed in the introduction.

Glass fibers formed from CdTe doped B-9 glass were used to create microspheres. Microspheres with cadmium telluride particles were synthesized using a CO_2 laser. Two representative microspheres can be seen in figures 2 a and b. Figure 2a shows a microsphere heat treated in the laser for only a few seconds and figure 2b shows a microsphere heat treated with the laser for several seconds. While 2a is a microsphere with clear glass, the microsphere in figure 2b shows a distinct red coloration indicating particles formed inside the microsphere. This coloration occurred after only a few seconds of heat treatment using the CO_2 laser, whereas the furnace heat treatments generally take hours. The photoluminescence from the microsphere in figure 2a gave a spectrum shown in figure 4 which is spectrally similar to that of undoped glass, figure 5. The microsphere which showed red coloration in figure 2b produced the spectrum shown in figure 3. This spectrum shows a sharp photoluminescence peak around 660 nm. This is in correlation to previous work done where quantum confinement emission was detected at the same wavelength[13].

Subsequent TEM characterization was used to determine the size and morphology of the produced nanoparticles. The TEM micrograph shown in figure 6 was obtained from the microsphere seen in figure 2b, the nanoparticles range from 5-10 nm in radius and there were several nm between particles indicating generally well dispersed particles. The clear doped microspheres gave a similar spectrum to the
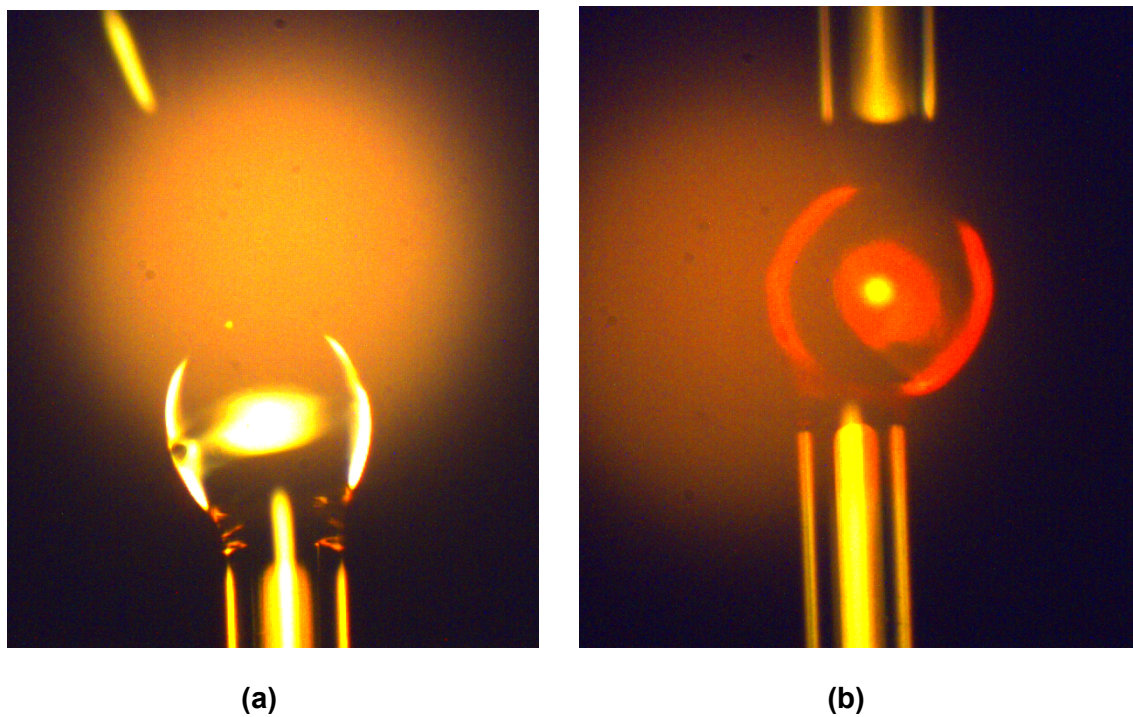
(a)   **(b)**

Fig. A.2: The microsphere on the left was heated for as short a time as possible appears to be clear. This indicates either very small particles or no particles formed inside the microspheres. The microsphere on the right was heated for a few seconds is red in color indicating particle formation in the size range desired.
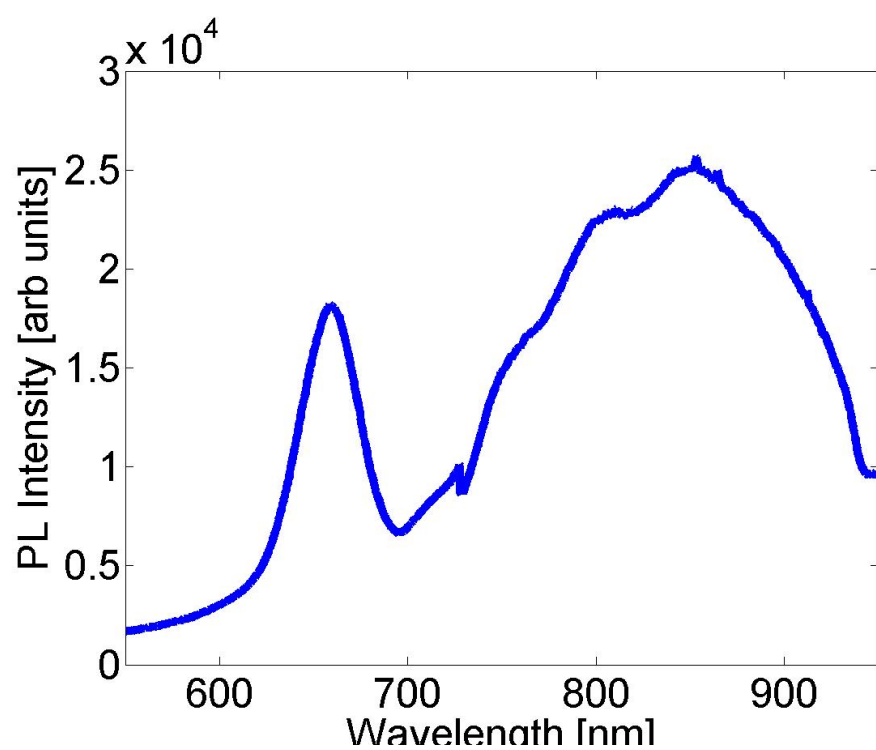
Fig. A.3: This spectrum was obtained from a microsphere heated for 20 seconds at 10 W/mm2.
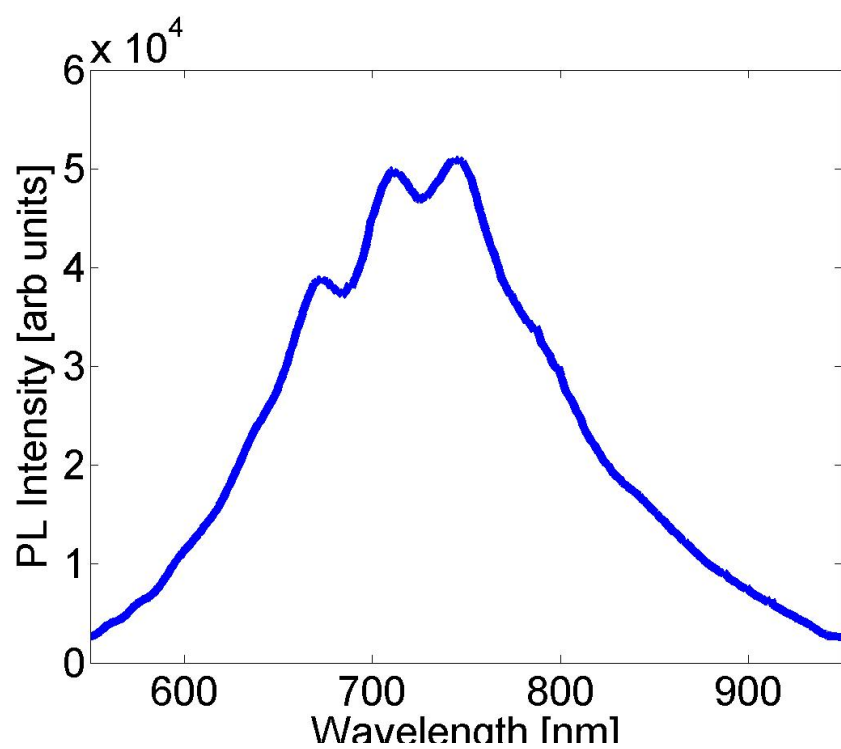
Fig. A.4: The spectrum above was obtained from a microsphere heated for 10 seconds at 5 W/mm2 and appeared clear.
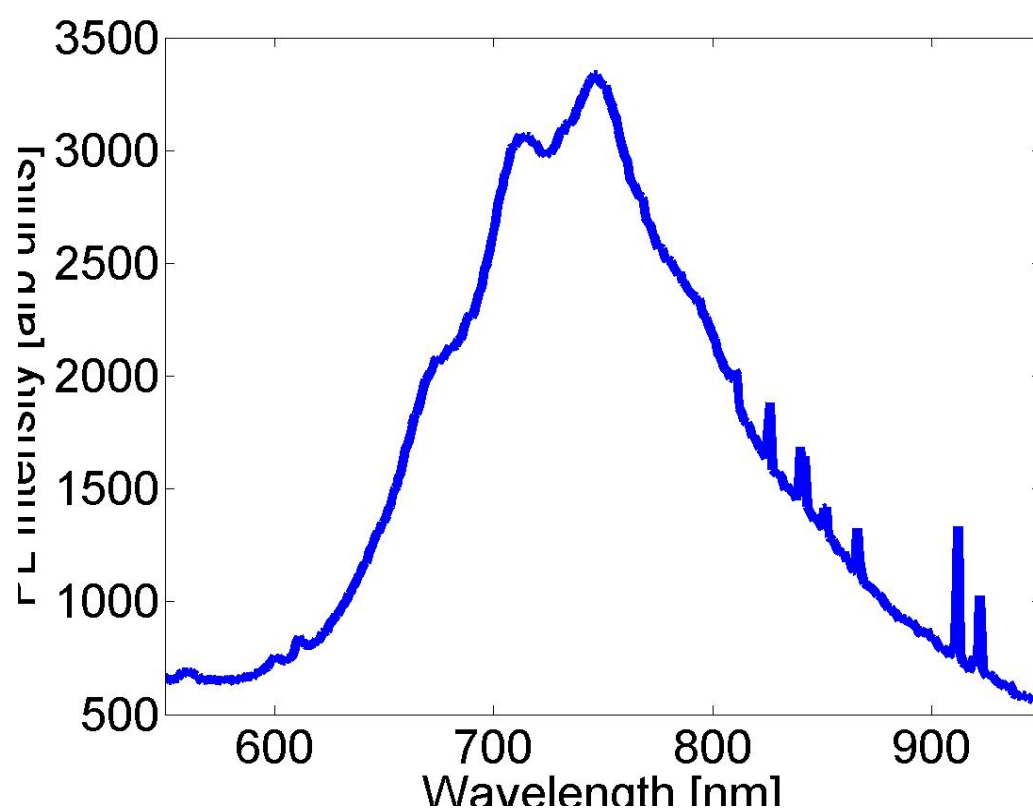
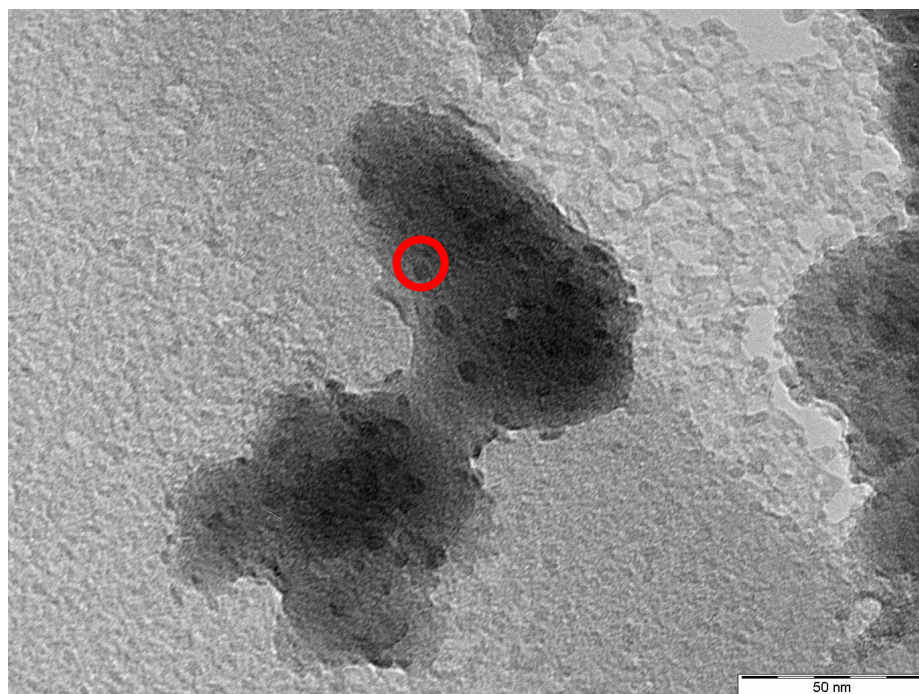**Fig. A.5:** This PL spectrum was obtained from undoped base glass.

Fig. A.6: The micrograph shown above is from a crushed microsphere which was red in color and the photoluminescence spectrum gave a narrow peak at nm. The particles ranged from approximately 5 to 10 nm. The microsphere was heated for 20 seconds at 10 W/mm2.

undoped glass indicating that there were no particles formed in these microspheres. Also, TEM images could not find any evidence of nanoparticle formation in the clear microsphere.

A.4 Summary and Future Work

The CO_2 laser heat treatment causes particle formation at much faster speeds than traditional furnace heat treatments. While research is needed to optimize the particle growth and determine the area of particle formation, this process has given promising initial results. Other research that is in progress is the investigation of different semiconducting materials inside glass microspheres. Also, in situ photoluminescence as the particles form inside the microsphere will be performed. This may give insight to the mechanism of particle formation and quantum confinement luminescence.

References

[1]   D. Navarro-Urrios, Pitanti, A., Daldosso, N., Gorbilleau, F., Rizk, R., Pucker, G., Pavesi, L., "Quantification of the carrier absorption losses in Si-nanocrystal rich rib waveguides at 1.54um," Applied physics letters **92**, 051101 (2008).

[2]   P.T. Snee, Chan, Y., Nocera, D.G., Bawendi, M.G., "Whispering-Gallery-Mode Lasing from a Semiconductor Nanocrystal/Microsphere Resonator Composite," Advanced Materials **17**, 1131-1136 (2005).

[3]   S.M. Spillane, Kippenberg, T.J., Vahala, K.J., "Ultralow-threshold Raman laser using a spherical dielectric microcavity," Nature **415**, 621 (2002).

[4]   S. Steiner, Hare, J., Lefevre-Seguin, V., Gerard, J.-M., "Room temperature lasing of InAs/GaAs quantum dots in the whispering gallery modes of a silica microsphere," Optics Express **15** (16), 10052 (2007).

[5]   H.-C. Ren, Vollmer, F. Arnold, S., Libchaber A., "High-Q microsphere biosensor - analysis for adsorption of rodlike bacteria," Optics Express **15** (25), 17410 (2007).

[6]   L. Collot, Lefevrese-Seguin, V., Brune, M., Raimond, J.M., Haroche, S., "Very High-Q Whispering-Gallery Mode Resonances Observed on Fused-Silica Mocrospheres," Europhysics letters **23** (5), 327-334 (1993).

[7]   M. Cai, Painter, O., Vahala, K., Sercel, P., "Fiber-coupled microscphere laser," Optics Letters **25** (19), 1430 (2000).

[8]   K. Sasagawa, Kusawake, K., Ohta, J., Nunoshita, M., "Nd-doped tellurite glass microsphere laser," Electronics letters **38** (22), 1355-1357 (2002).

[9]   X. Peng, Song, F., Jiang, S., Peyghambarian, N., "Fiber-taper-coupled L-band Er^{3+}-doped tellurite glass microsphere laser," Applied physics letters **82**, 1497 (2003).

[10]   J. Laine, 2003.

[11]   R. Jia, Jiang, D, Tan, P.,Sun, B., "Quantum dots in glass spherical microcavity," Applied physics letters **79** (2), 153 (2001).

[12]   L. Liu, Risbud, S., "Quantum-dot size distribution analysis and precipitation stages in semiconductor doped glasses," Journal of applied physics **68** (1), 130028 (1990).

[13]   C.L. Li, Ando, M., Murase, N., "Preparation and Characterization of glass embedding photoluminescent CdTe nanocrystals," Journal of non-crystalline solids **342**, 32-38 (2004).